

Synchrotron Powder Diffraction Studies of Metal-Organic Frameworks

Christopher Morris

Thesis submitted to the University of Nottingham for the degree of Doctor of Philosophy

September 2016

Declaration

Except where specific reference is made to other sources, the work presented in this thesis is the original work of the author. It has not been submitted, in whole or in part, for any other degree.

Signed: Christopher Morris

Date:

Abstract

This thesis describes a variety of high resolution synchrotron powder diffraction studies of guest-loaded metal-organic frameworks (MOFs). These studies have been used to provide insight into the binding mechanisms of the guest molecules.

Chapter 1 contains an introduction to MOFs, highlighting some potential applications that were investigated in this work. A description of the powder diffraction analysis techniques is also included.

Chapter 2 describes the design and implementation of a remote control gas dosing system for use on the powder diffraction beamline (I11) at Diamond Light Source. To assess the precision of this system, and to gain an insight into the high CO_2/N_2 selectivity of the V(III) MOF, MFM-300(V), an *in situ* powder diffraction experiment was performed, firstly using pure CO_2 and then with an equimolar mixture of CO_2/N_2. Two CO_2 sites were found in all cases, with CO_2-A forming a dipole-dipole interaction with the framework's hydroxyl group, and CO_2-B interacting with CO_2-A *via* further dipole-dipole interaction. In the presence of N_2, particularly at low loadings, the positions of the CO_2 molecules vary quite significantly due to the presence of disordered N_2 within the pore. Further to this investigation, the long term SO_2 adsorption stability of the Al(III) MOF, MFM-300(Al), was studied by powder diffraction. The SO_2-loaded MOF was found to remain stable over a period of 37 weeks.

In Chapter 3, an investigation into the C_8 hydrocarbon vapour adsorption and liquid phase separation properties of MFM-300(M) (M=Al, V, In) is described, with supporting structural information obtained from high resolution powder diffraction. In the vapour phase, MFM-300(Al) was the only MOF of the three studied to show

any discrimination between the 4 isomers, whereas in the liquid phase, it showed no significant separation. Conversely, MFM-300(In) showed the highest degree of separation of *m*-xylene from ethylbenzene and *o*-, and *p*-xylene, however this was accompanied by poor separation of ethylbenzene and *o*-xylene. MFM-300(V) showed a lesser degree of separation of *m*-xylene from ethylbenzene and *o*-, and *p*-xylene, but with a much better separation of ethylbenzene and *o*-xylene. The structural studies revealed π-π stacking interactions between the C_8 hydrocarbons and the phenyl ring of the framework, and in the case of MFM-300(In)(*p*-xylene), tetragonal $I4_122$ → orthorhombic $I2_12_12_1$ phase change was observed. To further investigate the apparent flexible nature of MFM-300(In), high pressure powder diffraction was used, and a similar phase change was observed at 0.584 GPa.

Chapter 4 describes the synthesis and characterisation of a Zr(IV) MOF, MFM-450. The CO_2 and N_2 adsorption properties of this MOF were investigated, and it was found to adsorb 2.32 mmol/g CO_2 at 273 K, followed by 1.97 mmol/g CO_2 at 283 K, and 1.48 mmol/g CO_2 at 298 K. The N_2 adsorption at these temperatures was negligible, resulting in high selectivities. To investigate the nature of CO_2 binding in MFM-450, *in situ* powder diffraction was used. Two CO_2 adsorption sites were found. The site in cage A was found to interact with the phenyl ring of the framework *via* π-π interactions, and the site in cage B interacts with the carboxylate group of the phenyl ring *via* a dipole-dipole interaction.

Acknowledgements

I would like to thank Prof. Martin Schröder, both for providing the opportunity to work on this project, and for his guidance over the last four years. I would also like to thank Dr. Sihai Yang for his support and advice. I am also grateful for the help and support of Prof. Chiu Tang, Dr. Claire Murray, and all of the support staff on beamline I11 at Diamond Light Source, and I thank Prof. Junliang Sun for his assistance in structure solution.

I am very happy to have worked in such a friendly environment for these past four years, and for that I owe particular thanks to Will, Nevo, Simona, Harry and Lydia.

I also thank my project students Lydia, Jamie and Damian, for their hard work and always challenging me with questions.

Finally I would like to thank my parents and family for always being supportive of me throughout my studies.

Table of Contents

Abstract iii

Acknowledgements v

List of Abbreviations xi

Chapter 1 1

Introduction 1

1.1 Porous Materials 2

1.2 Metal-Organic Frameworks 2

1.2.1 Introduction 2

1.2.2 Synthesis of MOFs 3

1.3 Carbon Capture and Sequestration 5

1.4 Molecular Separation 6

1.5 X-Ray Diffraction 7

1.5.1 X-Ray Sources 8

1.5.1.1 X-Ray Tube 8

1.5.1.2 Synchrotron Sources 9

1.5.2 Powder Diffraction 10

1.5.2.1 High Pressure Powder Diffraction 12

1.5.3.2 Rietveld Analysis 13

1.6 References 14

Chapter 2 18

In Situ Studies of Gas-Loaded Metal-Organic Frameworks 18

2.1 Introduction 19

2.1.1 Beamline I11 Manual Gas Dosing System 21

2.2 Aims of this Work 22

2.3 Remote Control Gas Dosing System 23

2.3.1 Initial Design and Specifications 23

2.3.2 Final Design and Specifications 24

2.3.3 GDA Commands 27

2.3.3.1 System Pressurisation 27

2.3.3.2 Sample Dosing 28

2.3.3.3 System Flushing 29

2.4 Results and Discussion 30

2.4.1 MFM-300(V) Structure 30

2.4.2 Single Component Structural Refinements 30

2.4.3 Dual Component Structural Refinements 37

2.4.4 Unit Cell Analysis 40

2.5 MFM-300(Al) – Long Duration SO_2 Stability 41

2.6 Conclusions 47

2.7 Experimental 47

2.7.1 *In Situ* PXRD Collection of MFM-300(V) 47

2.7.2 Long Duration PXRD Collection of MFM-300(Al) 48
2.7.3 PXRD Refinement Details 49
2.8 References 49
Chapter 3 52
Separation of C_8 Aromatic Hydrocarbons in MFM-300 52
3.1 Introduction 53
3.2 Aims of this Work 54
3.3 Results and Discussion 54
3.3.1 MFM-300(M) (M = Al, V, In) and C_8 Hydrocarbon Properties 54
3.3.2 High Resolution PXRD Study 56
3.3.2.1 C_8 Hydrocarbon-loaded MFM-300(Al) 56
3.3.2.1 C_8 Hydrocarbon-loaded MFM-300(V) 60
3.3.2.1 C_8 Hydrocarbon-loaded MFM-300(In) 64
3.3.2.4 Summary of Hydrocarbon-loaded MFM-300(M) Structures 71
3.3.2.5 High Pressure PXRD of MFM-300 72
3.3.3 Vapour Adsorption 76
3.3.3.1 MFM-300(Al) Isotherms 77
3.3.3.2 MFM-300(V) Isotherms 78
3.3.3.3 MFM-300(In) Isotherms 79
3.3.4 Liquid-Phase Separation 80
3.3.4.1 Separations with MFM-300(Al) 81

3.3.4.2 Separations with MFM-300(In) 88

3.3.4.4 Separations with MFM-300(V) 93

3.3.4.5 Binary Breakthrough Experiments 98

3.4 Conclusions 99

3.5 Experimental 99

3.5.1 High Resolution PXRD of Hydrocarbon-loaded MFM-300(M) 99

3.5.2 High Pressure PXRD Collection of MFM-300(In) 100

3.5.3 Vapour Adsorption Experiments 100

3.5.4 Liquid Phase Experiments 101

3.5.4.1 Column Packing 101

3.5.4.2 HPLC Separations 101

3.5.4.3 Breakthrough Experiments 101

3.6 References 102

Chapter 4 104

A Stable Zirconium MOF for CO_2 Separation 104

4.1 Introduction 105

4.2 Aims of this Work 108

4.3 Results and Discussion 108

4.3.1 Synthesis 108

4.3.2 Structure of MFM-450 110

4.3.3 Gas Adsorption Studies 115

4.3.4 Gas Selectivity Studies 118

4.3.5 *In Situ* PXRD Studies 119

4.4 Conclusions 122

4.5 Experimental 122

4.5.1 Synthesis of $Zr_6O_4(OH)_4(BPTC)_3$ (MFM-450) 122

4.5.2 High Resolution PXRD 123

4.5.3 Structural Refinement Details 123

4.6 References 124

Conclusions 125

Appendices 128

Appendix 1.1 - Fits of Rietveld refinements from single component CO_2 adsorption experiment with MFM-300(V) 128

Appendix 1.2 – Fits of Rietveld refinements from dual component N_2/CO_2 adsorption experiment 131

Appendix 1.3 – Fit of SO_2 LDE PXRD 132

Appendix 1.4 – C_8 Hydrocarbon loaded MFM-300(M) PXRD 133

Appendix 1.5 – MFM-450 PXRD 139

List of Abbreviations

BPR – back pressure regulator

BPTC – biphenyl-3,3’,5,5’-tetracarboxylate

CCS – carbon capture and sequestration

CIF – crystallographic information file

COSHH – control of substances hazardous to health

DAC – diamond anvil cell

DCM – dichloromethane

DEF – diethylformamide

DLS – Diamond Light Source

DMF – dimethylformamide

DVPC – dual valve pressure controller

EPICS – Experimental Physics and Industrial Control System

F – film

GC – gas chromatography

GCMC – Grand Canonical Monte Carlo

GDA – Generic Data Acquisition

GOF – Goodness-of-fit

GUI – graphical user interface

HPLC – high performance liquid chromatography

IAST – ideal adsorbed solution theory

ID – internal diameter

IGA – intelligent gravimetric analyser

L – length

LDE – long duration experiment

MAC – multi analyser crystal

MFC – mass flow controller

MFM – Manchester Framework Material

MOF – metal-organic framework

OD – outer diameter

PFA – perfluoroalkoxy alkanes

PTM – pressure transmitting medium

PXRD – powder X-ray diffraction

SCCM – standard cubic centimetres per minute

Chapter 1

Introduction

1.1 Porous Materials

Porous materials are a bulk materials which contains pores that are typically occupied by gas or liquid. The International Union of Pure and Applied Chemistry (IUPAC) states that there are 3 different types of pores: micropores (pore width < 2 nm), mesopores (pore width 2 - 50 nm) and macropores (pore width> 50 nm).[1] This thesis contains examples of a class of porous materials known as MOFs.

1.2 Metal-Organic Frameworks

1.2.1 Introduction

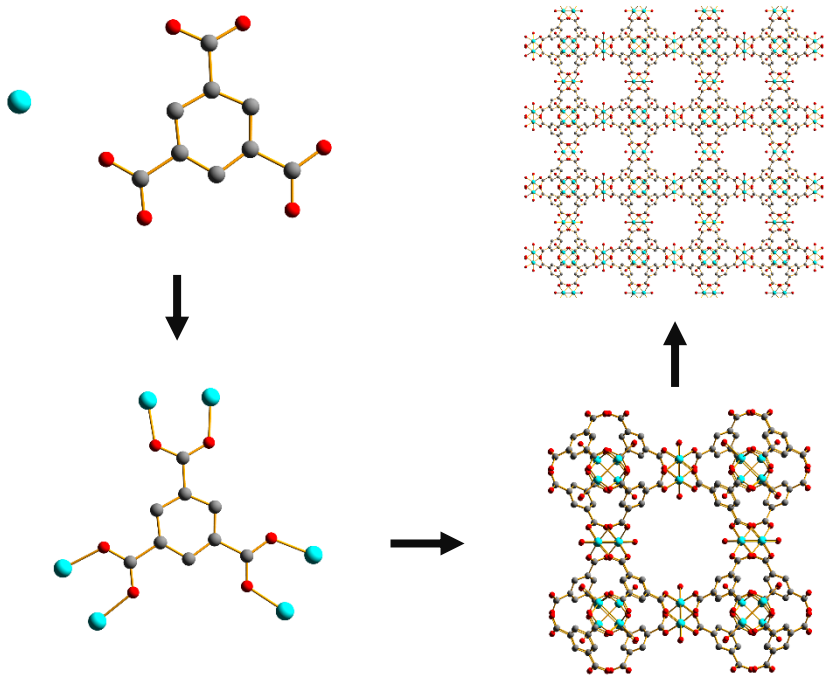


Figure 1.1 - the formation of a MOF (HKUST-1)[3] from inorganic and organic building blocks. Atom colours: copper (blue), oxygen (red), carbon (grey).

MOFs are a class of porous crystalline compounds consisting of metal ions, often in the form of clusters, and organic linkers that often form a three-dimensional structure.[2] The structure of a MOF, and therefore its properties and porosity, can be controlled by careful consideration of the two 'building blocks', which is a particular

advantage over other porous materials such as zeolites and activated carbons. Figure 1.1 demonstrates the way in which the extended framework of a MOF (HKUST-1)[4] can be built up by Cu(II) nodes and trimesic acid.

MOFs have existed for several decades,[3] but it was only in the 1990s that substantial research into their synthesis and properties began.[4-6] Towards the end of the decade, interest in the field was sparked by the development of HKUST-1[4] and MOF-5.[5] There has been an enormous growth in the number of MOF publications since this time (Figure 1.2).

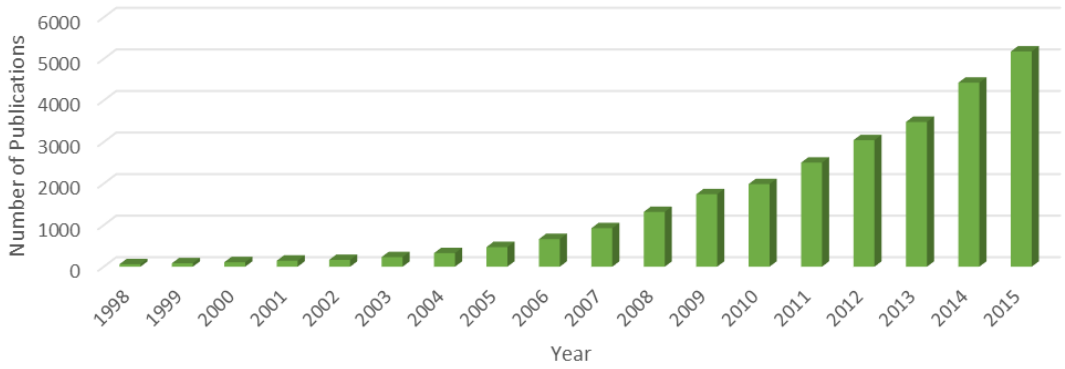


Figure 1.2 - number of publications of "MOFs", "metal-organic frameworks" and "porous coordination polymers" between 1998 and 2015. Data from Web of Science™

The porous nature of MOFs lends itself to numerous potential applications, in fields such as catalysis,[7-10] gas storage,[11-14], molecular separation,[15-18] drug delivery,[19] and chemical sensing.[20]

1.2.2 Synthesis of MOFs

MOFs are most commonly synthesised under solvothermal conditions, at high temperatures (up to 220 °C) in a sealed vessel, such as a PTFE lined stainless steel autoclave or pressure tube. The syntheses typically involve a readily soluble metal salt, such as chlorides and nitrates, polar, high boiling point, solvents such as DMF,

H_2O and DEF, linker, and acid, used to promote crystallinity. MOFs form *via* a reversible self-assembly mechanism, with the organic linkers reversibly binding to the metal nodes, until the most thermodynamically stable product is formed and precipitates out of solution as a microcrystalline powder or single crystals. The acid plays an important role in MOF synthesis as it facilitates the breaking of metal-linker bonds by reprotonating the binding site of the linker. Other synthetic methods, such as microwave heating,[21,22] and ball milling,[23] have also been demonstrated.

Once synthesised, MOFs are generally stored in a low boiling point solvent such as acetone, methanol or ethanol, which is frequently refreshed, resulting in a solvent-exchanged MOF. The reason low boiling point solvents are used for this process is that it enables desolvation of the MOF at much lower temperatures than would be required for the as-synthesised MOF.

1.3 Carbon Capture and Sequestration

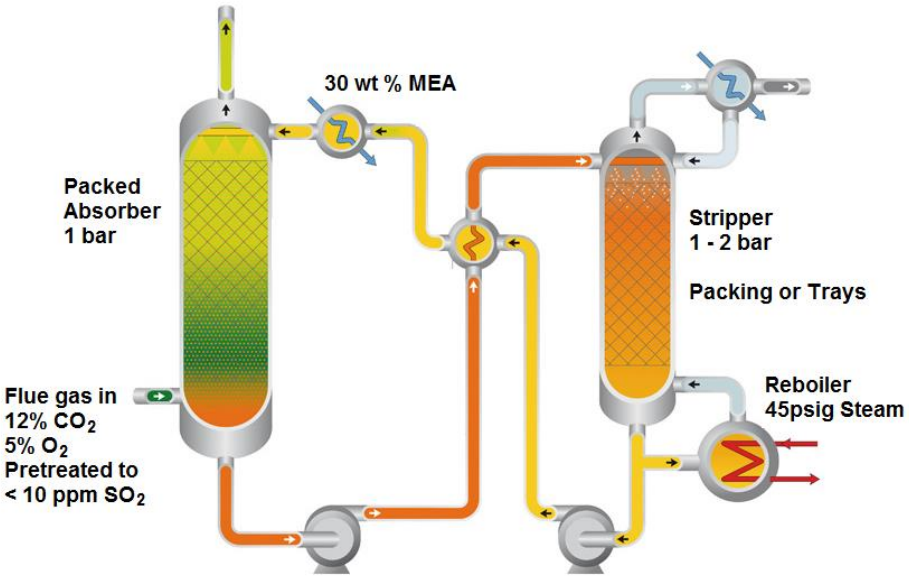


Figure 1.3 – a schematic of the amine scrubbing process currently used in CCS

With increasing levels of anthropogenic CO_2 emissions contributing to climate change, there is growing interest in the field of CCS.[24] The main source of these emissions, contributing around 80% of the total, is from the combustion of fossil fuels,[25] and as such, post-combustion carbon capture is an essential requirement.

The method most widely used in CCS currently is amine scrubbing[26] (Figure 1.3), however this process employs the use of highly toxic and corrosive amines, such as monoethanolamine, which chemisorbs the CO_2 to form carbamates. As a result of this chemisorption, there is a large amount of energy required to regenerate the adsorbent to produce pure CO_2 for sequestration. MOFs are seen as a promising alternative adsorbent, due to their high internal surface areas, functionalisability, and comparatively lower adsorbent regeneration energies.[13]

In addition to a high CO_2 uptake, a suitable MOF must also exhibit excellent selectivity of CO_2/N_2, as N_2 is the main component of flue gas. Due to the

quadrupole of CO_2, methods for enhancing the CO_2 interaction over N_2 include the incorporation of polar functional groups into the MOF. Zhang *et al.*[27] investigated the effects of incorporating linker functionality on the CO_2 uptake of a MOF, and found that the inclusion of polar functional groups within the MOF led to both an increase in CO_2 uptake and an increase in CO_2/N_2 selectivity, compared with the non-functionalised MOF.

Functional groups bound to the metal have also been found to enhance CO_2/N_2 selectivity. Schröder *et al.*[13] also reported the significance of the presence of hydroxyl functionality in the metal-oxygen chain of MFM-300(Al), which results in an high selectivity of CO_2/N_2. Long *et al.*[11] investigated the effect of post synthetically functionalising the Mg^{2+} ions of Mg_2(4,4'-dioxido-3,3'-biphenyl dicarboxylate) with N,N-dimethylethylenediamine, which resulted in a CO_2 uptake 15 times higher than in the unfunctionalised MOF.

1.4 Molecular Separation

An issue of significant importance industrially is the separation of hydrocarbons for the production of fuels and chemical feedstocks. One particular field of interest is the separation of C_8 hydrocarbons. Xylenes and ethylbenzene are generated as mixtures and as such must be separated for use on an industrial scale. Pure isomers have a high commercial value as *p*-xylene (*p*X) is used as a precursor to terephthalic acid, which is used in the production of the polymer poly(ethylene) terephthalate, also known as PET. *O*-xylene (*o*X) is also used in the polymer industry, as a precursor to plasticisers, and meta-xylene (*m*X) is a precursor to isophthalic acid which is used as a co-monomer in certain polymers. However, separation is difficult as the isomers have very similar properties so usual methods of separation, such as energy-intensive

distillation, are only appropriate for the separation of *o*X (b.p 144 °C) from *m*X, *p*X and ethylbenzene (b.p 139 °C, 138 °C and 136 °C respectively).[28]

Ion-exchanged zeolites are currently one of the best adsorptive separation media for this separation,[29] however in recent years there has been considerable interest in studying the potential of MOFs for this purpose.[30,31]

1.5 X-Ray Diffraction

X-ray radiation was first discovered in 1895 by German physicist W. C. Röntgen but it was not until 1912 that the first instance of X-ray diffraction was shown by M. von Laue using a single crystal of hydrated copper sulphate. This sparked much interest in the field and work by W.H. Bragg and W. L. Bragg demonstrated in 1913 that the diffraction pattern could be related to the positions of atoms within the crystals.[32]

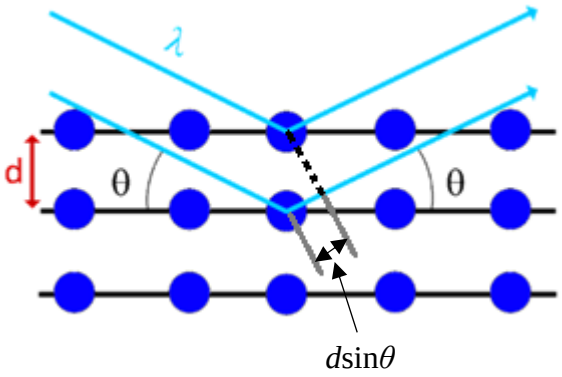


Figure 1.4 – illustration of Bragg's law

W. L. Bragg viewed diffraction as the specular reflections of X-rays by crystallographic planes (Figure 1.4), defined by the Miller indices, *hkl*. Parallel planes (planes with the same Miller indices) are equally spaced a distance of d. When the path difference of two beams ($2d\sin\theta$) is equal to an integer number of wavelengths, then the diffracted beams will constructively interfere, resulting in an intense Bragg peak. This equation of $n\lambda = 2d\sin\theta$ is known as Bragg's law.

1.5.1 X-Ray Sources

1.5.1.1 X-Ray Tube

In the laboratory, X-rays are typically generated by X-ray tubes. High energy electrons are accelerated towards a metal target, often Cu or Mo, resulting in the ejection of an electron from the inner shell. An outer shell electron moves to the inner shell to fill the 'hole' left, and in doing so emits an X-ray at an energy characteristic of the metal target.[32] For Cu, a $3p \rightarrow 1s$ relaxation results in a K_β peak at a wavelength of 1.392 Å, and a $2p \rightarrow 1s$ relaxation results in $K_{\alpha 1}$ and $K_{\alpha 2}$ peaks at 1.54056 Å and 1.54439 Å respectively (Figure 1.5).[33] Monochromators are typically placed between the X-ray source and sample to enable the selection of a specific wavelength for the experiment.

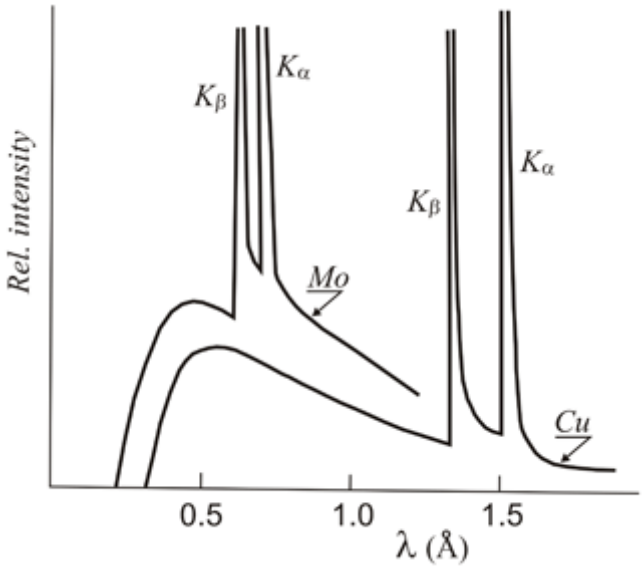


Figure 1.5 – distribution of wavelengths generated by bombardment of a Cu target and a Mo target. K_α and K_β shown. Figure taken from reference 33.

1.5.1.2 Synchrotron Sources

Another method of generating X-rays is using synchrotron sources. A typical layout of a synchrotron is shown in Figure 1.6.[34] Electrons, generated by an electron gun, are accelerated along a linear accelerator into a booster ring which further accelerates the electrons to relativistic speeds. Once at the target energy, the electrons are injected into the storage ring – a polygonal ring containing strong magnetic fields. On the corners of this polygonal ring, the electron beam is bent by a bending magnet (or in the case of third generation Synchrotrons, undulators and wigglers), resulting in the emission of synchrotron radiation tangential to the electron path. This radiation is then filtered and focussed by a series of monochromators, slits and mirrors in the optics hutch of the beamline before passing through to the experimental hutch to probe the sample.

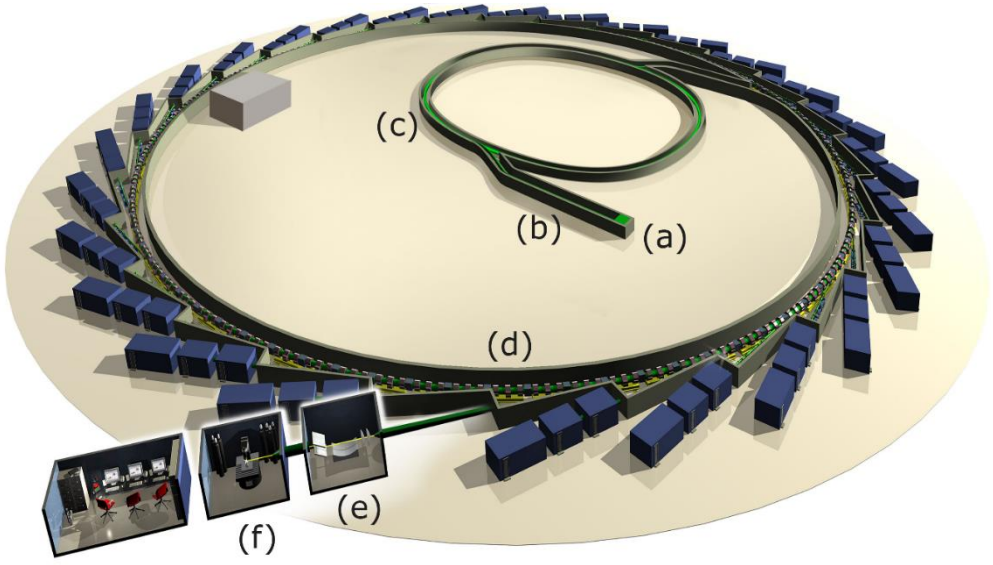


Figure 1.6 – illustration of a typical synchrotron – a) electron gun; b) linear accelerator; c) booster ring; d) storage ring; e) optics hutch; f) experimental hutch. Figure taken from reference 34.

X-rays produced by synchrotrons have a much higher photon flux and brilliance than those produced by lab sources, allowing for much faster data collections times. The wavelength of the X-ray beam can also be tuned to avoid absorption edges of elements.

1.5.2 Powder Diffraction

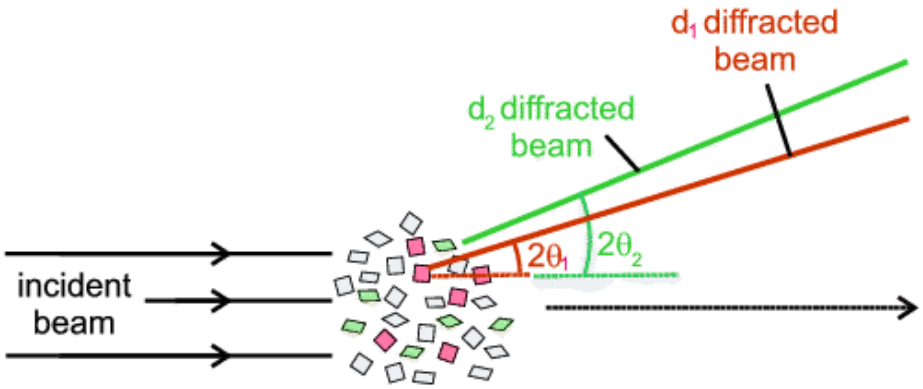


Figure 1.6 – illustration of X-rays interacting with powder. Figure taken from reference 35.

In single crystal diffraction, the crystal must be rotated in order for the Bragg condition to be met for all of the crystallographic planes within the crystal. An ideal powder specimen, however, consists of millions of randomly orientated crystallites, with sufficient crystallites in the correct orientation relative to the X-ray beam for Bragg's Law to be satisfied and a diffraction event to occur (Figure 1.6).[35] By scanning 2θ, a diffractogram of intensity vs. 2θ is obtained (Figure 1.7).[36]

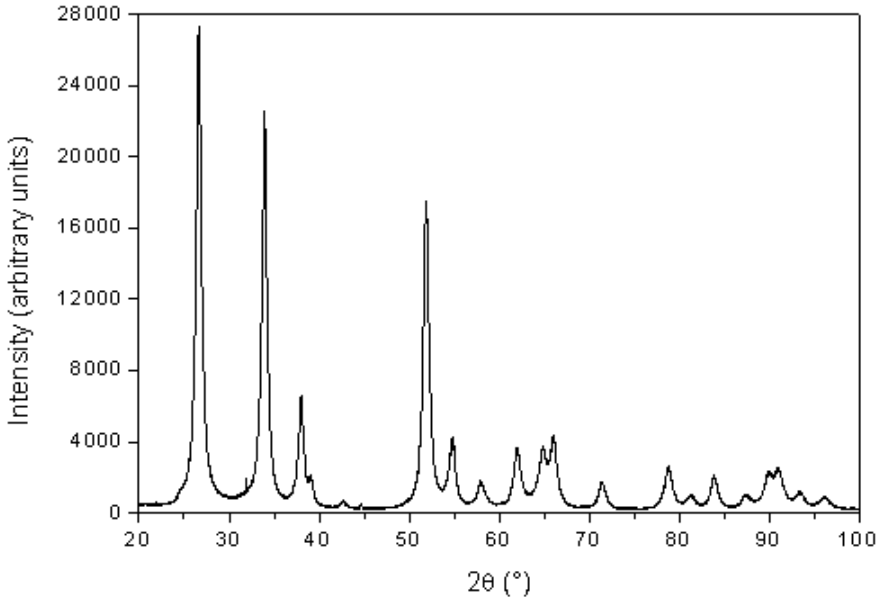


Figure 1.7 – example of a powder diffractogram. Figure taken from reference 36.

In some situations, however, not all orientations of crystallite are occupied. This can occur when the sample aligns along a specific plane, known as preferred orientation, which could result in the potential omission of peaks from the diffractogram, or incorrect relative intensities. The effect of this phenomenon can be minimised by grinding the sample prior to data collection, and mechanically moving the sample during data collection using spinners.[32]

Extraction of structural information from powder diffraction data is much more challenging than from single crystal data, as the three dimensions of the crystallographic data have been condensed into the one dimension of the diffractogram. However, due to the development of whole-profile fittings such as the Pawley and Le Bail methods allowing for peak intensities to be better extracted, and ever-increasing computing power, a growing number of structures are being determined with *ab initio* methods from powder diffraction data.[32]

1.5.2.1 High Pressure Powder Diffraction

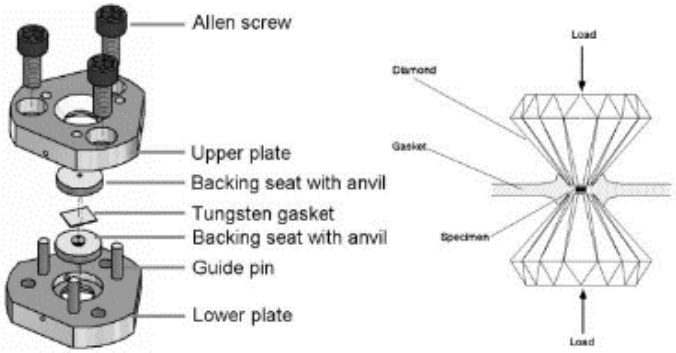


Figure 1.8 – schematic of a DAC with components labelled. Figure taken from reference 37.

In order to probe powder specimens in response to high mechanical pressure, DACs are used (Figure 1.8).[37] Generally, the pressure is generated by tightening the screws holding the cell together, however membrane driven cells also exist. By forcing the two diamonds together towards the specimen space, pressure is transferred onto the sample. To ensure that this pressure is equally (hydrostatically) distributed on the sample, a pressure transmitting medium is also contained in the cell, as well as an internal pressure sensor. The pressure sensor used is often ruby, as the pressure dependence of ruby luminescence is widely known, and can be easily measured *in situ.* It is important that the PTM used does not react with the sample, and in the case of high pressure PXRD of MOFs, PTMs which are too large to enter the pores, such as Fluorinert™ FC-70, are frequently used.

Due to the small sample area, the number of crystallites available for diffraction is less than in an ideal powder. To compensate for this, however, powders are

extensively ground before loading, and the sample cell is oscillated during collection.

1.5.3.2 Rietveld Analysis

The Rietveld method, devised by Hugo Rietveld in 1969,[38] is a least squares minimisation technique for the structural refinement of powder diffraction data. The quantity that is minimised is shown in Equation 1, where *Y*(obs) and *Y*(calc) are the observed and calculated intensities at individual points in the diffraction data, and w_i is the reciprocal of the square of the standard uncertainty of *Y*(obs).

$$\sum_i w_i\{\, Y_i(obs) - \, Y_i(calc)\}^2 \qquad \text{(Equation 1)}$$

As this method is a refinement technique as opposed to solution technique, the structure must be known or at least partially known. Once input into the refinement software, a diffraction profile is calculated, with the intensity of each point, y_{ic}, calculated by Equation 2, where *s* is a scale factor, *k* is the Bragg reflection, L_k is the Lorentz polarisation factor, F_k is the structure factor, θ_k is the position of the Bragg peak, $G\Delta\theta_k$ is the profile function, and y_{ib} is the intensity of the background.

$$y_{ic} = s \sum_k m_k L_k \, |F|^2 G \Delta\theta_k + \, y_{ib} \qquad \text{(Equation 2)}$$

To judge the quality of fit of a Rietveld refinement, the *GOF* (Equation 3) can be used. *GOF* is derived from R_{wp} and R_{exp}, shown in Equations 4 and 5 respectively, where $Y_{o,m}$ and $Y_{c,m}$ are the observed and calculated data points respectively at point *m*, w_m is equal to the reciprocal of the square of the error in $Y_{o,m}$, *M* is the number of data points, and *P* is the number of parameters.

$$GOF = chi = \frac{R_{wp}}{R_{\exp}} \qquad \text{(Equation 3)}$$

$$R_{wp} = \sqrt{\frac{\sum w_m \left(Y_{o,m} - Y_{c,m}\right)^2}{\sum w_m Y_{o,m}^{\ 2}}} \qquad \text{(Equation 4)}$$

$$R_{\exp} = \sqrt{\frac{M - P}{\sum w_m Y_{o,m}^2}} \qquad \text{(Equation 5)}$$

A low *GOF* can be indicative of a good quality refinement, however as the error in the observed intensity is a factor in the equations, often very high quality data with low error can decrease R_{exp}, resulting in a high *GOF*. Because of this, an equally important factor in judging the quality of a fit is the actual graphical fit of the data.

1.6 References

1. K. S. W. Sing, D. H. Everett, R. A. W. Haul, L. Moscou, R. A. Pierotti, J. Rouquerol and T. Siemieniewska, in *Handbook of Heterogeneous Catalysis*, Wiley-VCH Verlag GmbH & Co. KGaA, 2008.

2. S. Kitagawa, R. Kitaura and S.-i. Noro, *Angew Chem Int Ed*, 2004, **43**, 2334-2375.

3. B. F. Hoskins and R. Robson, *J. Am. Chem. Soc.*, 1989, **111**, 5962-5964.

4. S. S.-Y. Chui, S. M.-F. Lo, J. P. H. Charmant, A. G. Orpen and I. D. Williams, *Science*, 1999, **283**, 1148-1150.

5. H. Li, M. Eddaoudi, M. O'Keeffe and O. M. Yaghi, *Nature*, 1999, **402**, 276-279.

6. A. K. Cheetham, G. Férey and T. Loiseau, *Angew. Chem. Int. Ed.*, 1999, **38**, 3268-3292.

7. U. Mueller, M. Schubert, F. Teich, H. Puetter, K. Schierle-Arndt and J. Pastré, *J. Mater. Chem.*, 2006, **16**, 626.

8. F. Stallmach, S. Gröger, V. Künzel, J. Kärger, O. M. Yaghi, M. Hesse and U. Müller, *Angew. Chem. Int. Ed.*, 2006, **45**, 2123-2126.

9. S. Hermes, M.-K. Schröter, R. Schmid, L. Khodeir, M. Muhler, A. Tissler, R. W. Fischer and R. A. Fischer, *Angew. Chem. Int. Ed*., 2005, **44**, 6237-6241.

10. S.-H. Cho, B. Ma, S. T. Nguyen, J. T. Hupp and T. E. Albrecht-Schmitt, *Chem. Commun.*, 2006, **0**, 2563-2565.

11. T. M. McDonald, W. R. Lee, J. A. Mason, B. M. Wiers, C. S. Hong, J. R. Long, *J. Am. Chem. Soc.*, 2012, **134**, 7056.

12. W. Lu, Z. Wei, Z-Y. Gu, T-F. Liu, J. Park, J. Tian, M. Zhang, Q. Zhang, T. Gentle III, M. Bosch, H-C. Zhou, *Chem. Soc. Rev.*, 2014, **43**, 5561.

13. S. Yang, J. Sun, A. J. Ramirez-Cuesta, S. K. Callear, W. I. F. David, D. P. Anderson, R. Newby, A. J. Blake, J. E. Parker, C. C. Tang and M. Schröder, *Nat. Chem*., 2012, **4**, 887-894.

14. J. A. Mason, M. Veenstra and J. R. Long, *Chem. Sci*., 2014, **5**, 32-51.

15. S. Yang, A. J. Ramirez-Cuesta, R. Newby, V. Garcia-Sakai, P. Manuel, S. K. Callear, S. I. Campbell, C. C. Tang and M. Schröder, *Nat. Chem.*, 2015, **7**, 121–129.

16. S. J. Geier, J. A. Mason, E. D. Bloch, W. L. Queen, M. R. Hudson, C. M. Brown and J. R. Long, *Chem. Sci.*, 2013, **4**, 2054-2061.

17. K. L. Kauffman, J. T. Culp, A. J. Allen, L. Espinal, W. Wong-Ng, T. D. Brown, A. Goodman, M. P. Bernardo, R. J. Pancoast, D. Chirdon and C. Matranga, *Angew. Chem. Int. Ed. Engl.*, 2011, **50**, 10888-10892.

18. V. Finsy, H. Verelst, L. Alaerts, D. De Vos, P. A. Jacobs, G. V. Baron and J. F. M. Denayer, *J. Am. Chem. Soc.*, 2008, **130**, 7110-7118.

19. J. Della Rocca, D. Liu, and W. Lin, *Acc. Chem. Res.*, 2011, **44**, 957–968.

20. Z. Hu, B. J. Deiberta and J. Li, *Chem. Soc. Rev.*, 2014, **43**, 5815-5840.

21. S. H. Jhung, J. H. Lee and J. S. Chang, *Bull. Kor. Chem. Soc.*, 2005, **26**, 880–881.

22. J. Klinowski, F. A. Almeida Paz, P. Silva and J. Rocha, *Dalton Trans.*, 2011, **40**, 321-330.

23. D. Crawford, J. Casaban, R. Haydon, N. Giri, T. McNally, and S. L. James, *Chem. Sci.*, 2015, **6**, 1645–1649.

24. J. D. Figueroa, T. Fouta, S. Plasynski, H. McIlvried and R. D. Srivastavab, *Int. J. Greenh. Gas Control*, 2008, **2**, 9–20.

25. T. Barker, R. Pachauri, and A. Reisinger, *Intergov. Panel Clim. Chang.*, 2007.

26. G. T. Rochelle, *Science*, 2009, **325**, 1652-1654.

27. Zhang, W.; Huang, H.; Zhong, C.; Liu, D. *Phys. Chem. Chem. Phys.* 2012, **14**, 2317.

28. J. F. M. Denayer, D. De Vos and P. Leflaive, in *Metal-Organic Frameworks*, Wiley-VCH Verlag GmbH & Co. KGaA, 2011, pp. 171-190.

29. M. O. Daramola, A. J. Burger, M. Pera-Titus, A. Giroir-Fendler, S. Miachon, J. A. Dalmon, L. Lorenzen, *Asia Pac. J. Chem. Eng*., 2010, **5**, 815-837.

30. D. Peralta, G. Chaplais, J.-L. Paillaud, A. Simon-Masseron, K. Barthelet, G. D. Pirngruber, *Micropor. Mesopor. Mat.,* 2013**, 173**, 1-5;

31. D. Peralta, K. Barthelet, J. Pérez-Pellitero, C.Chizallet, G. Chaplais, A. Simon-Masseron, G. D. Pirngruber, *J. Phys. Chem. C,* 2012**, 116**, 21844-21855.

32. V. Pecharsky and P. Y. Zavalij, *Fundamentals Of Powder Diffraction And Structural Characterization Of Materials*, Springer Verlag, 2005.

33. The X-rays, http://www.xtal.iqfr.csic.es/Cristalografia/parte_02-en.html, (accessed August 2016)

34. DLS008, http://www.lightsources.org/imagebank/image/dls008, (accessed September 2016)

35. What is Powder Diffraction?, http://pd.chem.ucl.ac.uk/pdnn/powintro/powdiff.htm, (accessed September 2016)

36. M. D. Cabezas, D. G. Lamas, R. E. Baby, E.Cabanillas and N. E. W. d. Reca, *An. Asoc. Quím. Argent.,* **93**, 69-74.

37. The University of Edinburgh Chemical Crystallography Group, http://www.crystal.chem.ed.ac.uk/research/hpcg.php?page=2, (accessed August 2016)

38. H. Rietveld, *J. Appl. Crystallogr.*, 1969, **2**, 65-71.

Chapter 2

In Situ Studies of Gas-Loaded Metal-Organic Frameworks

2.1 Introduction

Within the field of gas adsorption, the identification of preferred binding sites within the MOF structure provides important insight for understanding the MOF-gas binding interactions and selectivities. Such studies, however, are often very challenging because most porous adsorbents (*e.g.*, activated carbons, porous silica, and large pore zeolites) lack order in their structures. The highly crystalline nature of MOFs, by contrast, makes them particularly advantageous in this perspective since it enables the interrogation of preferred binding sites *via* advanced *in situ* crystallographic investigations.[1-12]

Although single crystal diffraction is the most powerful technique to study the location of guests within a pore, MOF single crystals often decompose during desolvation at elevated temperatures, and as a result, sequential guest loading under pressure is only achieved in exceptional cases.[4-9] On the other hand, techniques such as powder X-ray diffraction (suitable for CO_2, SO_2 *etc*) and neutron powder diffraction (suitable for H_2 and small hydrocarbons) are also being employed to probe these host-guest structures *in situ*.[1,2,10-12]

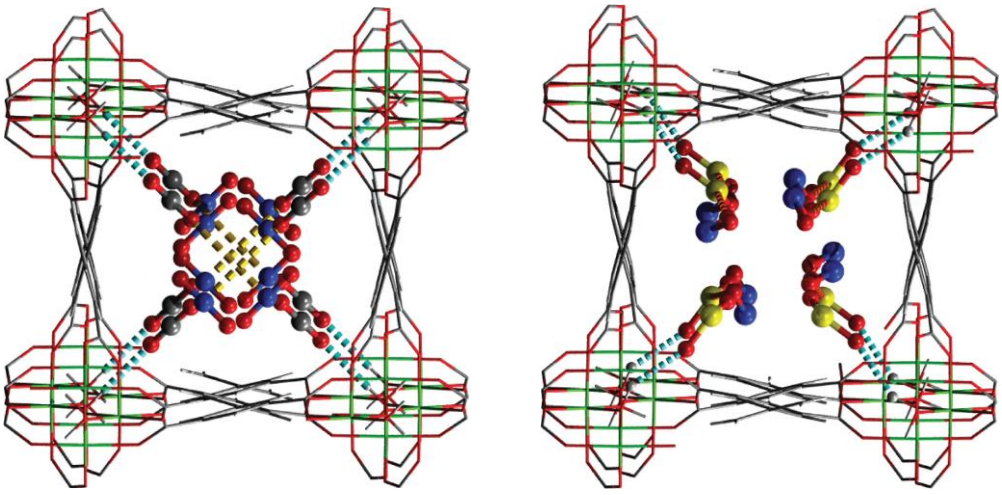


Figure 2.1 – (left) Structure of CO_2-loaded MFM-300(Al); (right) Structure of SO_2-loaded MFM-300(Al). Figure taken from reference 1.

Work previously reported by the Schröder *et al.* has shown the potential of using *in situ* techniques. A publication on MFM-300(Al),[1] an Al(III)-BPTC MOF, used the Rietveld refinements of *in situ* powder diffraction data, combined with inelastic neutron scattering, to visualise CO_2 and SO_2 molecules within the pores (Figure 2.1). This led to a much greater understanding of the way in which these gases interact with the MOF, and provided a rationale for the much lower isosteric adsorption enthalpy observed with this MOF, compared with amine-functionalised MOF materials. This was due to the single dipole-dipole interaction between this MOF and the CO_2, compared with the three interactions present in amine functionalised MOFs.

Current gas dosing systems, however, suffer from two limitations. Firstly, precise control of gas loading is very problematic in operation, and as a result, most of the studies rely on the characterisation of the bare and gas-loaded structures under one or two pressures (typically atmospheric pressure) and thus much information on the gas uptake process over a wide pressure range is lost. Secondly, precise dosing with mixtures of gases with desirable ratio that more closely reflect real world conditions is difficult to achieve and as a result molecular details on the competitive binding between two different gas species in the same pore environment are unclear.

2.1.1 Beamline I11 Manual Gas Dosing System

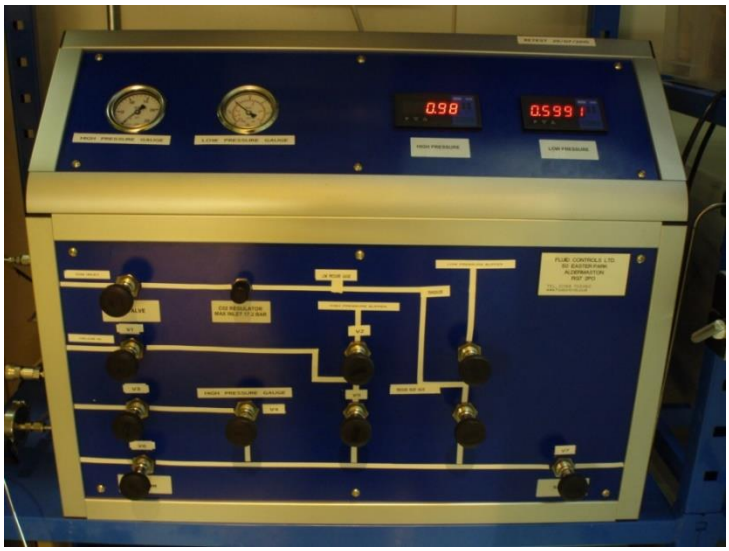


Figure 2.2 – photo of manual gas dosing system on beamline I11 at DLS. Figure taken from reference 12.

The previous gas dosing system on the PXRD beamline I11 at DLS[12] (Figure 2.2) allows users at the beamline to perform *in situ* gas absorption/desorption powder X-ray diffraction studies on samples at either a low pressure ($P \leq 1.5$ bar) or a high pressure ($P \leq 100$ bar), depending on the capillary cell that is used (Figure 2.3). The system is manually operated and is limited to using only one gas at a time.

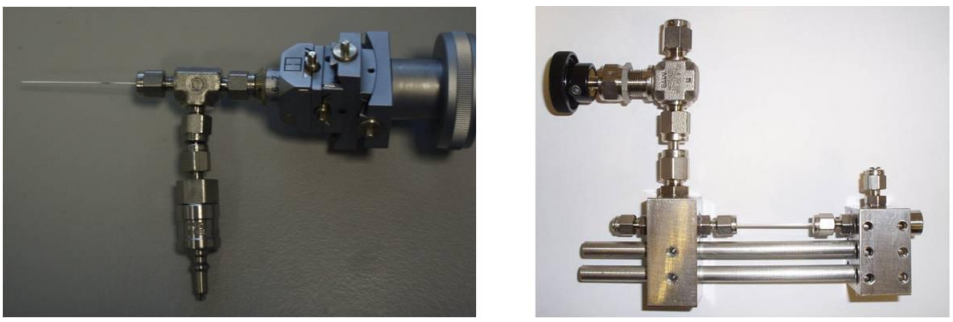


Figure 2.3 – (left) low pressure sample holder with glass capillary; (right) high pressure sample holder with sapphire capillary. Figure taken from reference 12.

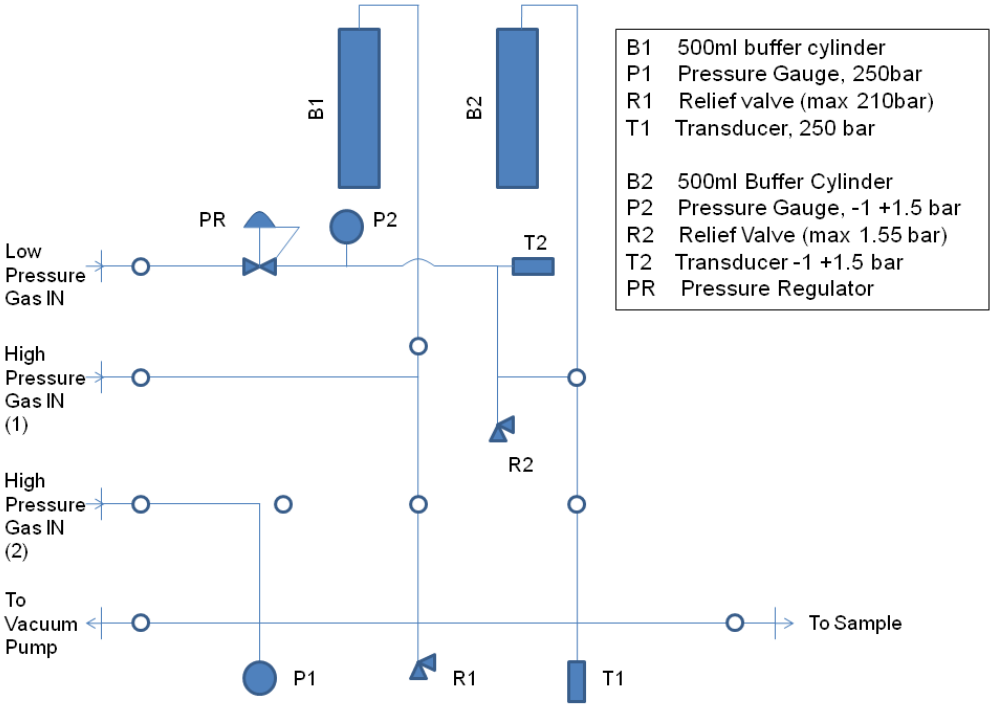


Figure 2.4 – schematic of manual gas dosing system on beamline I11 at DLS. Figure taken from reference 12.

The schematic for the current system is shown in Figure 2.4 and it can be seen that both the low pressure and high pressure sections are implemented on the same panel.

A major drawback of this system, however, is that precise control of pressure is extremely difficult to achieve, and relies heavily on the skill of the operator. The system may also potentially be unsafe, for example if a leak occurred during operation.

2.2 Aims of this Work

The aims of this work were to design and commission a remote control gas dosing system for use on beamline I11 at DLS and to use this system to perform *in situ* studies of gas-loaded MOFs. Of particular interest was the behaviour of hydroxyl-functionalised MOF MFM-300(V), which has been shown to exhibit a high

selectivity for CO_2 over N_2 – a property with significant importance in CCS. Understanding the how this MOF behaves in response to these two gases is central to exploiting its potential on an industrial scale. This in-depth *in situ* study also seeks to determine the precision of the gas dosing system.

Another part of this work was to use *in situ* PXRD to assess the stability of MFM-300(Al) as a long term SO_2 storage medium.

2.3 Remote Control Gas Dosing System

The design and implementation of a remote control gas dosing system was a priority of this work. As an upgrade over the manual system, it was important that the new system offered high precision, chemical compatibility, and a higher degree of operational flexibility.

2.3.1 Initial Design and Specifications

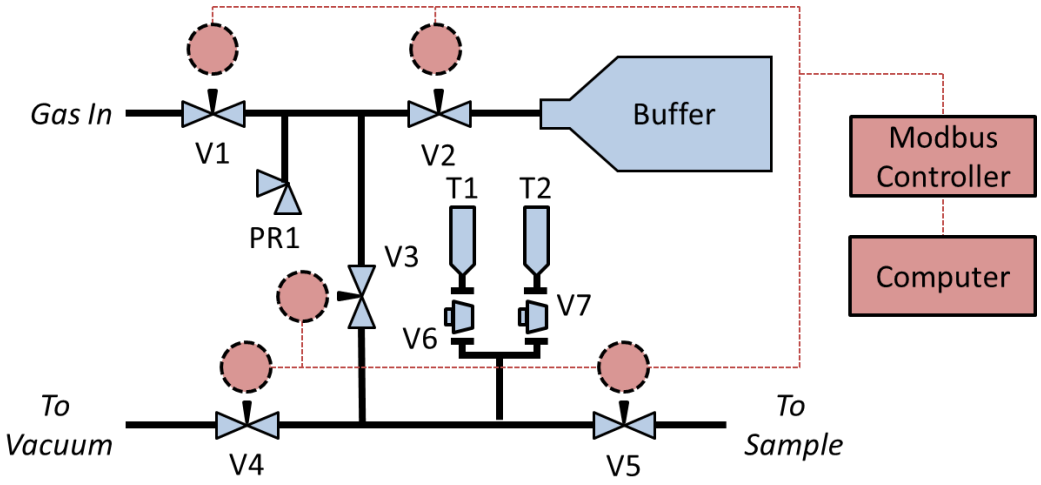


Figure 2.5 – schematic of initial gas dosing system design. V1-V5: needle valves; V6 and V7: plug valves; PR1: pressure release valve; T1: low precision corrosion resistant pressure transducer; T2: high precision pressure transducer. Red components represent the mechanical actuator controls.

The design proposed initially (Figure 2.5) took the approach of mounting computer-controlled mechanical actuators onto needle valves. The wetted parts of the system would be made from PFA, which would ensure exceptional chemical resistivity. Two transducers would be required, one high precision, and one corrosion-resistant, as a high precision corrosion-resistant pressure transistor was not available, meaning that when using corrosive gases, a compromise on precision would be necessary. A major drawback of this design, however, was the potential difficulties in interfacing the Modbus controller with EPICS and GDA. For this reason, an alternative approach was considered.

2.3.2 Final Design and Specifications

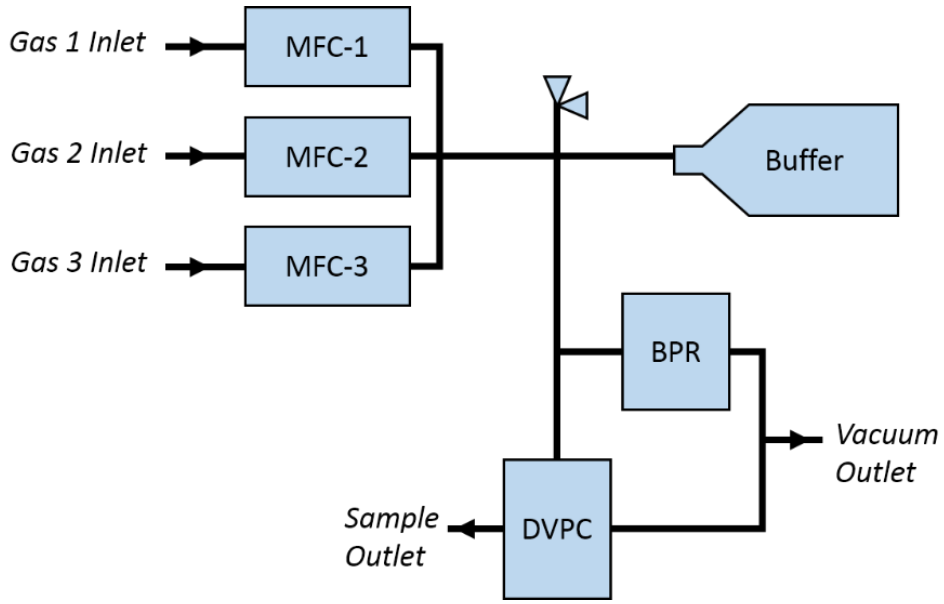


Figure 2.6 – schematic of final design of remote control gas dosing system. MFC-x: mass flow controllers which control the flow of gas into the system; BPR: back-pressure regulator which regulates overall system pressure; DVPC: dual-valve pressure controller which regulates sample pressure.

The final design of the system (Figure 2.6) consists of three Alicat MCS-1SLPM-D MFCs, an Alicat PCS-100PSIA-D pressure controller functioning as a programmable BPR, and an Alicat PCDS-100PSIA-D DVPC connected with 6 mm stainless steel Swagelok tubing and connectors. A pressure relief valve (5.5 bar absolute) is in place to protect the system components from over-pressurisation. Two Swagelok pneumatically activated bellows-sealed valves are used on the vacuum side of the system to control the system's venting to a COSHH extract and to a vacuum pump. Both the BPR and DVPC have a standard accuracy of ± 0.25% of the full scale, which results in pressure accuracy of ± 0.017 bar. The system has been fully integrated into the GDA software environment and EPICS at DLS, and can be controlled either via EPICS GUI or GDA command line.

Sample dosing occurs in two stages. Firstly, the main portion of the system, which acts as a reservoir of gas from which the sample can be dosed, must be pressurised to a pressure which exceeds the highest desired sample pressure. At this point the sample can be dosed. The DVPC ensures that the sample pressure remains constant by opening/closing each of its valves to correct any deviation (Figure 2.7).

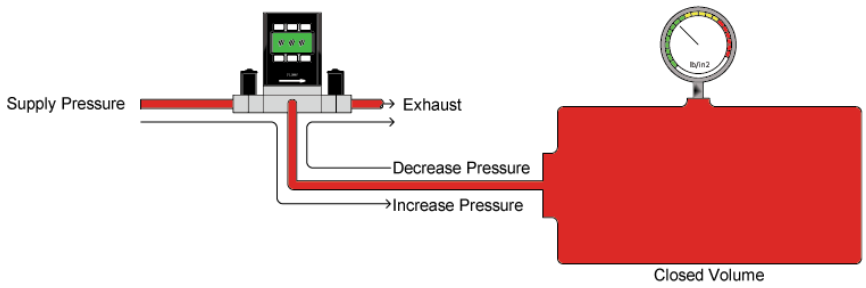


Figure 2.7 – illustration of DVPC method of operation.



Figure 2.8 – photo of fully constructed remote control gas dosing system.

The fully constructed system is shown in Figure 2.8.

2.3.3 GDA Commands

Commands have been written for filling the system, flushing the system, and setting the sample pressure. These commands are outlined below.

2.3.3.1 System Pressurisation

To pressurise the system, gas flows through a chosen MFC into the main body and the buffer. System pressure is controlled by the BPR. The command to control this is shown below, and the logic of this command is shown in Figure 2.9.

Command: gasrig.gasin(mfc=mfc***x***, pressuretarget=***y***)

This command sets system pressure to *z* bar using MFC-*x* with flow rate of 0.1 SCCM.

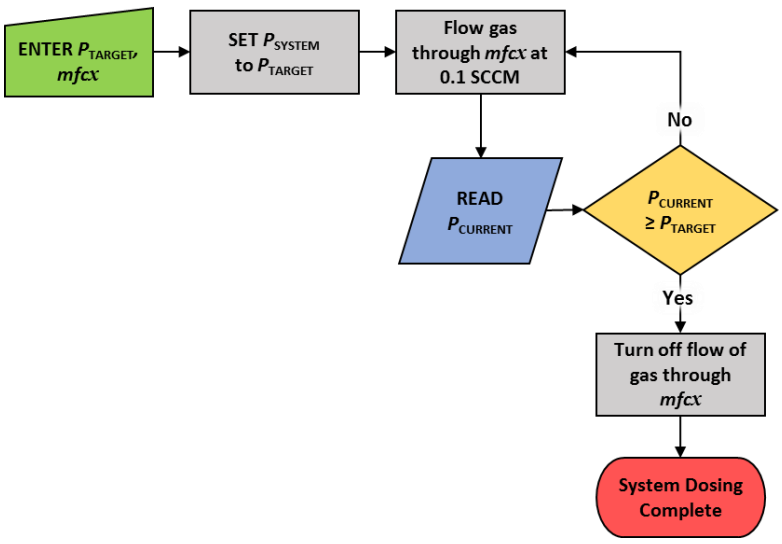


Figure 2.9 – flow diagram of the logic used to dose the system.

2.3.3.2 Sample Dosing

Incremental pressurisation/depressurisation of the sample is necessary to avoid sample movement within the capillary. The command used to dose the sample is shown below and the logic used to achieve incremental changes is shown in Figure 2.10.

Command: sampleP(***x***)

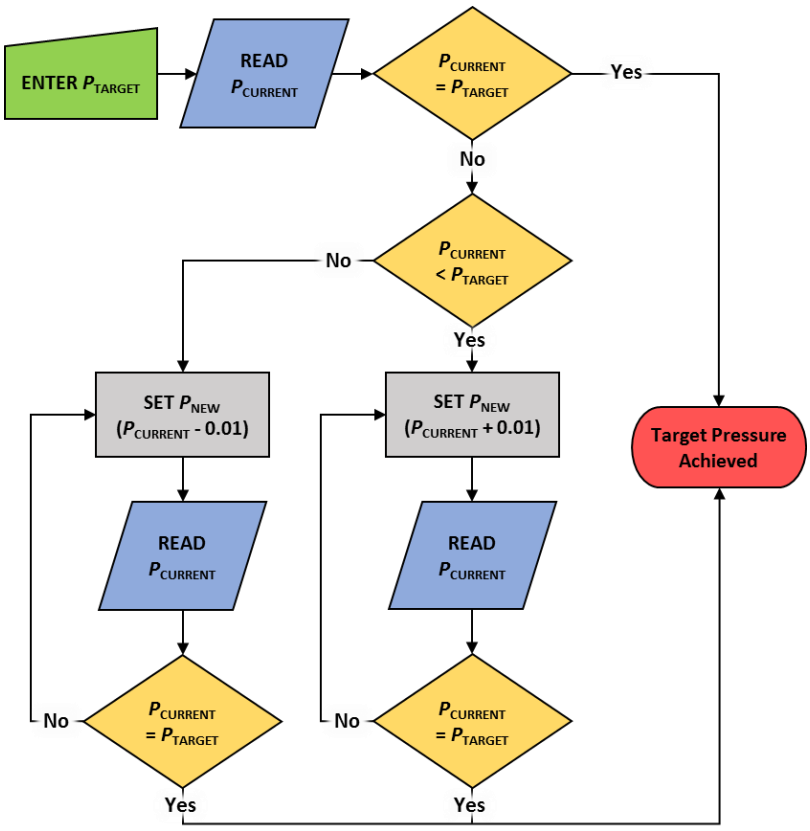


Figure 2.10 – flow diagram of the logic used to dose the sample.

2.3.3.3 System Flushing

To avoid contamination of the vacuum pump with corrosive gases, a flushing method was devised (Figure 2.11). The system must be flushed with an inert gas at least 4 times using the command below.

Command: gasrig.flushSystem(***n***, mfc=mfc***x***, duration=***t***)

This command performs *n* cycles of flowing inert gas from MFC-*x* with flow rate of 0.5 SCCM to a pressure of 4 bar, waiting for *t* seconds and then venting to the COSHH extract.

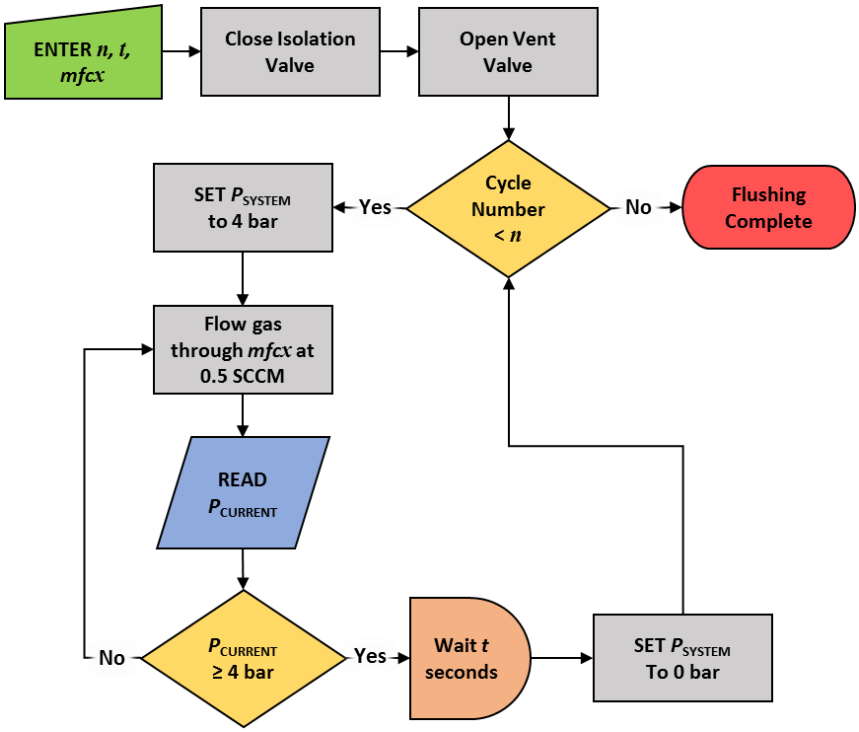


Figure 2.11 – flow diagram of the logic used to flush the system.

2.4 Results and Discussion

2.4.1 MFM-300(V) Structure

The powder diffraction data for the activated MFM-300(V) was indexed to a tetragonal cell of $a = b = 15.13549(4)$ Å, $c = 12.06324(4)$ Å in space group $I4_122$, isostructural to the published MFM-300(Al).[1,2] The structure was obtained by Rietveld refinement of the MFM-300(Al) structure against the data for the activated MFM-300(V), resulting in an excellent fit. The structure consists of biphenyl-3,3',5,5'-tetracarboxylate ligands bridging $[VO_4(OH)_2]$ chains which run along the *c*-axis down the 4_1 screw axis. The unit cell comprises two channels decorated with μ-OH groups.

2.4.2 Single Component Structural Refinements

Difference Fourier analysis of the CO_2-loaded structures revealed two well-defined regions of electron density within the pore of MFM-300(V) – one region situated above the hydroxyl group of the framework and the other located adjacent to this region (Figure 2.12).

Due to the particularly high quality of the data, the standard approach of modelling the guest molecule as a rigid body was not necessary. Instead, soft-restrained CO_2 molecules (penalty functions for both C-O distances and O-O distance) were added to the model obtained from the activated MFM-300(V) refinement, and their positions refined, revealing 2 distinct binding sites (A and B) across the entire pressure range (Figure 2.12). The soft-restrained framework was then refined, resulting in excellent fits and satisfactory structural models across the entire pressure range.

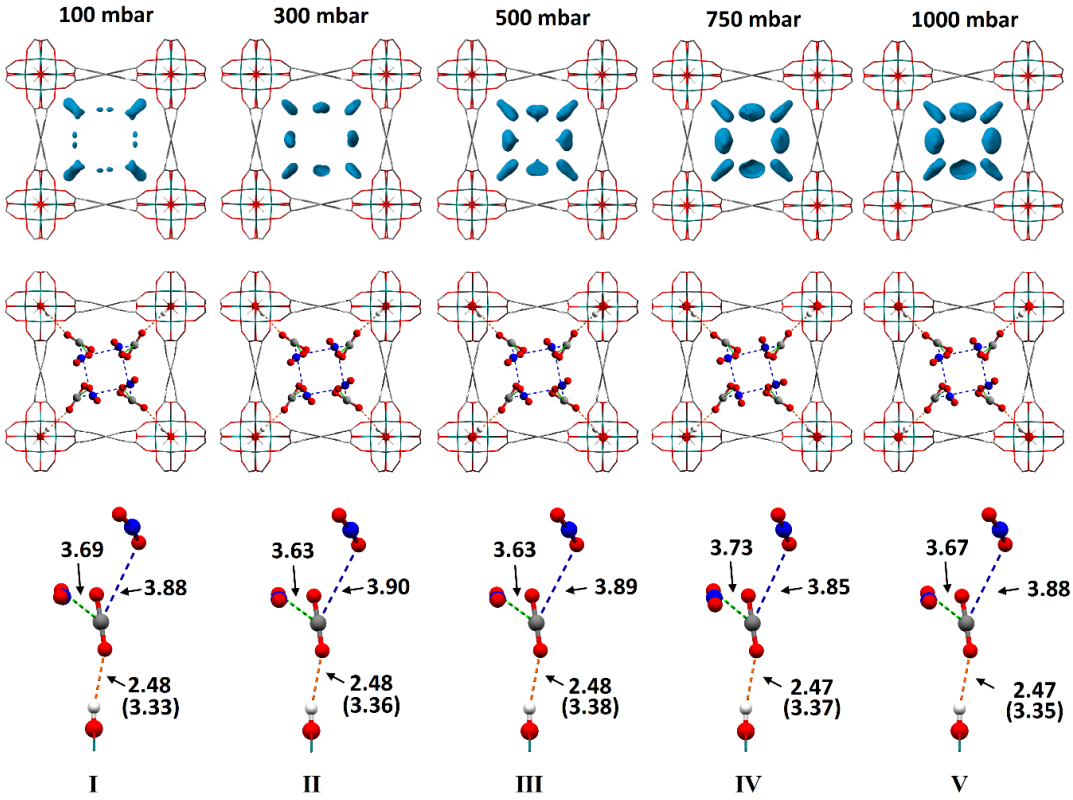


Figure 2.12 - (top) Views of difference Fourier maps of CO_2-loaded MFM-300(V^{III}) viewed along c-axis, from 100-1000 mbar. (middle) Crystal structures of CO_2-loaded MFM-300(V^{III}) viewed along c-axis, from 100-1000 mbar. (bottom) Detailed view of the interaction of CO_2-A with the M-OH and the intermolecular dipole interactions with CO_2-B. In the case of the OH---^{A}O=C=O interaction, O---^{A}O=C=O distances are shown in brackets; Note: for clarity, only half of the positionally disordered CO_2 molecules have been shown.

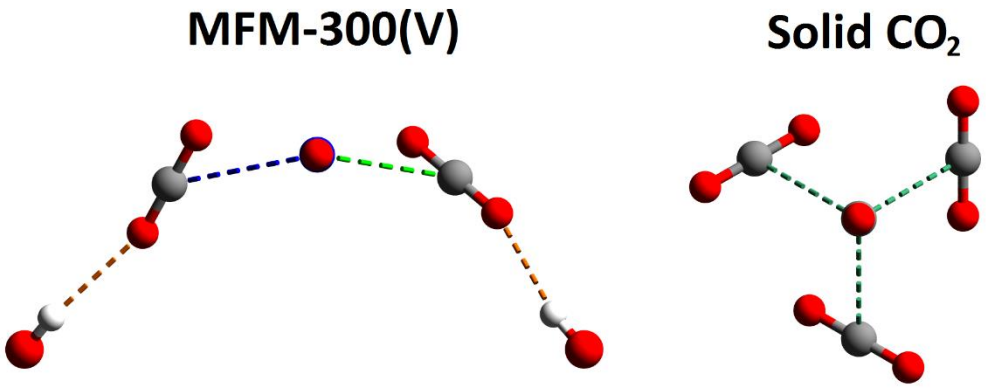


Figure 2.13 – (left) close-up view of interactions between CO_2-B and CO_2-A in MFM-300(V^{III})•$x$$CO_2$; (right) close-up view of the structure of solid CO_2.

The manner in which the two sites interact is shown in Figure 2.13. CO_2-A forms a dipole-dipole interaction with the μ-OH group of the framework and CO_2-B interacts with CO_2-A via two separate dipole-dipole interactions resulting in distorted T-shapes, similar to that found in the structure of solid CO_2. The combination of these interactions forms an infinite chiral network of CO_2-A and CO_2-B that propagates along the pore (Figure 2.14). Similar forms of interaction was found for each dataset of MFM-300(V)•$x$$CO_2$ and excellent graphical fits coupled with goodness-of-fit values ranging from 1.67 to 1.80 are an indication of the accuracy of the structural models.

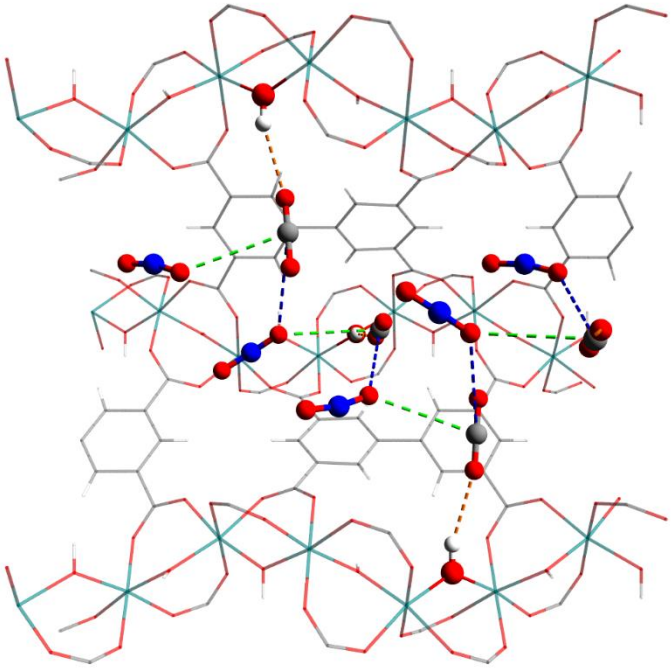


Figure 2.14 - view down *a* axis of MFM-300(V^{III})•*x*CO_2 showing the infinite chiral network that propagates through the pore.

When comparing these interactions with those found in solid CO_2 at 150 K[13] (Figure 2.13) there are many similarities, the most striking of which is the manner in which CO_2-B 'sandwiches' itself between molecules of CO_2-A, maximising the number of dipole-dipole interactions between the molecules. The C=O---C angle of interaction across the entire pressure range (128 - 139°) is also similar to C=O---C angle (132.35°) in solid CO_2. The distances of the interactions in solid CO_2, however, are much shorter than the interactions in MFM-300(V), with a O=C=O---C(=O)$_2$ distance of 3.1066 Å, which is likely due to the solid CO_2 structure being obtained at a much lower temperature than the CO_2-loaded MFM-300(V).

These structures vary significantly from the published MFM-300(Al)•3.2CO_2.[1] Although there are similarities in the OH---O=C=O interaction, in MFM-300(Al) the 2 CO_2 sites align to create discrete T-shaped O=C=O---C(=O)$_2$ units above each

hydroxyl. These differences can be explained by the much narrower pore of MFM-300(Al) having more of a confinement effect than MFM-300(V) on the CO_2 molecules.

Throughout the 5 different loadings of CO_2, the position and orientation of CO_2-A relative to the hydroxyl moiety remains consistent (OH---O=C=O = 2.47 – 2.48 Å). The position of CO_2-B, however, changes slightly over the pressure range. In MFM-300(V)-I, CO_2-B interacts with two molecules of CO_2-A with distances of 3.69(7) and 3.87(6) Å. In MFM-300(V)-II, there is a slight shift of CO_2-B, resulting in interactions at distances of 3.63(5) and 3.89(5) Å. The conformation of CO_2-B in MFM-300(V)-III remains similar to MFM-300(V)-II, with distances of 3.62(5) and 3.89(4) Å. In MFM-300(V)-IV, however, there is a apparent shift in the orientation of CO_2-B resulting in interaction distances of 3.72(4) and 3.85(4) Å. Finally in MFM-300(V)-V, the orientation of CO_2-B changes once more to give interaction distances of 3.66(4) and 3.88(3) Å. These results highlight the dynamic nature of the gases within the pore as the pressure changes, and suggest that the lowest energy crystallographic position for the guest molecules is affected by their crystallographic occupancy. The distances for these interactions are summarised in Table 2.1.

Table 2.1 - Distances of interactions present in MFM-300(VIII)•xCO_2 structures obtained from both single and dual component experiments. Distance 1 = distance from O atom of CO_2-A to O atom of framework's hydroxyl group. Distance 2 and 3 are distances between C atom of CO_2-A and O atom of CO_2-B.

Structure	CO_2 Pressure (mbar)	d1 (Å)	d2 (Å)	d3 (Å)
I	100	3.33(1)	3.69(7)	3.88(6)
II	300	3.36(1)	3.63(6)	3.90(5)
III	500	3.37(1)	3.63(6)	3.90(5)
IV	750	3.370(9)	3.73(4)	3.85(4)
V	1000	3.352(8)	3.67(4)	3.88(4)
VI	300	3.35(2)	3.6(2)	4.0(2)
VII	500	3.34(2)	3.73(4)	3.90(4)
VIII	1000	3.37(1)	3.72(3)	3.93(3)

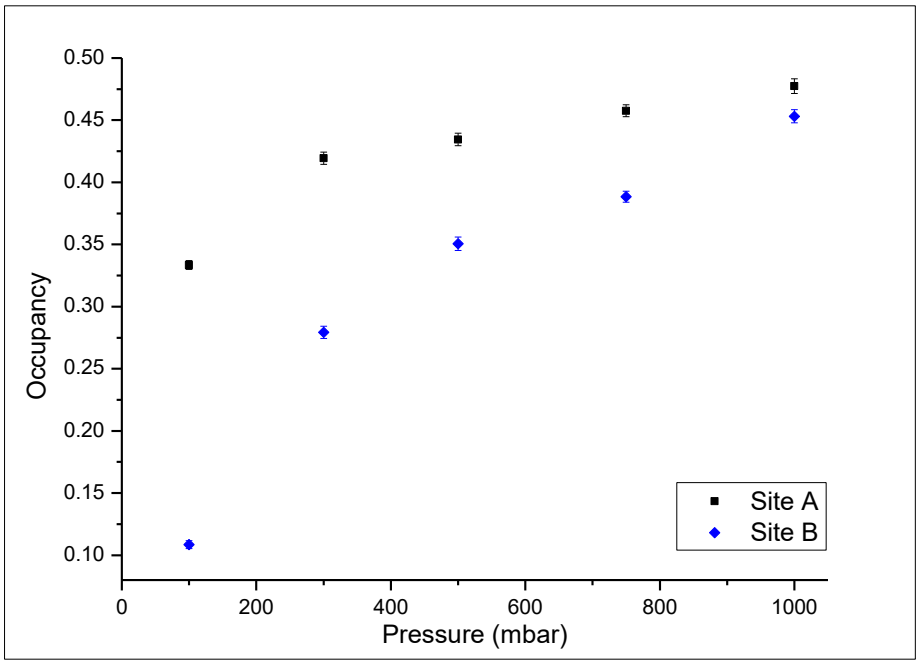


Figure 2.15 - Plot of individual CO_2 occupancies from single component CO_2 adsorption experiment, as a function of pressure.

Inspection of the crystallographic occupancies of each site with respect to pressure (Figure 2.15) shows that each site populates concurrently, with Site A having a higher occupancy than Site B at each pressure. This suggests cooperativity between

each site, and implies a dependency of Site B on the presence of Site A. Combined occupancies of the two sites of CO_2 atoms from these refinements were plotted as a function of pressure and compared to a gravimetric CO_2 isotherm of MFM-300(V) collected at 273 K (Figure 2.16). The plot shows very good agreement with the isotherm, further validating the accuracy of the structural models, whilst also confirming the accuracy of the remote control gas dosing system.

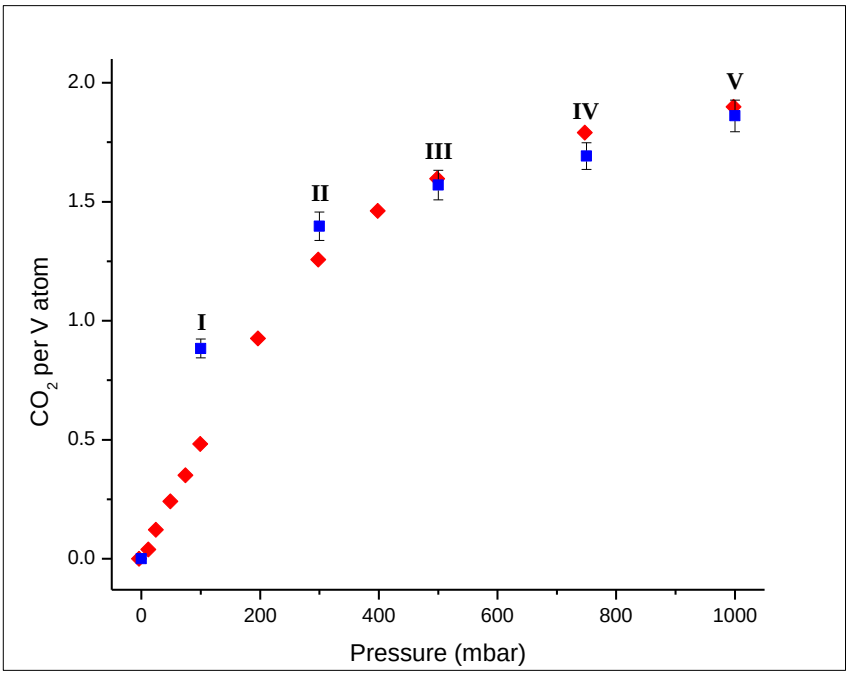


Figure 2.16 - Plot of combined CO_2 occupancies from single component CO_2 adsorption experiment, as a function of pressure (blue square) overlaid on gravimetric CO_2 isotherm of MFM-300(V^{III}) (red diamond).

Difference Fourier analysis of N_2-loaded MFM-300(V) revealed no specific regions of electron density, and refinement of the empty framework against the N_2-loaded data revealed no significant contribution from N_2 to the structure, which is likely due to the MOF's low N_2 uptake at 273 K.

2.4.3 Dual Component Structural Refinements

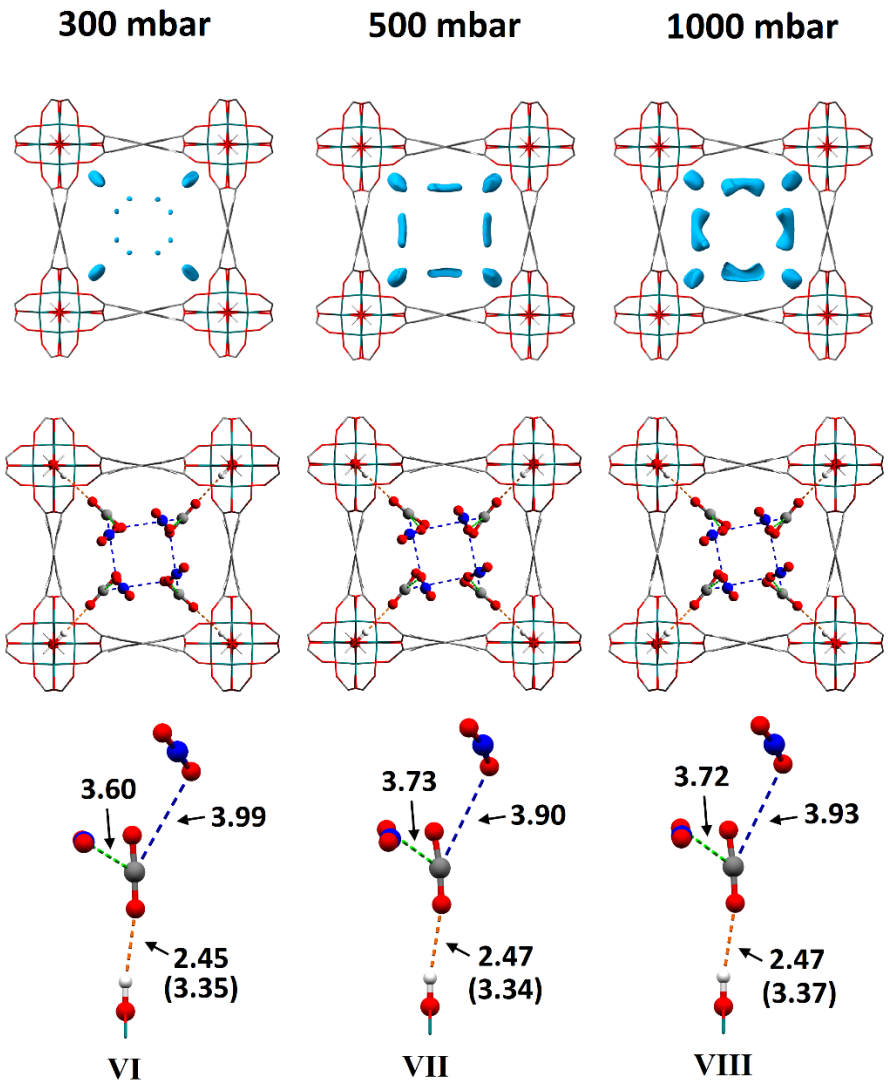


Figure 2.17 - (top) Views of difference Fourier maps of CO_2/N_2-loaded MFM-300(V^{III}) viewed along c-axis, from 300-1000 mbar. (middle) Structures of CO_2/N_2-loaded MFM-300(V) from dual component experiment, viewed along c-axis, from 300-1000 mbar; (bottom) close-up view of the respective interaction of CO_2-A with the framework's hydroxyl and its two interactions with CO_2-B. In the case of the OH---^{A}O=C=O interaction, O---^{A}O=C=O distances are shown in brackets; Note: for clarity, only half of the positionally disordered CO_2 molecules have been shown.

Similarly to the single component CO_2 refinements, difference Fourier analysis revealed two regions of high electron density, which were attributed to CO_2 molecules due to the similarity in position to those in the single component CO_2 refinements. The refinement of two soft-restrained CO_2 molecules in these positions

confirmed the presence of the same two binding sites found in the single component CO_2 structures (Sites A and B) (Figure 2.17). The soft-restrained framework was then refined, resulting in excellent fits for all three loadings. Similarly to the single component N_2 refinements, no adsorption sites could be found for N_2.

Again, the position of CO_2-A remains somewhat consistent across the range of loadings, in a similar range to those in the single component CO_2 structures. In MFM-300(V)-VI, CO_2-B forms two interactions with two molecules of CO_2-A, at distances of 3.6(2) and 3.9(1) Å. The position of CO_2-B in MFM-300(V)-VII, however, has shifted slightly compared to MFM-300(V)-VI, resulting in interaction distances of 3.72(4) and 3.90(4) Å. The position of CO_2-B in MFM-300(V)-VIII is not significantly different to that of MFM-300(V)-VII, with interaction distances of 3.71(3) and 3.92(3) Å. Once again this confirms that crystallographic occupancy can play a role in the preferred position of the guest molecules. These interaction distances are summarised in Table 2.1.

Comparing MFM-300(V)-VI to MFM-300(V)-II, two structures loaded with 300 mbar of CO_2, the distances of interaction of CO_2-B to CO_2-A are quite different. MFM-300(V^{III})-II exhibits O_2C---O=C=O distances of 3.63(6) and 3.90(5) Å whereas the respective distances in MFM-300(V^{III})-VI are 3.6(2) and 4.0(2) Å. MFM-300(V)-VII and MFM-300(V)-III are slightly more similar to each other than MFM-300(V)-VI and MFM-300(V)-II, and MFM-300(V)-VIII and MFM-300(V)-V are even more similar. The reason for these differences is likely due to the presence of N_2 within the pore affecting the position of CO_2-B. As the CO_2 occupancy increases, there is less space for the N_2 molecules to reside in the pores, as it is displaced by CO_2, and therefore less N_2, resulting in the position of CO_2-B becoming more similar to its position in the single component equivalent.

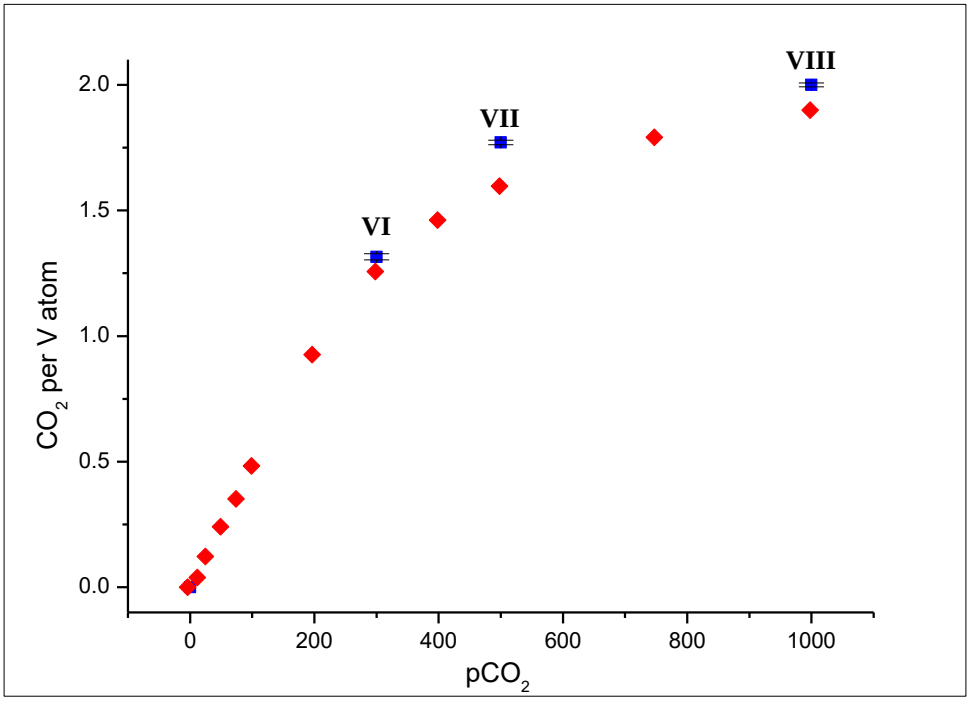


Figure 2.18 - Plot of combined CO_2 occupancies from dual component N_2/CO_2 adsorption experiment as a function of pressure (blue square) overlaid on gravimetric CO_2 isotherm of MFM-300(V^{III}) (red diamond).

The CO_2 occupancy plot from these refinements (Figure 2.18) again show very good agreement with both the gravimetric isotherm and the occupancy plot from the single component experiment, which shows that the extent to which MFM-300(V) adsorbs CO_2 does not change significantly in the presence of N_2 and is direct evidence of CO_2 over N_2 selectivity.

2.4.4 Unit Cell Analysis

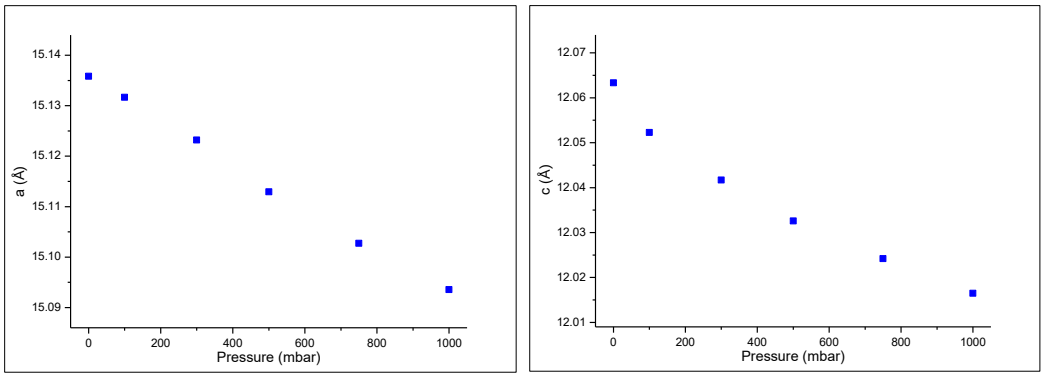


Figure 2.19 - (left) Plot of *a* parameter vs. pressure from single component CO_2 adsorption experiment; (right) Plot of *c* parameter vs. pressure from single component CO_2 adsorption experiment. Note: error bars are smaller than symbol.

Plots of the *a* and *c* parameters derived from Pawley refinements of the single component CO_2 experiments as a function of pressure are shown in Figure 2.19. A general decrease in length is observed for each parameter. When also considering the results from the Rietveld refinements, this trend can be explained by the μ-OH---O=C=O interaction and the two O=C=O---C(=O)$_2$ interactions forming a network of interactions, increase the amount of 'attractive' force within the pore which causes the framework to contract along both axes.

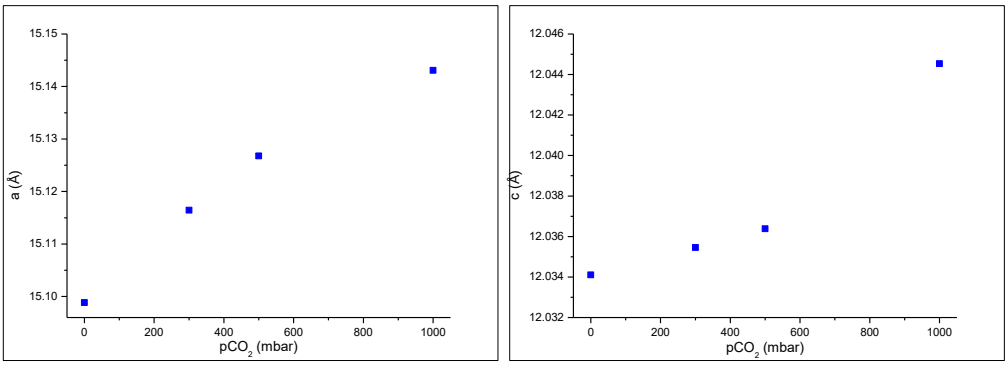


Figure 2.20 - (left) Plot of *a* parameter vs. pressure from dual component N_2/CO_2 adsorption experiment; (right) Plot of *c* parameter vs. pressure from dual component N_2/CO_2 adsorption experiment. Note: error bars are smaller than symbol.

Conversely, in the dual component experiments show a general increase in length of the *a* and *c* parameters with increasing pressure (Figure 2.20), likely due to the presence of disordered non-interacting N_2 inside the pore causing the channel to expand as a result of repulsion. This is supported by the fact that the expansion of the *a* axis, an axis very much dependent on the pore width, is much greater than the expansion of the *c* axis.

2.5 MFM-300(Al) – Long Duration SO_2 Stability

MFM-300(Al) has previously been reported to have exceptional SO_2 uptake at 1 bar.[1] The suitability of this MOF as a long term SO_2 storage medium, however, was unknown. To investigate the long term stability of SO_2-loaded MFM-300(Al), synchrotron PXRD data were collected over a period of 37 weeks. From initial inspection of the data it can be confirmed that the MOF remains crystalline over this period (Figure 2.21).

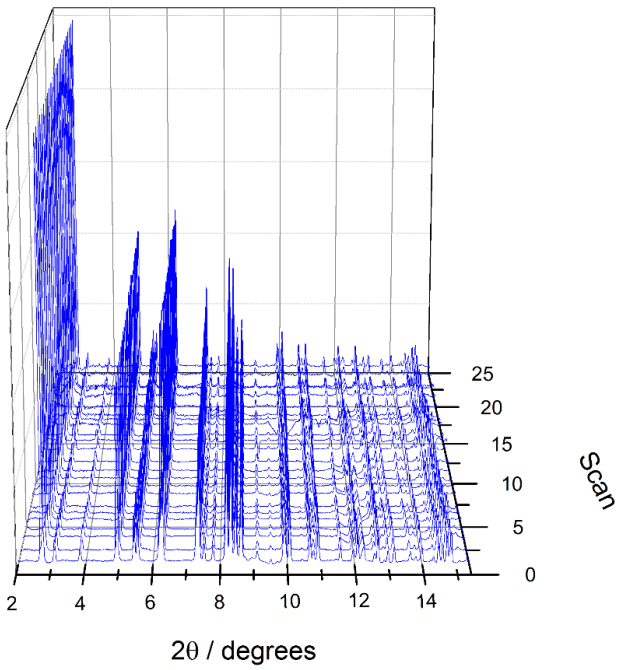


Figure 2.21 – background subtracted plots of the 24 scans of SO_2-loaded MFM-300(Al) collected over 37 weeks.

Rietveld refinements were then performed on the data. Difference Fourier analysis revealed 2 regions of electron density, in similar positions to the SO_2 locations in the published MFM-300(Al)•4SO_2. Two rigid bodies of SO_2 were included in the model and their positions refined. The soft-restrained framework was then refined, resulting in a very good graphical fit. Similarly to the published structure of MFM-300(Al)•4SO_2, one SO_2 molecule forms a hydrogen bonding interaction with the framework's hydroxyl group, and the other SO_2 molecule forms a dipole-dipole interaction with the first. Similar structures were obtained for all 24 structures. The resulting model is shown in Figure 2.22 and the corresponding occupancies and distances tabulated in Table 2.2.

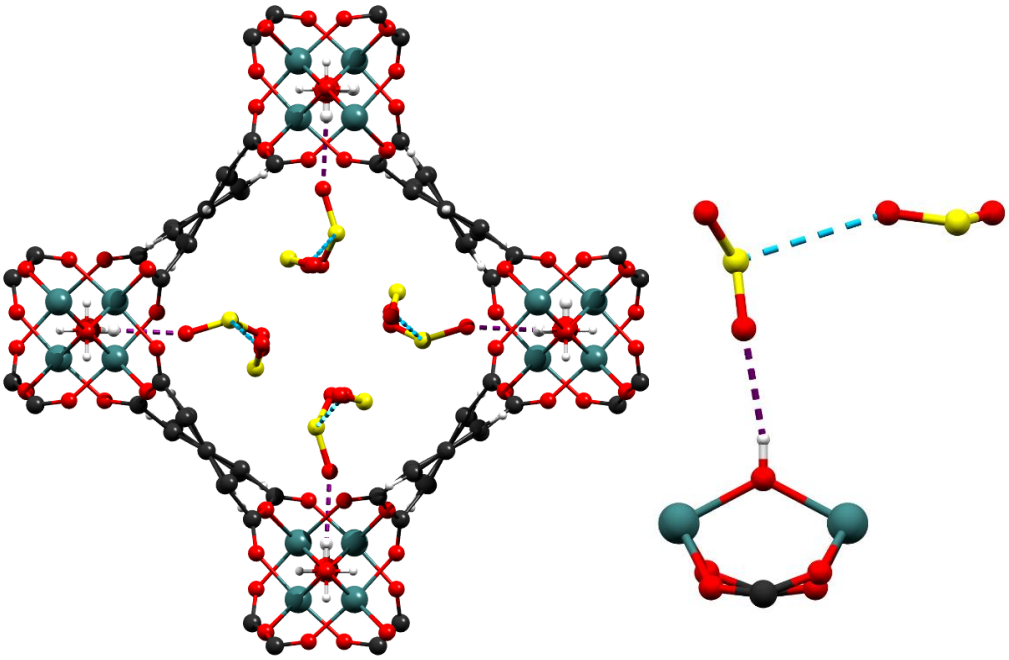


Figure 2.22 – structure SO_2-loaded MFM-300(Al).

Table 2.2 – table of occupancies, O-O distances, and S-O distances from the 24 refined structures of SO_2-loaded MFM-300(Al)

Week	SO_2-I Occ.	SO_2-II Occ.	O-O Distance (Å)	S-O Distance (Å)
1	0.500(3)	0.500(2)	3.08(6)	3.31(9)
2	0.500(5)	0.500(4)	3.13(6)	3.36(9)
3	0.500(5)	0.500(4)	3.09(6)	3.36(9)
4	0.500(5)	0.500(4)	3.09(6)	3.34(8)
10	0.500(4)	0.500(4)	3.11(6)	3.33(8)
11	0.500(5)	0.500(4)	3.12(6)	3.34(8)
12	0.500(5)	0.500(4)	3.11(6)	3.33(9)
13	0.497(5)	0.500(5)	3.11(6)	3.30(10)
14	0.498(5)	0.500(4)	3.11(6)	3.33(9)
15	0.500(5)	0.500(4)	3.11(6)	3.31(8)
16	0.496(5)	0.500(4)	3.11(6)	3.32(9)
20	0.500(7)	0.500(6)	3.06(8)	3.45(10)
21	0.500(11)	0.499(9)	3.07(11)	3.42(17)
22	0.499(7)	0.498(5)	3.08(6)	3.47(9)
23	0.500(6)	0.499(6)	3.04(6)	3.56(10)
24	0.499(7)	0.498(7)	3.06(6)	3.86(13)
25	0.500(10)	0.499(11)	3.07(9)	3.63(18)
26	0.500(8)	0.499(8)	3.08(6)	3.72(14)
32	0.500(11)	0.500(11)	3.04(9)	3.92(21)
33	0.498(11)	0.497(11)	3.05(9)	3.99(21)
34	0.498(13)	0.498(13)	3.08(11)	3.77(22)
35	0.494(11)	0.496(11)	3.07(12)	3.90(19)
36	0.492(8)	0.497(8)	3.07(6)	4.07(15)
37	0.496(11)	0.498(11)	3.04(9)	3.97(20)

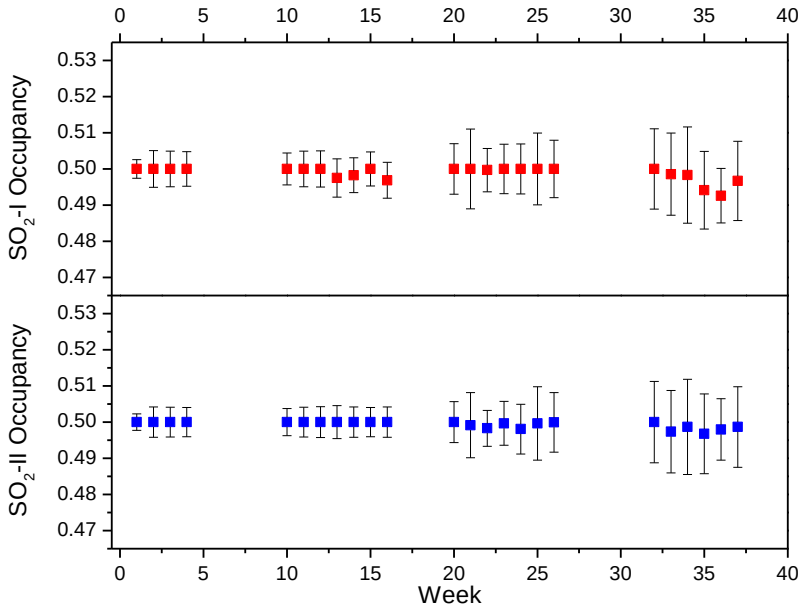


Figure 2.22 – plots of crystallographic occupancy of each SO_2 site.

From the plot of the occupancies of each SO_2 site (Figure 2.22), it can be seen that each site remains at around 0.5 (within error) over the duration of the experiment, meaning that the framework has not lost any adsorbed SO_2 over this time.

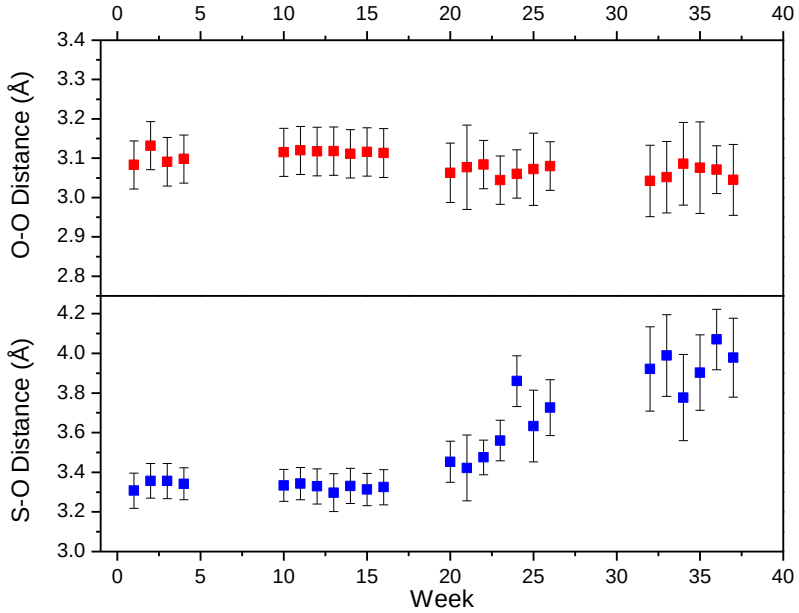


Figure 2.23 – (top) plot of O-O distances; (bottom) plot of S-O distances.

From the plot of O-O distances (which is related to the position of SO_2-I), and S-O distances (which relates to the positions and orientations of SO_2-I and SO_2-II) (Figure 2.23), it appears that the position of SO_2-I remains somewhat consistent over the whole experiment, with a slight drift towards the framework's hydroxyl group beginning at around 20 weeks, whereas the gradual increase of the S-O distance after 20 weeks suggests a more drastic positional or orientational change of SO_2-II.

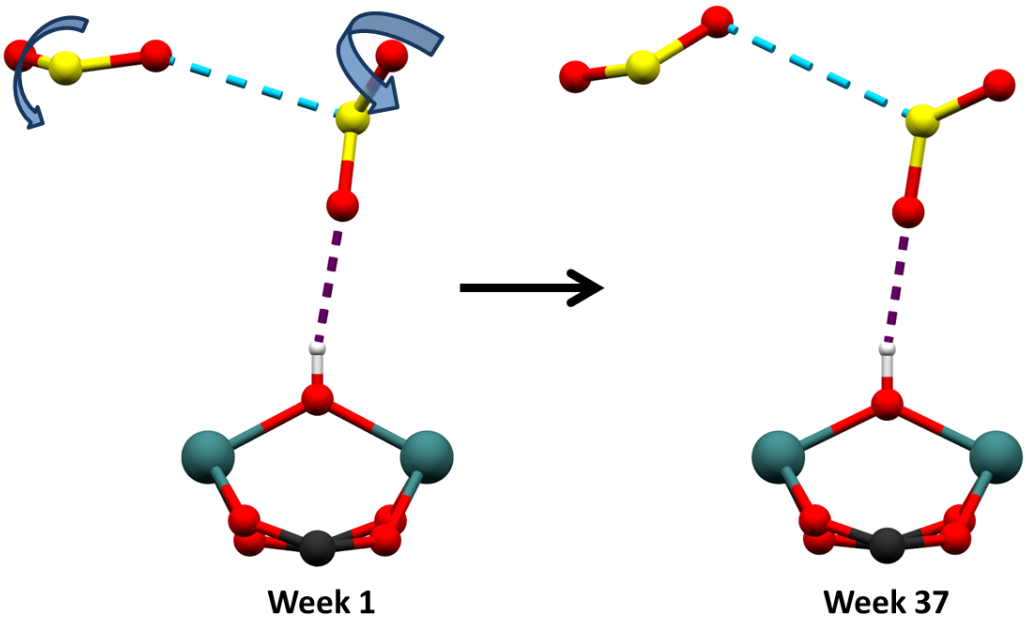


Figure 2.24 – illustration of the shifts in positions of SO_2 molecules from week 1 to week 37.

When comparing the structure obtained from data in week 1 to that of week 37 (Figure 2.24), a slight rotation of SO_2-I is observed, with a minor decrease in OH---O=SO distance, as well as a more apparent shift in the position and orientation of SO_2-II. This guest reordering phenomenon may be the beginning of framework decomposition.

2.6 Conclusions

In summary, a new remote control gas dosing system has been successfully implemented on the powder diffraction Beamline I11 at Diamond, capable of millibar precision and fully automated operation. This system has shown unique *in situ* structural characterisation of MFM-300(V^{III}) as a function of CO_2, N_2, and CO_2/N_2 equimolar mixture loading. Rietveld structural analysis confirmed the presence of two distinct CO_2 sites within the MOF pore with a hydrogen bond interaction between the framework's μ-OH and CO_2-A, and two further intermolecular dipole interactions between CO_2-B and CO_2-A. The position of CO_2-A was found to remain consistent across the entire pressure range; however, the position of CO_2-B was found to be dynamic as a function of pressure. Upon dosing of the CO_2/N_2 equimolar mixture, a similar network of CO_2-A and CO_2-B was observed in MFM-300(V^{III}). At higher loading of the mixture, the presence of N_2 in gas phase was not found to have notable impact on the positions of adsorbed CO_2. However at lower loadings, the position of CO_2-B was found to be slightly different to its single component equivalent. Occupancy plots from both the single and dual component experiments show excellent agreement with the adsorption isotherms, confirming the precision of the gas dosing system.

2.7 Experimental

2.7.1 *In Situ* PXRD Collection of MFM-300(V)

High resolution synchrotron PXRD experiments were performed on beamline I11 at DLS (λ = 0.825633 Å). A sample of acetone-exchanged MFM-300(V) was loaded into a 0.7 mm borosilicate capillary which was secured into the sample cell. The cell was pressurised to 1.5 bar with N_2, the DVPC switched to 'hold' mode and the

pressure monitored. The pressure remained at 1.5 bar indicating that the cell was sealed. The system was then evacuated of N_2 and dosed with CO_2 to 2 bar.

The sample was then activated at 373 K under vacuum (1 x 10^{-6} bar) for 1 hour, cooled to 273K and data was collected for 1 hour with beamline I11's high resolution MAC detectors.[14] The sample was then dosed with 100, 300, 500, 750, and 1000 mbar of CO_2 with 1 hour data collection, at 273 K, 30 minutes after each dosing, allowing for sample equilibration. The sample was subsequently reactivated at 373K under vacuum (1 x 10^{-6} bar) for 30 minutes and the system fully evacuated of CO_2.

The system was dosed with N_2 to 2 bar, and the sample dosed to 300, 500 and 1000 mbar with 15 minute data collections using MAC detectors, at 273 K, 30 minutes after each dosing. The sample was then reactivated at 373K under vacuum (1 x 10^{-6} bar) for 30 minutes and the system fully evacuated of N_2.

To prepare a CO_2/N_2 mixture (1:1, v/v), the system was first dosed with 1.5 bar CO_2, followed by 1.5 bar N_2, resulting in an overall system pressure of 3 bar. The sample was then dosed with the mixture to 600, 1000 and 2000 mbar with 1 hour data collection, at 273 K, 30 minutes after each dosing.

2.7.2 Long Duration PXRD Collection of MFM-300(Al)

Synchrotron PXRD data were collected on beamline I11's LDE facility at DLS, weekly, for a period of 37 weeks using a Pixium area detector (λ = 0.49420 - 0.49481 Å). A sample of acetone-exchanged MFM-300(Al) was loaded into a 0.7 mm borosilicate capillary and secured into the sample cell. It was then activated at 373 K for 1 hour, cooled to room temperature, and dosed to 1 bar with SO_2. The end of the capillary was then submerged in liquid nitrogen, removed from the sample

cell, and its open end was flame sealed using a butane torch. The sealed capillary was then mounted in the LDE holder.

2.7.3 PXRD Refinement Details

Structures and unit cells of MFM-300(V^{III}) for the entire range of loadings were refined, using the Rietveld and Pawley methods respectively, with TOPAS Academic 5. The backgrounds of the profiles were fit using a Chebyshev polynomial with 13 coefficients, and the Stephens anisotropic peak function[15] used to account for the slight anisotropic line broadening observed. Two well defined regions of electron density in the pore were revealed by difference Fourier analysis. In the pure CO_2 experiment, these regions were assigned as CO_2, and in the equimolar CO_2/N_2 mixture experiments, these regions were also assigned as CO_2 rather than N_2, due to both the similarity in position to the pure CO_2 experiments, and also the shape of the electron density being more suited to a linear triatomic molecule as opposed to a small, more spherical, diatomic molecule. In all cases, the CO_2 molecules were soft restrained, rather than modelled as rigid bodies. Soft restraints involve 1-1 and 1-2 distances refined in a weighted penalty function which is minimised during the refinement. The positions of these soft restrained atoms were refined, followed by a final refinement of the soft restrained framework, resulting in excellent fits and satisfactory structural models for the entire pressure range. Individual occupancies and isotropic temperature factors of the atoms in each CO_2 molecule were made equal, and the values for each molecule were refined simultaneously.

2.8 References

1. S. Yang, J. Sun, A. J. Ramirez-Cuesta, S. K. Callear, W. I. F. David, D. P. Anderson, R. Newby, A. J. Blake, J. E. Parker, C. C. Tang and M. Schröder, *Nat. Chem.*, 2012, **4**, 887-894.

2. S. Yang, A. J. Ramirez-Cuesta, R. Newby, V. Garcia-Sakai, P. Manuel, S. K. Callear, S. I. Campbell, C. C. Tang and M. Schröder, *Nat. Chem.*, 2015, **7**, 121–129.

3. S. J. Geier, J. A. Mason, E. D. Bloch, W. L. Queen, M. R. Hudson, C. M. Brown and J. R. Long, *Chem. Sci.*, 2013, **4**, 2054-2061.

4. R. Vaidhyanathan, S. S. Iremonger, G. K. H. Shimizu, P. G. Boyd, S. Alavi and T. K. Woo, *Science*, 2010, **330**, 650-653.

5. J. L. C. Rowsell, E. C. Spencer, J. Eckert, J. A. K. Howard and O. M. Yaghi, *Science*, 2005, **309**, 1350-1354.

6. J. P. Zhang and X. M. Chen, *J. Am. Chem. Soc.*, 2009, **131**, 5516–5521.

7. S. Takamizawa, E. Nataka, T. Akatsuka, R. Miyake, Y. Kakizaki, H. Takeuchi, G. Maruta and Sadamu Takeda, *J. Am. Chem. Soc.*, 2010, **132**, 3783–3792.

8. E. C. Spencer, J. A. K. Howard, G. J. McIntyre, J. L. C. Rowsell and O. M. Yaghi., *Chem. Commun.*, 2006, 278-280.

9. C. P. Krap, R. Newby, A. Dhakshinamoorthy, H. García, I. Cebula, T. L. Easun, M. Savage, J. E. Eyley, S. Gao, A. J. Blake, W. Lewis, P. H. Beton, M. R. W, D. R. Allan, M. D. Frogley, C. C. Tang, G. Cinque, S. Yang and M. Schröder, *Inorg. Chem.*, 2016, **55**, 1076–1088.

10. E. D. Bloch, W. L. Queen, R. Krishna, J. M. Zadrozny, C. M. Brown and J. R. Long, *Science*, 2012, **335**, 1606-1610.

11. Y. Yan, I. Telepeni, S. Yang, X. Lin, W. Kockelmann, A. Dailly, A. J. Blake, W. Lewis, G. S. Walker, D. R. Allan, S. A. Barnett, N. R. Champness and M. Schröder, *J. Am. Chem. Soc.*, 2010, **132**, 4092–4094.

12. J. E. Parker, J. Potter, S. P. Thompson, A. R. Lennie and C. C. Tang, *Mater. Sci. Forum*, 2012, **706-709**, 1707-1712.

12. M. Savage, I. da Silva, M. Johnson, J. H. Carter, R. Newby, M. Suyetin, E. Besley, P. Manuel, S. Rudić, A. N. Fitch, C. Murray, W. I. F. David, S. Yang and M. Schröder, *J. Am. Chem. Soc.*, 2016, **138**, 9119–9127.

13. A. Simon and K. Peters, *Acta Cryst.*, 1980, **B36**, 2750-2751.

14. S. P. Thompson, J. E. Parker, J. Potter, T. P. Hill, A. Birt, T. M. Cobb, F. Yuan and C. C. Tang, *Rev. Sci. Instrum.*, 2009, **80**, 075107.

15. P. W. Stephens, *J. Appl. Cryst.*, 1999, **32**, 281-289.

Chapter 3

Separation of C_8 Aromatic Hydrocarbons in MFM-300

3.1 Introduction

The first study into separation of C_8 aromatic hydrocarbons using a MOF was reported by Denayer *et al.* in 2008 using the MOF MIL-47.[1] From competitive batch adsorption in the liquid phase, it was found that the MOF did show selectivity in adsorption of *p*-xylene over either *m*-xylene and ethylbenzene. The selectivity increased with the concentration of adsorbate. As more of the xylene molecules entered the pore, their stacking within the confined space became more important.

Similar work performed by Chen *et al.* in 2009 using a Zn based MOF with intersecting 3-dimensional pores.[2] This study saw preferential adsorption of *o*-xylene over *m*-xylene and *p*-xylene which was ascribed to the *o*-xylene---MOF interactions being stronger than that of *m*-xylene and *p*-xylene. This conclusion enforces the notion that studies of guest-host interactions are important in this field.

A study by Millange *et al.*[3] investigated the liquid phase separation of xylene isomers in MIL-53(Fe), and found that the material was successful at separating *p*-xylene, *o*-xylene and *m*-xylene. These results were coupled with high resolution PXRD studies of xylene-loaded MIL-53(Fe), in which the *p*-xylene structure was found to undergo a monoclinic → orthorhombic phase change.

More recently, Stoddart *et al.*[4] demonstrated the separation of *o*-xylene, *m*-xylene and *p*-xylene in a carbohydrate-based MOF. In this study they found that a large range of particle sizes can result in poorly resolved peaks, and proposed a method for the control of the particle size of their MOF, which greatly improved peak resolution. Using GCMC simulations they revealed that *o*-xylene could stack in a preferred parallel-displaced π- π stacking arrangement within the channel of the

MOF whereas *m*-xylene and *p*-xylene could not. This explained the much higher retention time observed for this *o*-xylene.

3.2 Aims of this Work

The aims of this work were to use high resolution PXRD to investigate the nature of the binding interactions between the isostructural MOFs MFM-300(Al),[5] MFM-300(V), and MFM-300(In),[6] and *m*-xylene, *o*-xylene, *p*-xylene and ethylbenzene.

Further to this, both the vapour phase adsorption behaviour and liquid phase separation properties of these 3 materials were investigated, the latter using HPLC-type methods and binary breakthrough experiments.

3.3 Results and Discussion

3.3.1 MFM-300(M) (M = Al, V, In) and C_8 Hydrocarbon Properties

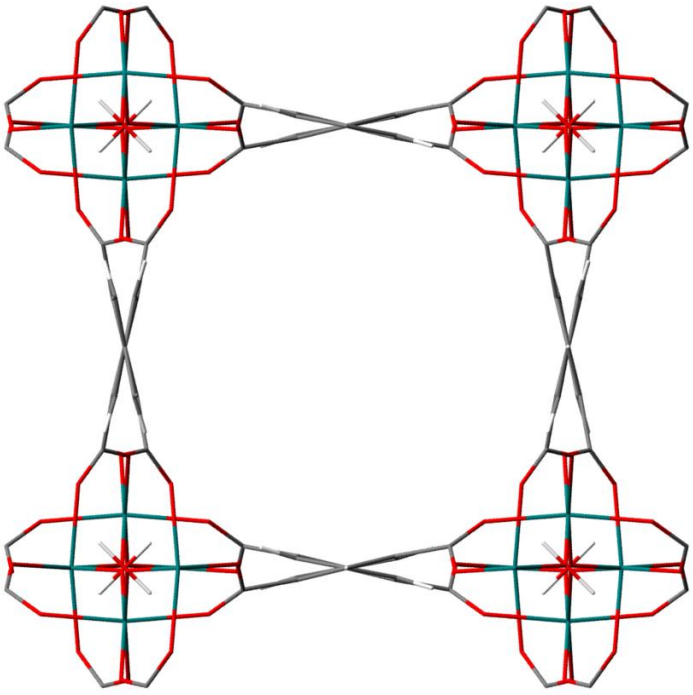


Figure 3.1 – square channel of MFM-300(M) as viewed down *c*-axis.

Structurally, the MOFs comprise $MO_4(OH)_2$ (M = Al, V, In) chains bridged by biphenyl tetracarboxylate ions, in tetragonal space group $I4_122$, resulting in a three dimensional framework with one dimensional square channels along the *c*-axis, as shown in Figure 3.1. Due to the variation in M-O bond lengths between the three metals, the size of this channel varies (Table 3.1), resulting in different properties for each MOF.

Table 3.1 – properties of MFM-300(M) (M=Al, V, In)

	Channel Size (Å)[a]	Surface Area (m^2 g^{-1})	Pore Volume (cc g^{-1})
MFM-300(Al)	7.08	1,370[b]	0.375[b]
MFM-300(V)	7.30	1,892[b]	0.490[b]
MFM-300(In)	7.55	1,071[c]	0.419[d]

[a] Measured from crystal structure across the pore, parallel to the *a* and *b* axes, using the same position in each MOF
[b]Calculated by DFT from CO_2 isotherm at 273K
[c]Calculated by BET
[d]Determined from N_2 isotherm at 77K

Due to the differences in size and dipole moment of ethylbenzene, *m*-, *o*- and *p*-xylene (Table 3.2), it was hypothesised that the differences in properties of MFM-300(M) (M = Al, V, In) could be used to achieve separation of the hydrocarbons.

Table 3.2 - Properties of C_8 hydrocarbons. Obtained from references 7-9.

	Boiling Point (K)	Dipole Moment (D)	σ^a (nm^2)	Kinetic Diameter[d] (Å)	X^b (Å)	Y^b (Å)	Z^b (Å)
m-xylene	412	0.30	0.379	6.80	8.994	3.949	7.315
o-xylene	417	0.45	0.375	6.80	7.269	3.834	7.826
p-xylene	411	0.02	0.380	5.85	6.618	3.810	9.146
Ethylbenzene	409	0.37	0.368	6.00	6.625	5.285	9.361

[a]Molecule cross-sectional area
[b]X, Y and Z are molecular width, thickness and length respectively

3.3.2 High Resolution PXRD Study

To understand how the each of the C_8 hydrocarbons interacts with the different frameworks, high resolution PXRD data was collected on beamline I11 at DLS. To prepare the samples for PXRD, MFM-300(Al), MFM-300(V), and MFM-300(In) were each activated at 120°C under vacuum for 48 hours and submerged in in 2 ml of each of the C_8 hydrocarbons for 4 weeks. This duration was deemed sufficient to account for the potentially slow kinetics of diffusion into the pores of the MOFs, in particular the smaller pores of MFM-300(Al). Worth noting is that in the MFM-300(Al) and MFM-300(In) structures, hydroxyl-bound water molecules are still present. In the MFM-300(V) structures, however, there are no water molecules present due to the lack of hydroxyl as a result of the V^{III} to V^{IV} oxidation.

3.3.2.1 C_8 Hydrocarbon-loaded MFM-300(Al)

Rietveld refinements were performed on the data, in which guest molecules were treated as rigid bodies with refined bond lengths and the framework was soft-

restrained to allow a degree of flexibility. The positions of the guest molecules was initially found using a simulated annealing global optimisation, followed by Rietveld refinement. Finally, the framework was refined, resulting in excellent fits.

3.3.2.1.1 Meta-xylene loaded MFM-300(Al)

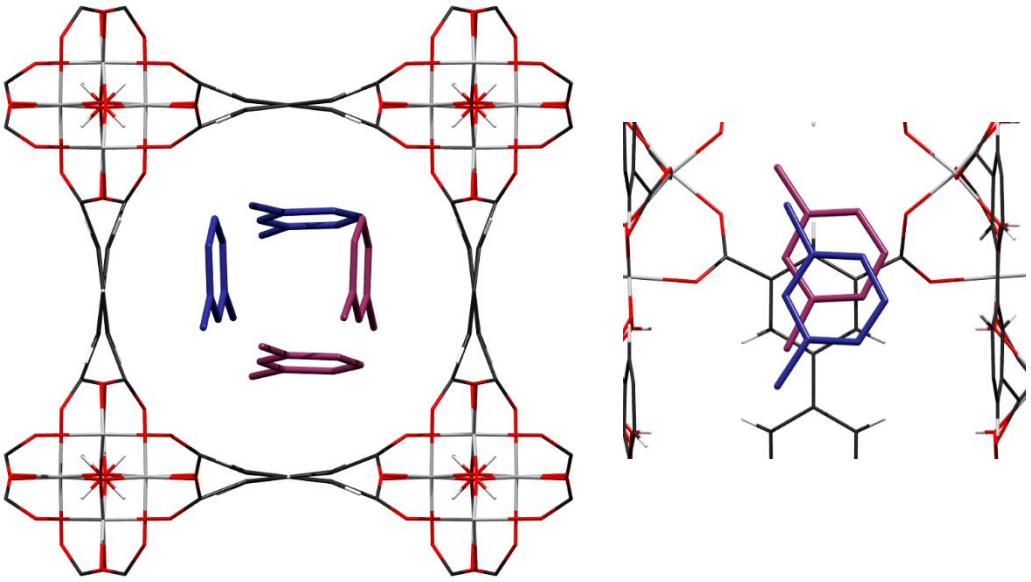


Figure 3.2 – (left) square channel of MFM-300(Al)-m-xylene as viewed down *c*-axis; (right) top view of host-guest interaction.

The structure of MFM-300(Al)(*m*-xylene) is shown in Figure 3.2. There are eight positionally disordered *m*-xylene molecules in the channel with an occupancy of 0.45 for each molecule, however only half of the molecules are shown here for clarity, due to steric clashes. The *m*-xylene molecules sit almost parallel to the phenyl ring of the framework at a distance of 3.42 Å, indicative of a π-π stacking interaction, with the methyl substituents pointing along the channel, away from the framework. Also present are π-π interactions between the guest molecules, which are 3.90 Å apart in a parallel-displaced arrangement. There appear to be no further interactions present between the framework and the *m*-xylene molecules.

3.3.2.1.2 Ortho-xylene loaded MFM-300(Al)

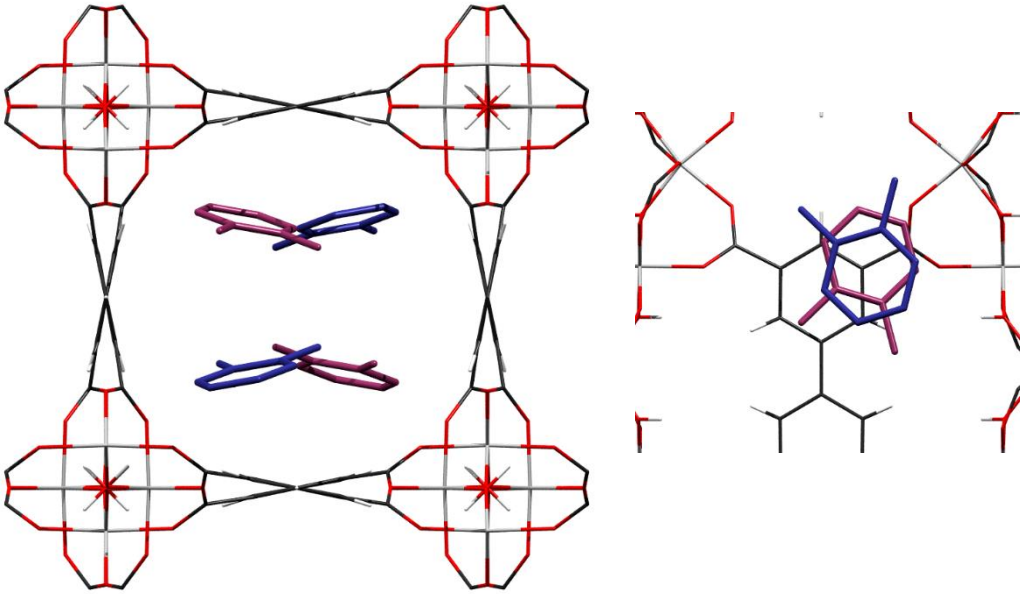


Figure 3.3 – (left) square channel of MFM-300(Al)-o-xylene as viewed down *c*-axis; (right) top view of host-guest interaction.

The structure of MFM-300(Al)(*o*-xylene) (Figure 3.3), similarly to MFM-300(Al)(*m*-xylene), comprises eight positionally disordered *o*-xylene molecules at an occupancy of 0.42. The maximum possible occupancy for these molecules is 0.5 due to steric clashes. The guest molecules exhibit parallel displaced π-π stacking interaction at a distance of 3.52 Å from the phenyl ring of the framework, with the methyl substituents pointing away from the framework. Guest-guest π-π interactions are also present at a distance of 3.65 Å.

3.3.2.1.3 Para-xylene loaded MFM-300(Al)

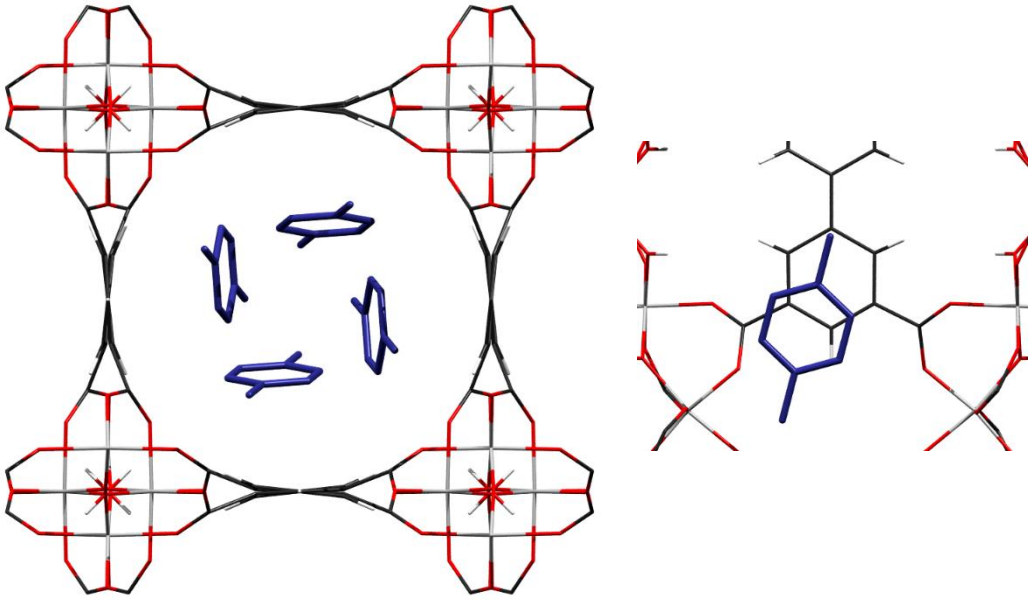


Figure 3.4 – (left) square channel of MFM-300(Al)-*p*-xylene as viewed down *c*-axis; (right) top view of host-guest interaction.

The structure of MFM-300(Al)(*p*-xylene) (Figure 3.4) again has eight postionally disordered guest molecules in the channel at an occupancy of 0.47, forming π-π interactions with the phenyl ring of the framework at a distance of 3.47 Å with the methyl substituents pointing along the channel. There are no guest-guest interactions present, a direct result of the methyl groups prohibiting a molecule further along the pore co-existing with the molecule occupying this site.

3.3.2.1.4 Ethylbenzene loaded MFM-300(Al)

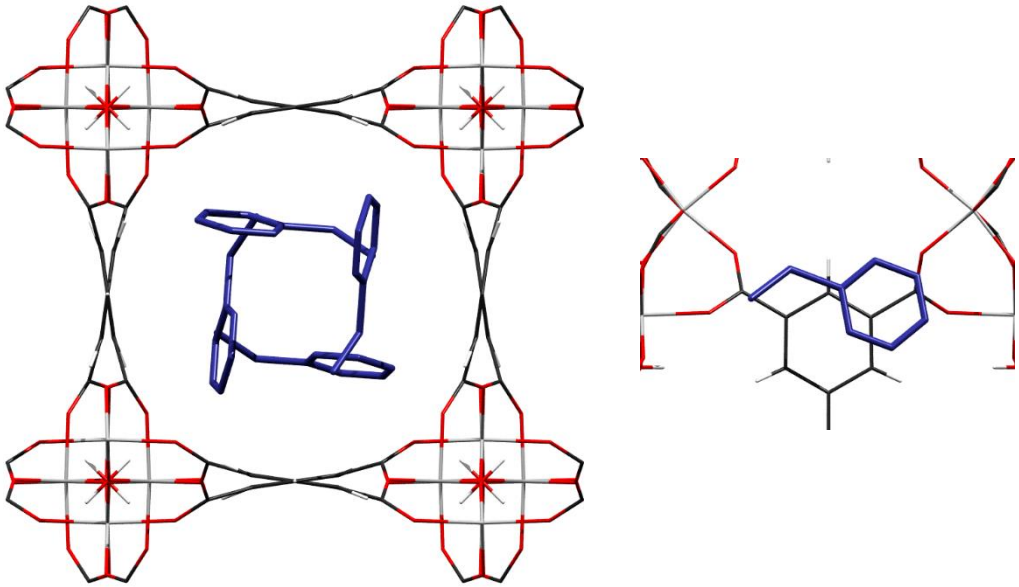


Figure 3.5– (left) square channel of MFM-300(Al)-ethylbenzene as viewed down *c*-axis; (right) top view of host-guest interaction.

The structure of MFM-300(Al)(ethylbenzene) (Figure 3.5) comprises eight positionally disordered ethylbenzene molecules at half occupancy. Each molecule forms an offset π-π stacking interaction 3.61 Å with the methyl group of the ethyl substituent pointing to the centre of the channel. Similarly to in MFM-300(Al)(*p*-xylene), the position of the substituents prevents π-π stacking of the guest molecules.

3.3.2.1 C_8 Hydrocarbon-loaded MFM-300(V)

The structures of C_8 hydrocarbon-loaded MFM-300(V) were determined using similar methods to those used for MFM-300(Al). Worth noting, however, is that during the activation procedure, MFM-300(V) oxidised from V^{III} to V^{IV}. This was apparent from a green to brown colour change and also a significant reduction in crystallinity.

3.3.2.1.1 Meta-xylene loaded MFM-300(V)

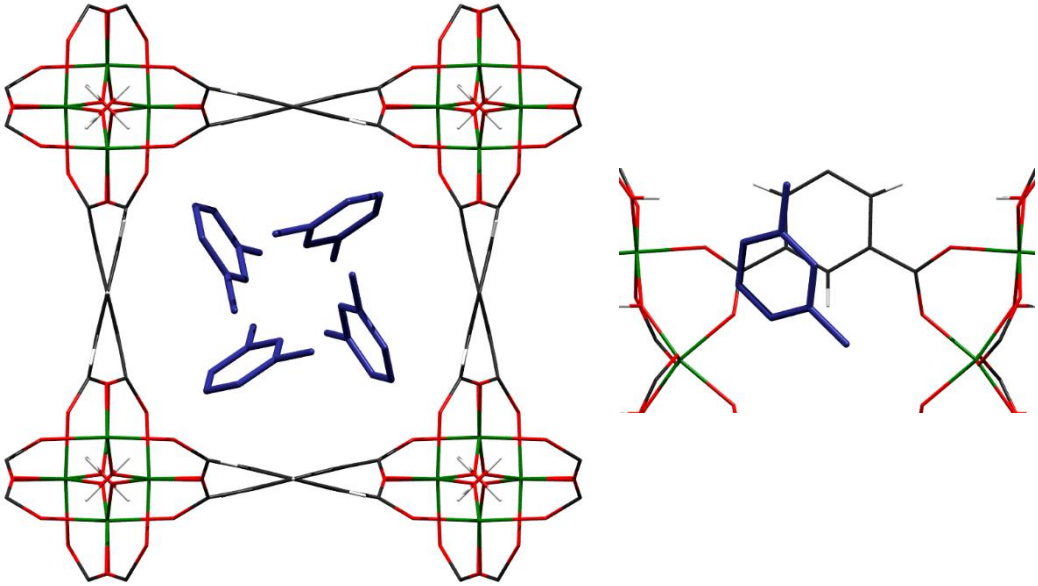


Figure 3.6– (left) square channel of MFM-300(V)-m-xylene as viewed down *c*-axis; (right) top view of host-guest interaction.

Figure 3.6 shows the structure of MFM-300(V)(*m*-xylene). The structure comprises eight positionally disordered *m*-xylene molecules at half occupancy. The *m*-xylene molecules sit almost parallel to the phenyl ring of the framework and form an offset π-π stacking interaction at a distance of 3.54 Å. Unlike the MFM-300(Al)(*m*-xylene) structure, there is no guest-guest π-π stacking present, which is likely due to the larger pore of MFM-300(V) having less of a confinement effect.

3.3.2.1.2 Ortho-xylene loaded MFM-300(V)

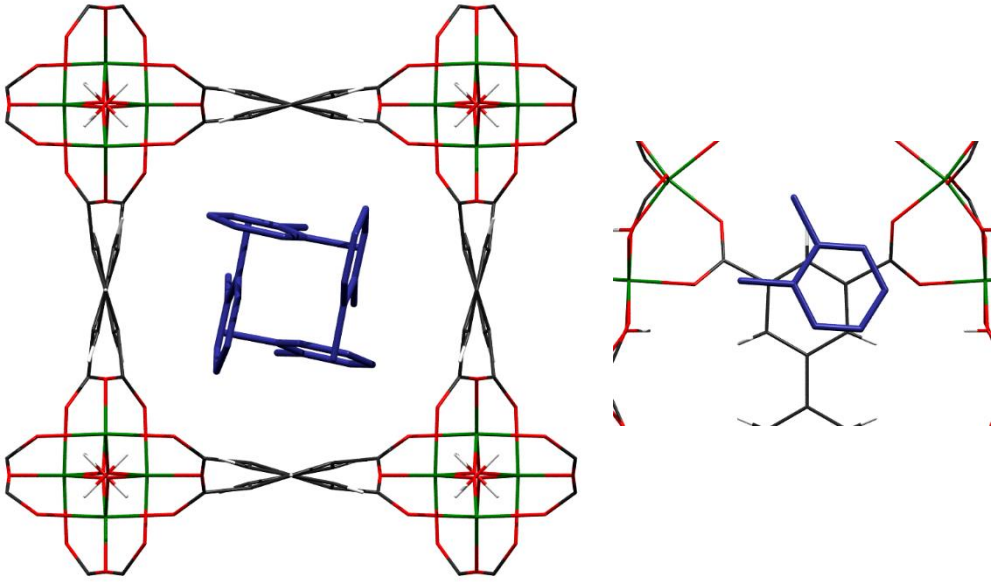


Figure 3.6– (left) square channel of MFM-300(V)-o-xylene as viewed down *c*-axis; (right) top view of host-guest interaction.

The structure of MFM-300(V)(*o*-xylene) is shown in Figure 3.7. The guest molecule sits parallel to the framework's phenyl at a distance of 3.85 Å, indicating a π-π stacking interaction. Again, there are no guest-guest π-π interactions present, unlike the structure of MFM-300(Al)(*o*-xylene), due to the larger pores of MFM-300(V) causing less confinement.

3.3.2.1.3 Para-xylene loaded MFM-300(V)

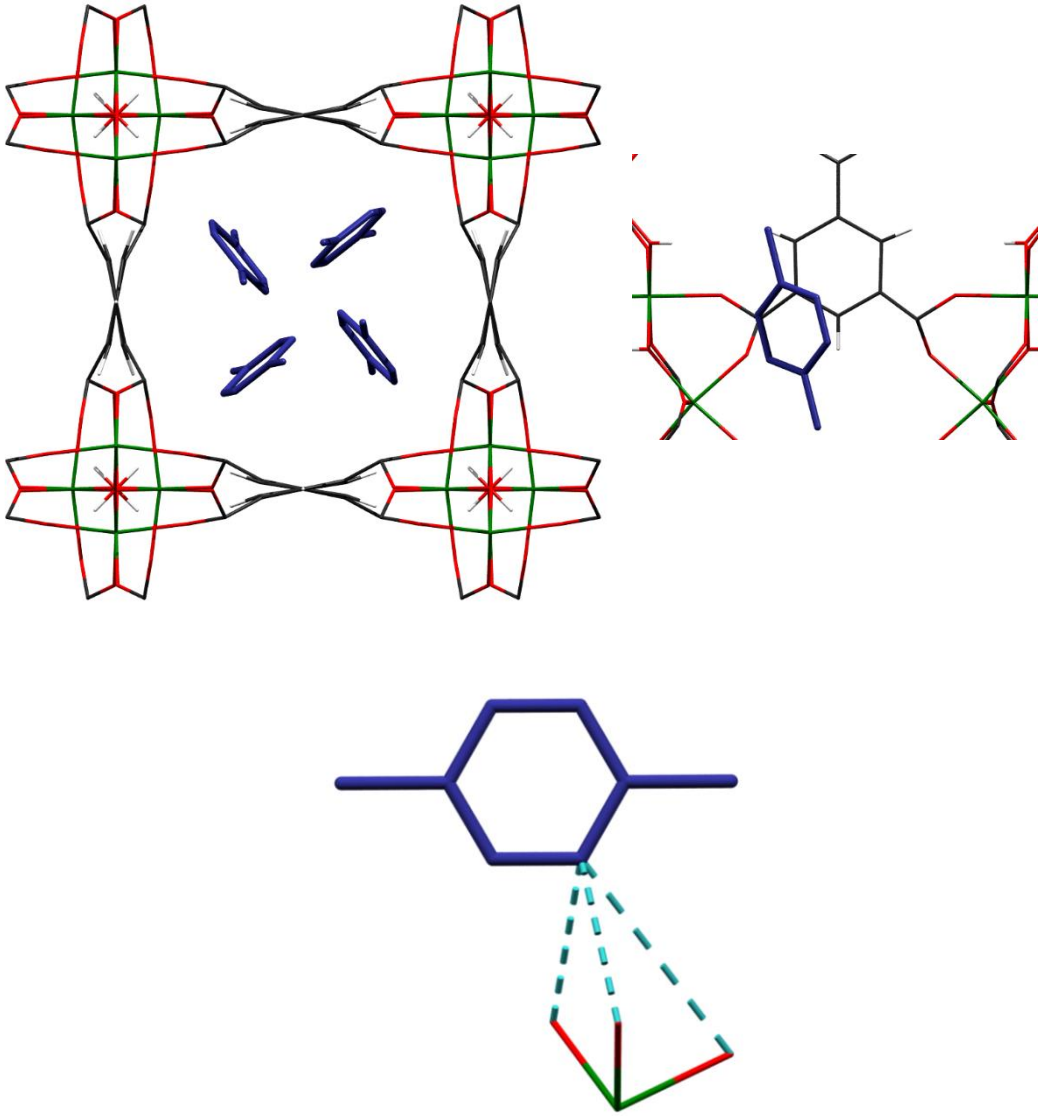


Figure 3.7– (top-left) square channel of MFM-300(V)-p-xylene as viewed down *c*-axis; (top-right) top view of host-guest interaction; (bottom) proximity of C atom of xylene to O atoms of VO_6 octahedron.

Figure 3.7 shows the structure of MFM-300(V)(*p*-xylene). The *p*-xylene molecule sits 3.87 Å from the phenyl ring of the framework, which is in the range of a π-π interaction, however it is somewhat skewed from the central position of the channel. This may be due to a C-H interaction with the oxygen atoms of the VO_6 octahedron.

A carbon atom points into a ‘pocket’ of three oxygen atoms with C---O distances of around 3 Å.

3.3.2.1.4 Ethylbenzene loaded MFM-300(V)

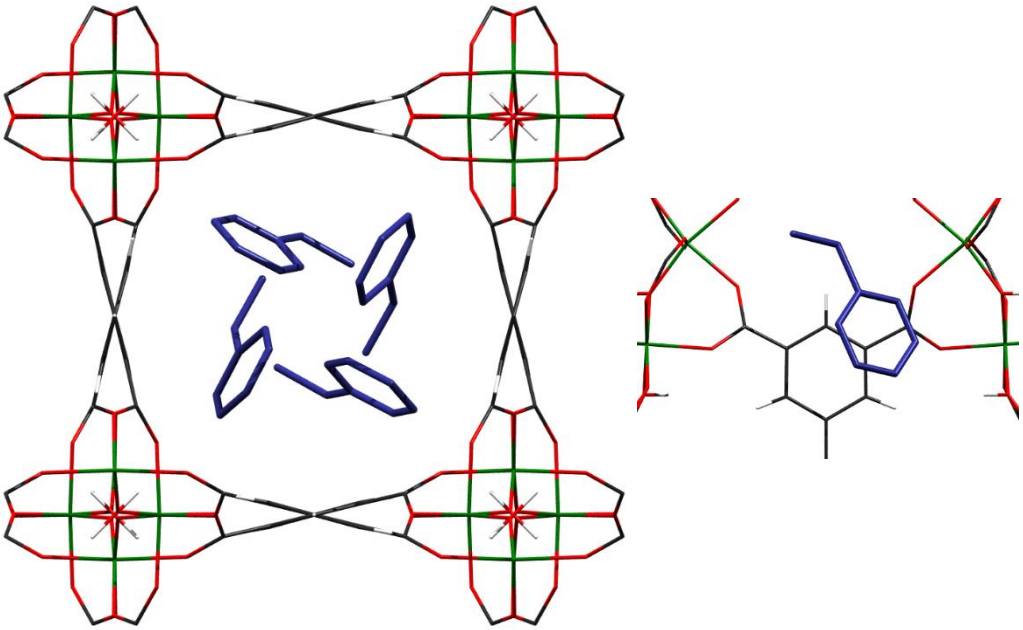


Figure 3.8– (left) square channel of MFM-300(V)-ethylbenzene as viewed down *c*-axis; (right) top view of host-guest interaction.

The structure of MFM-300(V)(ethylbenzene) (Figure 3.8) again shows a π-π stacking interaction between the framework’s phenyl ring and the guest molecule, at a distance of 3.75 Å.

3.3.2.1 C_8 Hydrocarbon-loaded MFM-300(In)

Rietveld refinements were carried out on the data in similar ways to those done for MFM-300(Al) and MFM-300(V). One main difference in the MFM-300(In) results, however, is a tetragonal $I4_122$ to orthorhombic $I2_12_12_1$ phase change in MFM-300(In)(*p*-xylene). As $I2_12_12_1$ is a maximal subgroup of $I4_122$, the framework’s

$I2_12_12_1$ structure was generated from the $I4_122$ phase using the TRANSTRU structure utility on the Bilbao Crystallographic Server and the transformation matrix (**P**, p): **a**,**b**,**c** ; 0,1/4,3/8.

3.3.2.1.1 Meta-xylene loaded MFM-300(In)

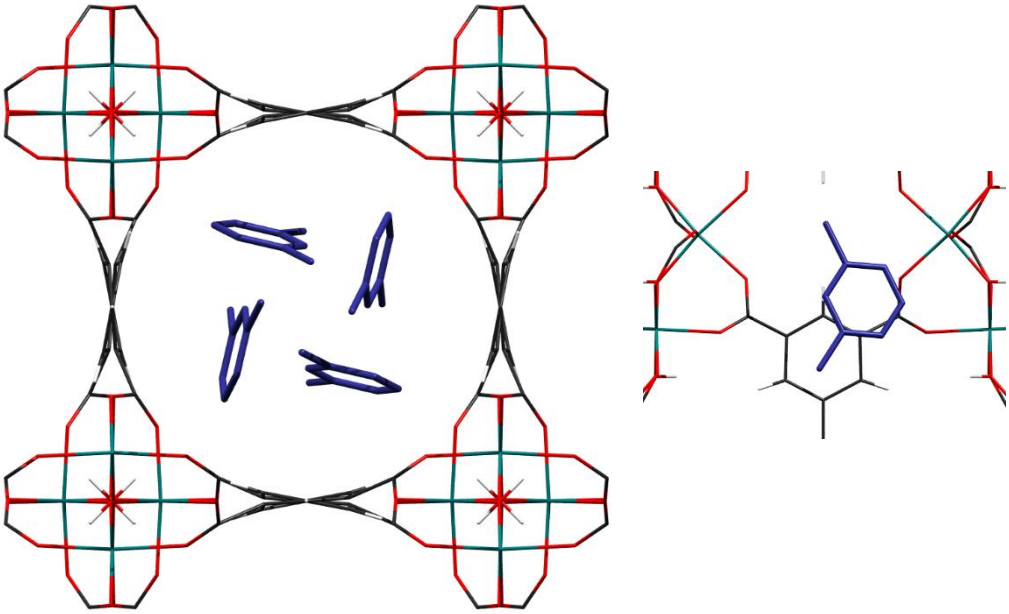


Figure 3.9– (left) square channel of MFM-300(In)-m-xylene as viewed down *c*-axis; (right) top view of host-guest interaction.

The structure of MFM-300(In)(*m*-xylene) (Figure 3.9) comprises eight positionally disordered *m*-xylene molecules at an occupancy of 0.48. Half of the molecules were deleted for clarity. The guest interacts at a distance of 3.74 Å from the framework's phenyl ring in an offset π-π interaction. Similarly to the structure of MFM-300(V)(*m*-xylene), there is not enough of a confinement effect to cause guest-guest π-π interactions.

3.3.2.1.2 Ortho-xylene loaded MFM-300(In)

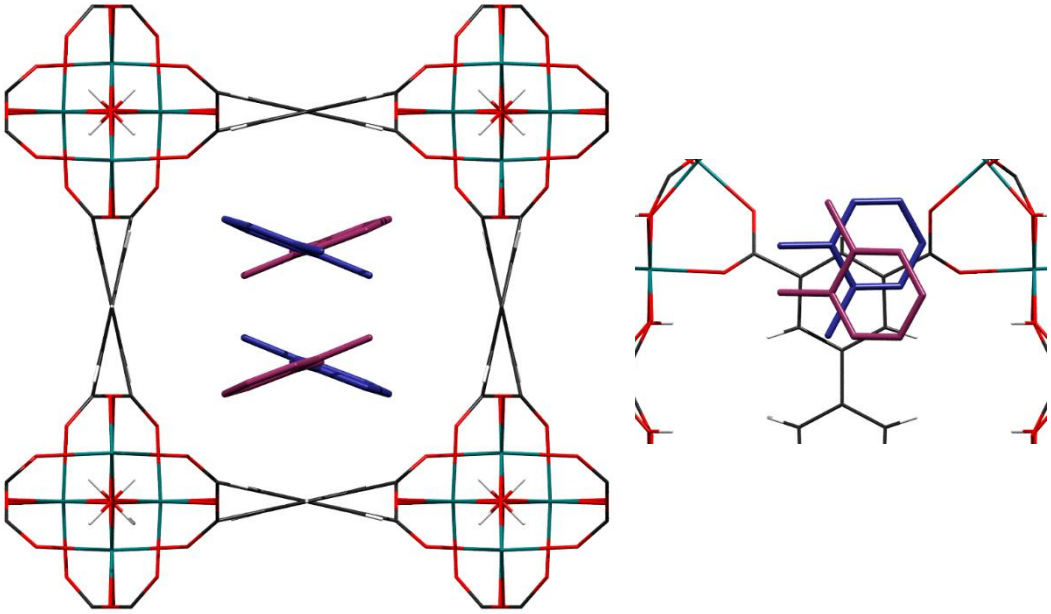


Figure 3.10– (left) square channel of MFM-300(In)-o-xylene as viewed down *c*-axis; (right) top view of host-guest interaction.

The structure of MFM-300(In)(*o*-xylene) is shown in Figure 3.10. There are eight positionally disordered *o*-xylene molecules at an occupancy of 0.47 which sit parallel to the framework's phenyl ring at a distance of 3.67 Å. Although from the Figure 3.10 it appears that there may be guest-guest π-π interactions present, the lack of parallelity between the guests suggests that this is not the case.

3.3.2.1.3 Para-xylene loaded MFM-300(In)

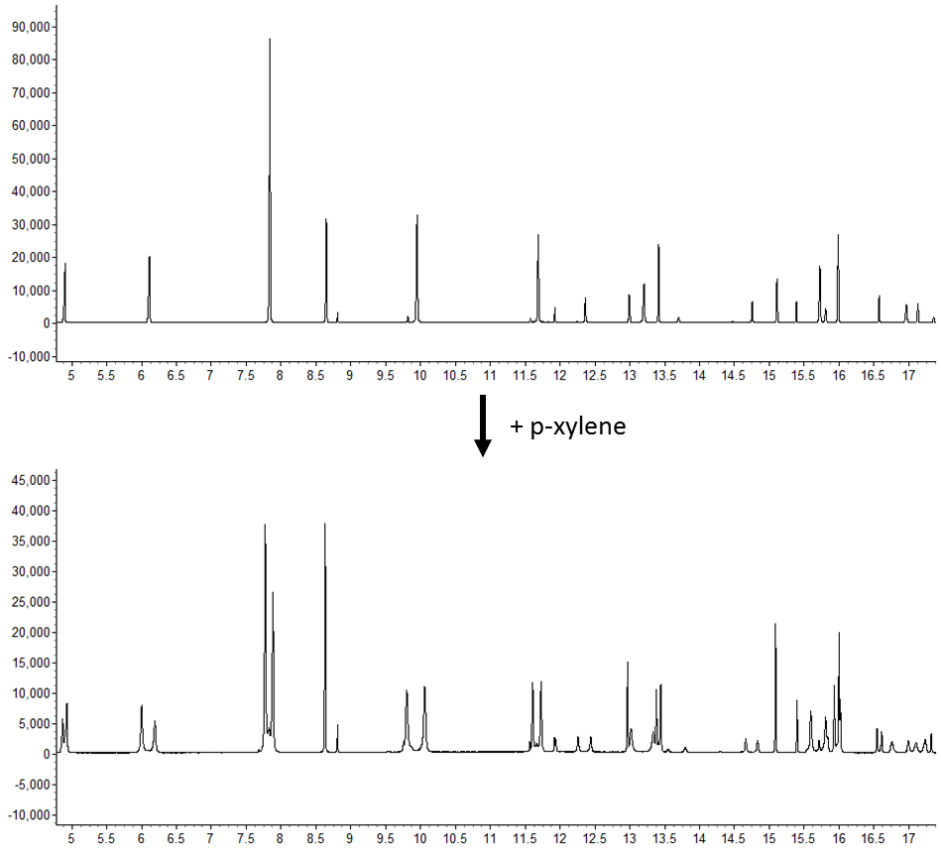


Figure 3.11– powder diffractograms showing tetragonal → orthorhombic phase change in MFM-300(In).

The most noteworthy observation in the structure of MFM-300(In)(*p*-xylene) is a tetragonal $I4_122$ to orthorhombic $I2_12_12_1$ phase change (Figure 3.11). This $I4_122$ → $I2_12_12_1$ phase change for the MFM-300 structure was predicted by Coudert *et al.*[10] who computationally demonstrated that applying a tetragonal shear would result in framework deformation, but until now, the flexible nature of this structure has not been demonstrated experimentally.

The structures of the two phases are shown in Figure 3.12. The phase change is accompanied by a reduction in the torsion angle of the phenyl rings in the linker –

14(2)° in this case, compared to 25.2(4)° in the MFM-300(In)(*o*-xylene) structure – and a slight distortion in the InO_6 octahedron, which combine to cause a contraction of the *a*-axis and an elongation of the *b*-axis. These subtle changes cause the square shape of the 1D channel to distort slightly into a lozenge shape.

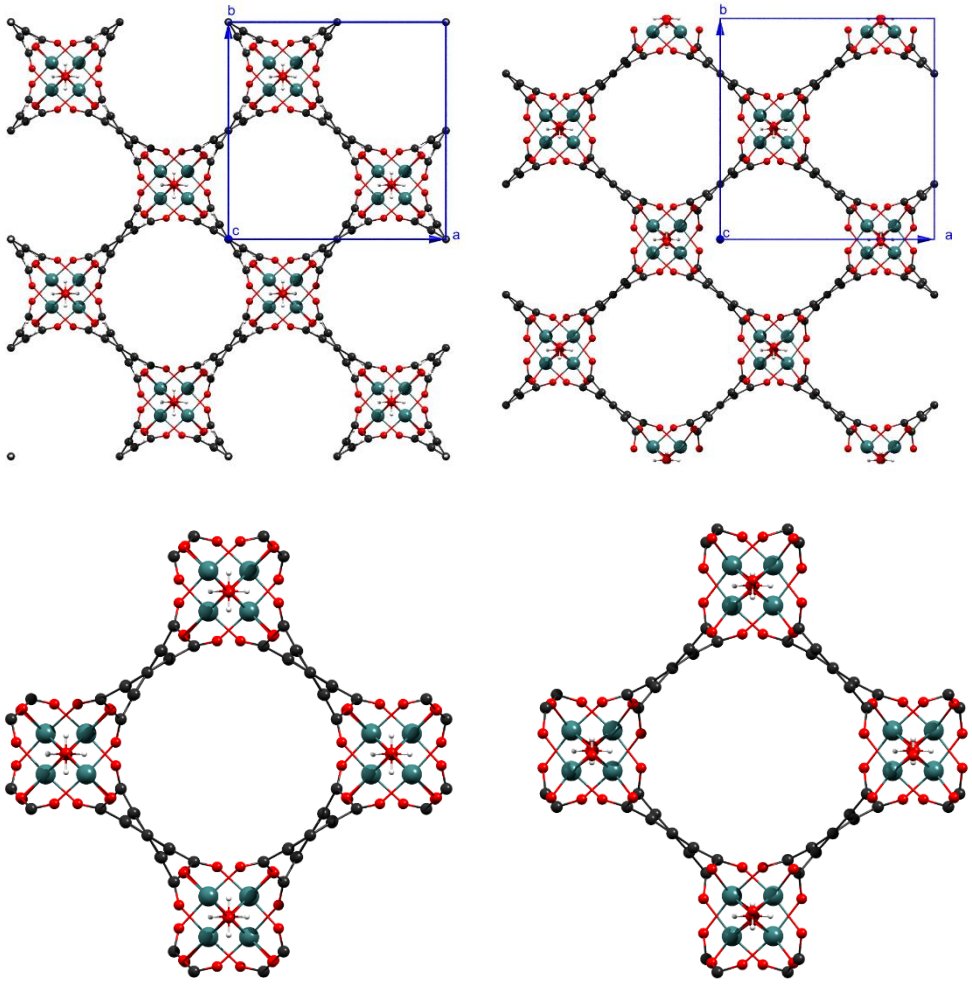


Figure 3.12– (top left) 2x2 supercell of tetragonal MFM-300(In); (top right) 2x2 supercell of orthorhombic MFM-300(In); (bottom left) view of channel of tetragonal MFM-300(In); (bottom right) view of channel of orthorhombic MFM-300(In).

It should be noted that the phase change did not go to completion, as the PXRD pattern indicates the presence of around 4% of the original $I4_122$ phase (Figure 3.14). This suggests that the kinetics of this *p*-xylene induced transition are slow.

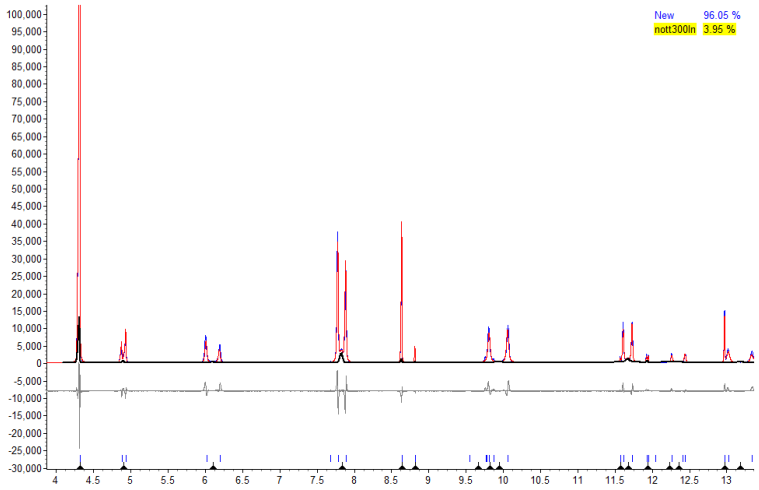


Figure 3.14 – powder diffractogram showing presence of 4% tetragonal phase (black line)

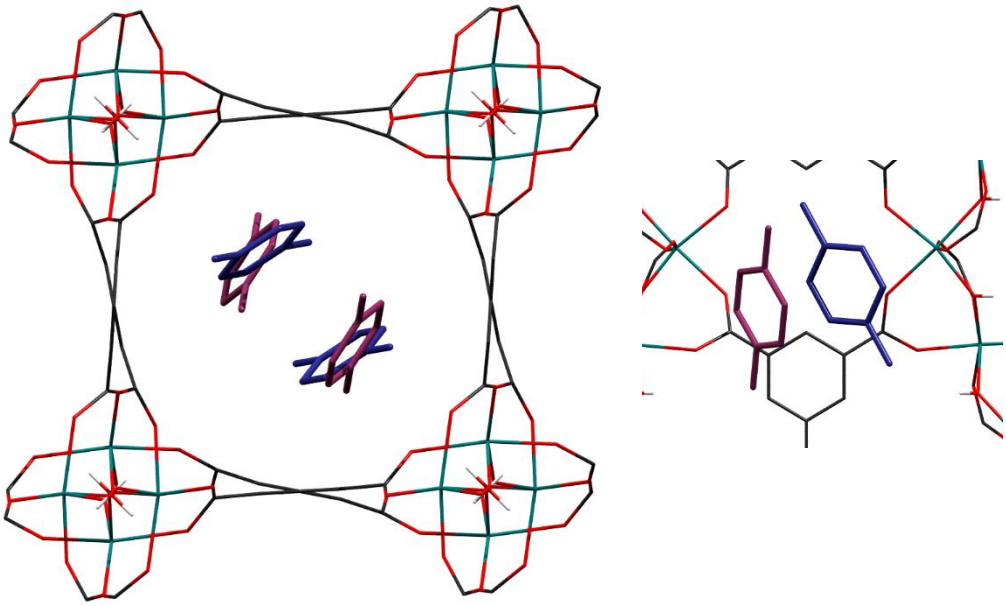


Figure 3.15 – (left) lonzenge shaped channel of MFM-300(In)-*p*-xylene as viewed down *c*-axis; (right) top view of host-guest interaction.

The structure of *p*-xylene loaded MFM-300(In) is shown in Figure 3.15. The structure comprises four *p*-xylene molecules at 0.74 occupancy. These molecules exhibit a C-H---π-system interaction with the framework (*p*-xylene to framework phenyl ring), with the closest distance from the C atom of the *p*-xylene to the centre of the framework's phenyl ring being 3.27 Å.

3.3.2.1.4 Ethylbenzene loaded MFM-300(In)

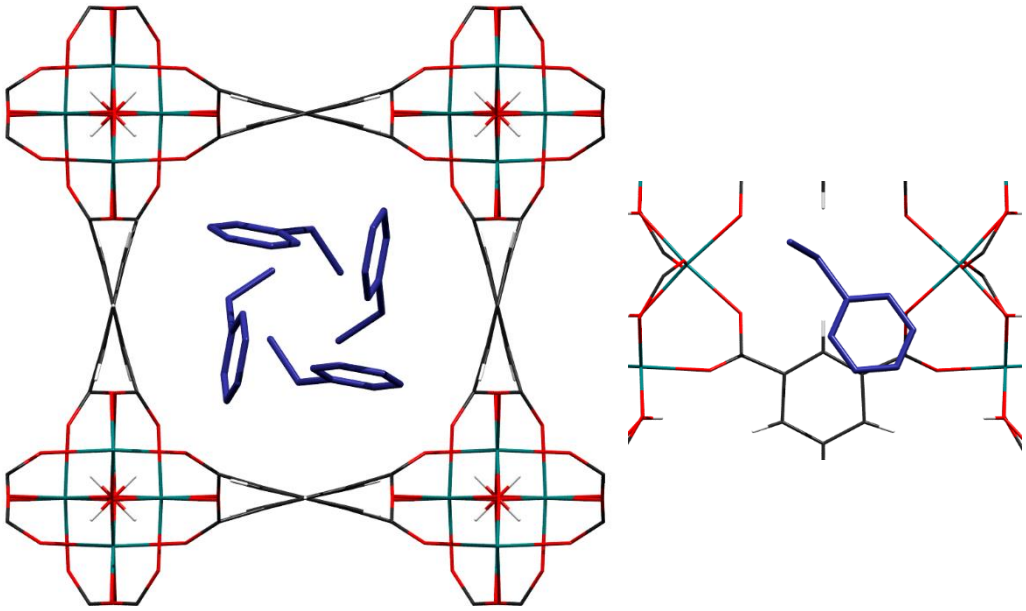


Figure 3.16 – (left) square channel of MFM-300(In)-ethylbenzene as viewed down *c*-axis; (right) top view of host-guest interaction.

The structure of MFM-300(In)(ethylbenzene) is shown in Figure 3.16. The structure comprises eight positionally disordered ethylbenzene molecules, forming a π-π interaction with the phenyl ring of the framework at a distance of 3.97 Å.

3.3.2.4 Summary of Hydrocarbon-loaded MFM-300(M) Structures

Occupancies and π-π distances from each of the reported MFM-300(M) structures are summarised in Table 3.3. All structures exhibit π-stacking between the phenyl ring of the framework and the hydrocarbon molecule.

Table 3.3 - Summary of host-guest π-π distances and occupancies in the structures of hydrocarbon-loaded MFM-300(M). mX = *m*-xylene; oX = *o*-xylene; pX = *p*-xylene; Eb = ethylbenzene.

Metal	Hydrocarbon	Host-Guest π-π distance (Å)	Occupancy
Al	mX	3.42	0.45
	oX	3.52	0.42
	pX	3.47	0.47
	Eb	3.61	0.5
V	mX	3.54	0.5
	oX	3.85	0.5
	pX	3.87	0.5
	Eb	3.75	0.5
In	mX	3.74	0.48
	oX	3.67	0.47
	pX	3.27	0.74[a]
	Eb	3.97	0.5

[a]Maximum occupancy in this case is 1.0 as opposed to 0.5 in other structures

3.3.2.5 High Pressure PXRD of MFM-300

According to Coudert *et al.*,[10] the MFM-300(Al) undergoes continuous phase transition between 0-1 GPa of shear stress with no significant change observed beyond 1 GPa (Figure 3.17). The study also simulated applying an isotropic pressure to the system and found that a pressure of 0.7 GPa brings about the same phase change (Figure 3.18).

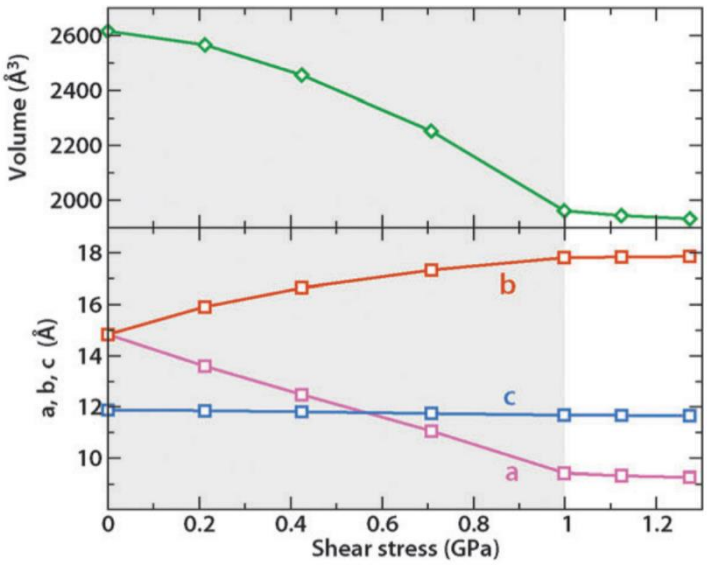


Figure 3.17 – Plot of unit cell parameters of MFM-300(Al) as a function of computational shear stress. Figure taken from reference 10.

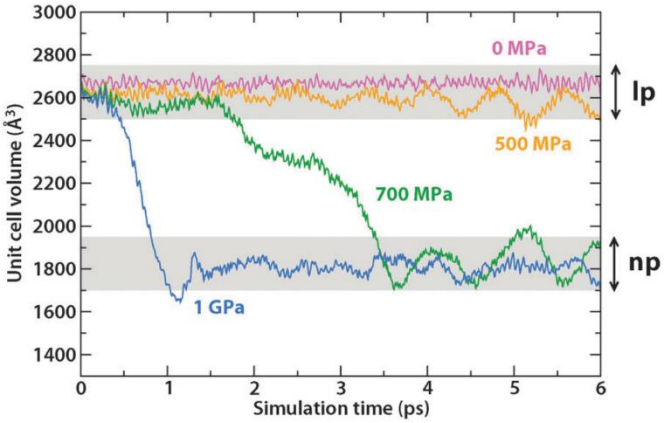


Figure 3.18 – Plot of cell volume of MFM-300(Al) as a function of simulation time. Figure taken from reference 10.

To experimentally validate these simulations and to further investigate the apparent flexible nature of MFM-300(In), a high pressure PXRD study was conducted. The MOF was pressurised in a DAC to 8 different pressures from 0 – 3.23 GPa inclusive, and then depressurised to ambient pressure. The MOF was activated prior to loading, and the PTM chosen was Fluorinert™ FC-70 (too large to enter the pore), to ensure that the pressure was acting on the MOF from outside the crystallites. The resulting PXRD data are shown in Figure 3.19.

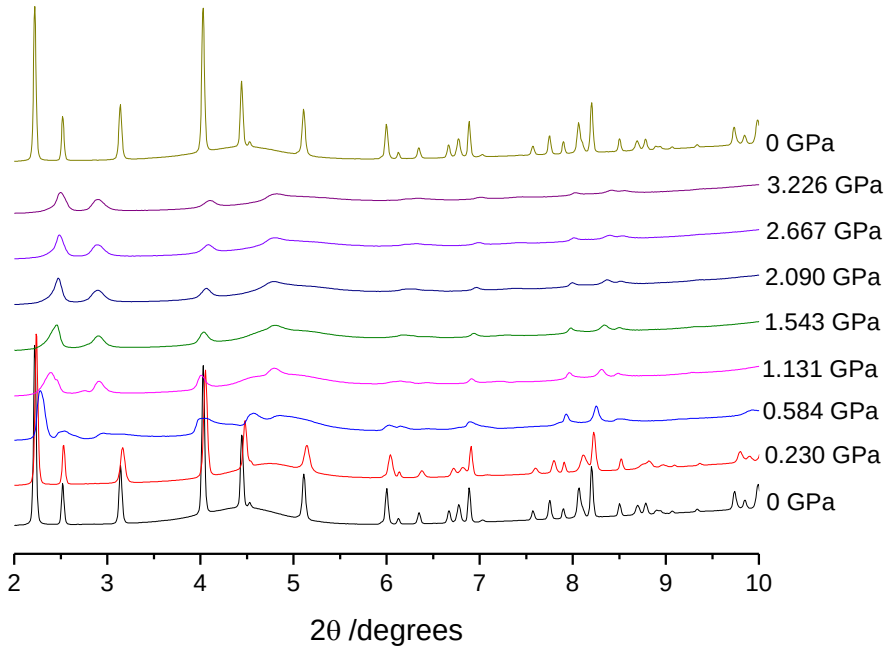


Figure 3.19– powder diffractograms of MFM-300(In) as a function of pressure.

The diffractograms were indexed, and it was found that the structure retained its tetragonal symmetry up to 0.584 GPa, where there was a tetragonal $I4_122$ → orthorhombic $I2_12_12_1$ phase change. On depressurisation of the cell, the original tetragonal symmetry returned, confirming the reversible nature of this transition. The cell parameters from this experiment are plotted as a function of pressure in Figure 3.20. The cell compresses from 0 to 0.230 GPa, and then upon increasing the pressure to 0.584 GPa, the *a*-axis decreases significantly, almost linearly, until 1.543

GPa is reached, at which point further changes are much more gradual. Conversely, the *b*-axis elongates as a function of pressure from 0.584 GPa. Unlike the *a*-axis, however, the change in the *b* parameter is not as severe, and begins to plateau from 1.131 GPa as opposed to 1.534 GPa. The *c*-axis, however, changes very little across the entire pressure range.

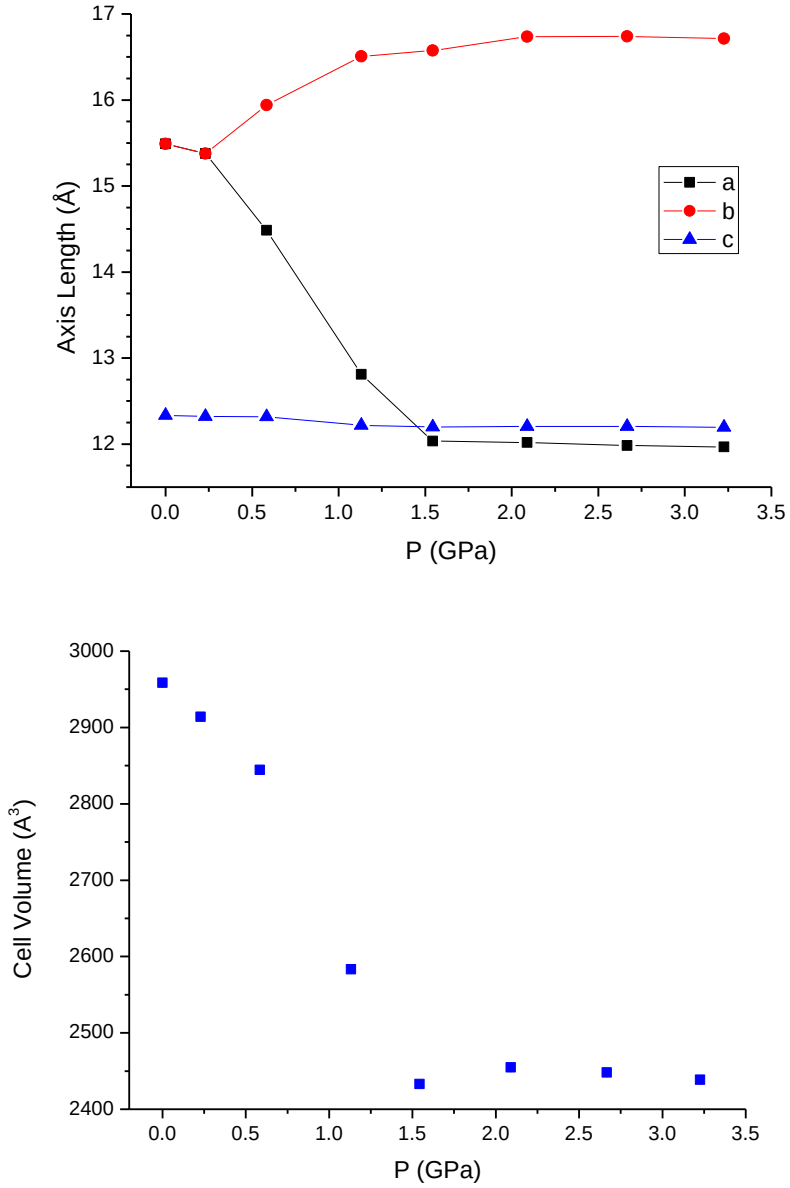


Figure 3.20 – unit cell parameters (top) and cell volume (bottom) of MFM-300(In) as a function of pressure.

The data of the high pressure phase was not of sufficient quality to obtain any further structural information *via* Rietveld refinement. However, based on the phase change in MFM-300(In)(*p*-xylene) and the results from the study by Coudert, coupled with the cell parameter variations, it is reasonable to suggest that the pore transitions from a square shape in the tetragonal system, to a lozenge shape as *a* and *b* diverge, until a relatively stable orthorhombic structure is reached at 1.543 GPa.

3.3.3 Vapour Adsorption

To investigate the C_8 hydrocarbon vapour adsorption properties of MFM-300(M) (M=Al, V, In), isotherms at were measured at 45 °C for each solvent in the different MOFs. After an initial trial run of *p*-xylene in MFM-300(In) at 30 °C revealed incredible slow kinetics of adsorption, the higher temperature of 45 °C was deemed sufficient. Each isotherm was performed after activation of the MOF under vacuum at 150 °C for 24 hours, to ensure complete removal of solvent from the pores.

3.3.3.1 MFM-300(Al) Isotherms

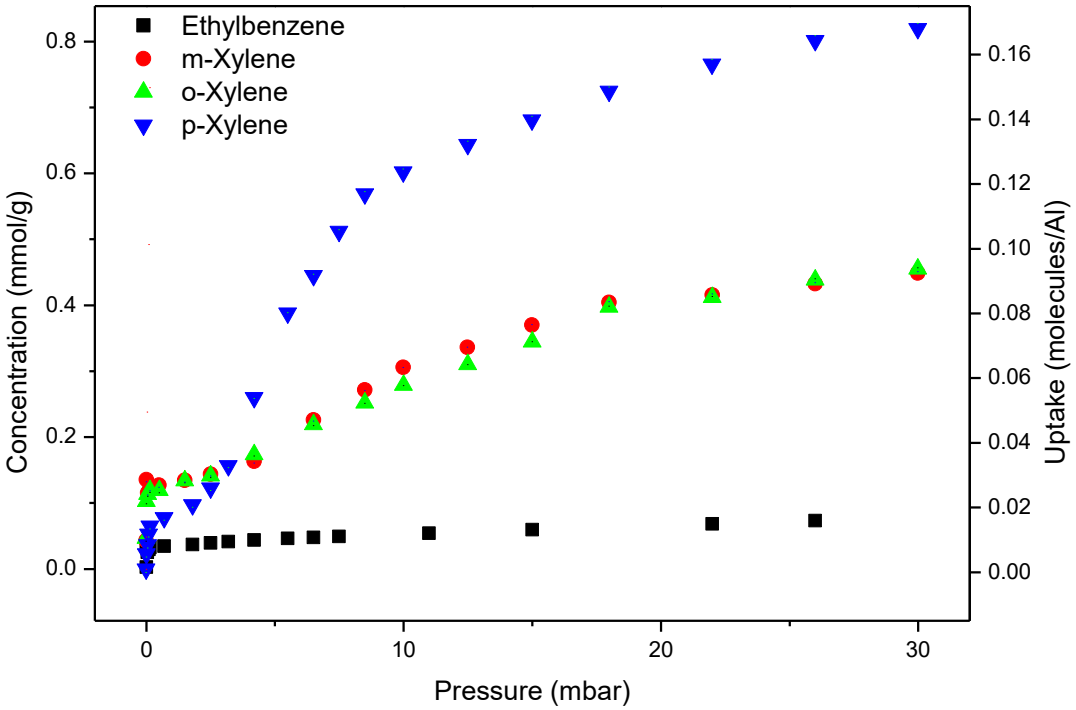


Figure 3.21 – C_8 hydrocarbon isotherms with MFM-300(Al) recorded at 45°C.

Figure 3.21 shows the adsorption isotherms of ethylbenzene, *m*-xylene, *o*-xylene and *p*-xylene in MFM-300(Al) at 45 °C. The MOF exhibits an extremely low uptake of ethylbenzene (0.073 mmol/g at 26 mbar) and the adsorption of both *m*-xylene and *o*-xylene is almost identical (0.449 mmol/g and 0.455 mmol/g respectively at 30 mbar) and both exhibit a similar isotherm shape. The uptake of *p*-xylene (0.82 mmol/g at 30 mbar), however, is almost double that of *m*- and *o*- xylene and over ten times that of ethylbenzene.

The adsorption profiles of *m*-, *o*-, and *p*-xylene correspond to a type IV isotherm, a phenomenon that has previously been observed in the adsorption of *p*-xylene in silicalite,[11] where it was found that the similarity in size between the adsorbate and pore channel resulted in this behaviour.

The similarity in uptake of *m*-xylene and *o*-xylene is likely due to their similar sizes, however, the large differences in uptake between *p*-xylene and ethylbenzene was unforeseen. The two molecules have similar kinetic diameters, and the high resolution PXRD study confirmed liquid-phase adsorption of each molecule. As the PXRD experiment involved storing the MOF under ethylbenzene for a period of four weeks, it is possible that the differences between ethylbenzene in the liquid phase and vapour phase is due to the kinetics of diffusion of ethylbenzene entering the pore. This may also explain why the overall uptakes of all four of the adsorbates is much higher in the PXRD experiment, ranging from 0.84-1.00 molecules per Al(III) as opposed to 0.02-0.17 molecules per Al(III) from the isotherms.

3.3.3.2 MFM-300(V) Isotherms

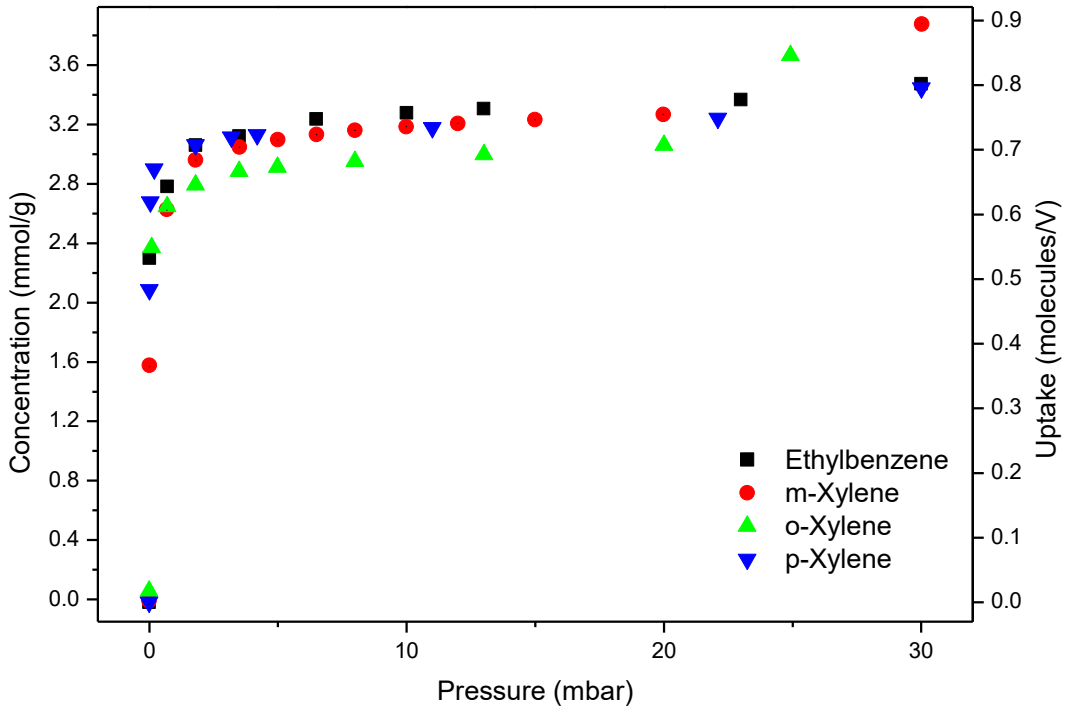


Figure 3.22 – C_8 hydrocarbon isotherms with MFM-300(V) recorded at 45°C.

Figure 3.22 shows the adsorption isotherms of ethylbenzene, *m*-xylene, *o*-xylene and *p*-xylene in MFM-300(V) at 45 °C. Unlike in MFM-300(Al), the uptake of all four compounds is fairly similar, with an ethylbenzene uptake of 3.47 mmol/g at 30 mbar, a *m*-xylene uptake of 3.88 mmol/g at 30 mbar, a *o*-xylene uptake of 3.67 mmol/g at 25 mbar, and a *p*-xylene uptake of 3.45 mmol/g at 30 mbar. In this case the adsorption profile of each adsorbate exhibits type I behaviour.

The number of molecules per metal is in much better agreement with the high resolution PXRD results than in the case of MFM-300(Al), due to the reduced effects of diffusion kinetics as a result of the larger pore of MFM-300(V).

3.3.3.3 MFM-300(In) Isotherms

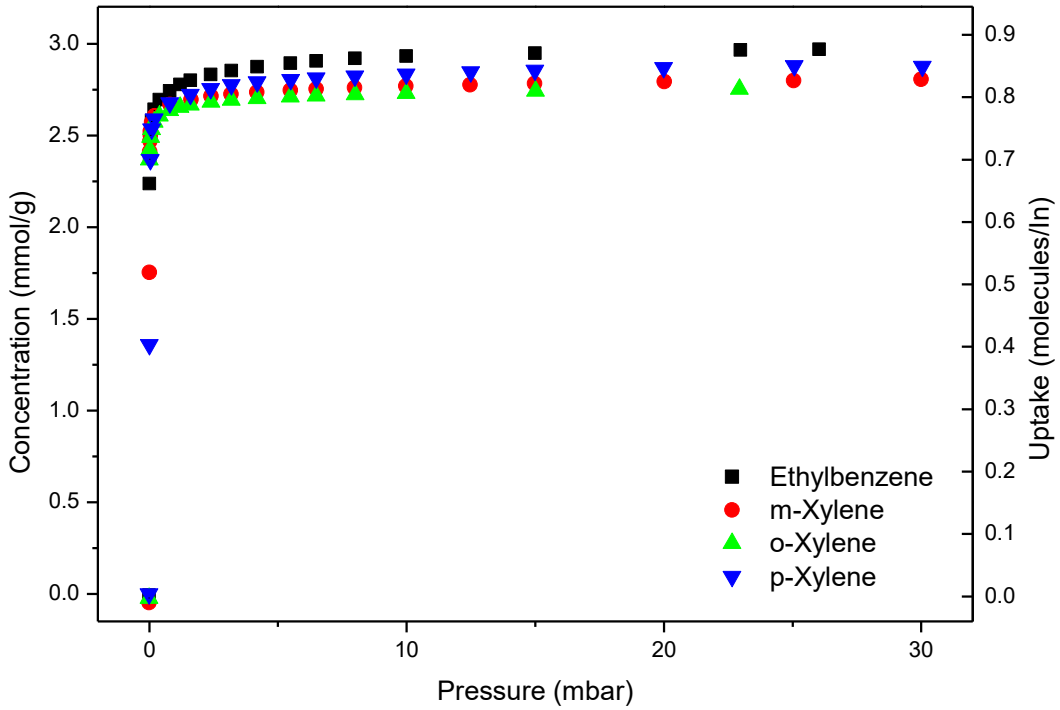


Figure 3.23 – C_8 hydrocarbon isotherms with MFM-300(In) recorded at 45°C.

Figure 3.23 shows the adsorption isotherms of ethylbenzene, *m*-xylene, *o*-xylene and *p*-xylene in MFM-300(In) at 45°C. All four adsorbates exhibit incredibly similar

uptakes, with an ethylbenzene uptake of 2.97 mmol/g at 26 mbar, a *m*-xylene uptake of 2.81 mmol/g at 30 mbar, a *o*-xylene uptake of 2.75 mmol/g at 23 mbar, and a *p*-xylene uptake of 2.87 mmol/g at 30 mbar. Similarly to MFM-300(V), each isotherm exhibits type I behaviour.

MFM-300(In) exhibits a higher uptake of adsorbates per metal atom compared both MFM-300(V) and MFM-300(Al) as a result of its larger pore size, and similarly to MFM-300(V), the agreement between the PXRD results and isotherms is much better than with MFM-300(Al).

3.3.4 Liquid-Phase Separation

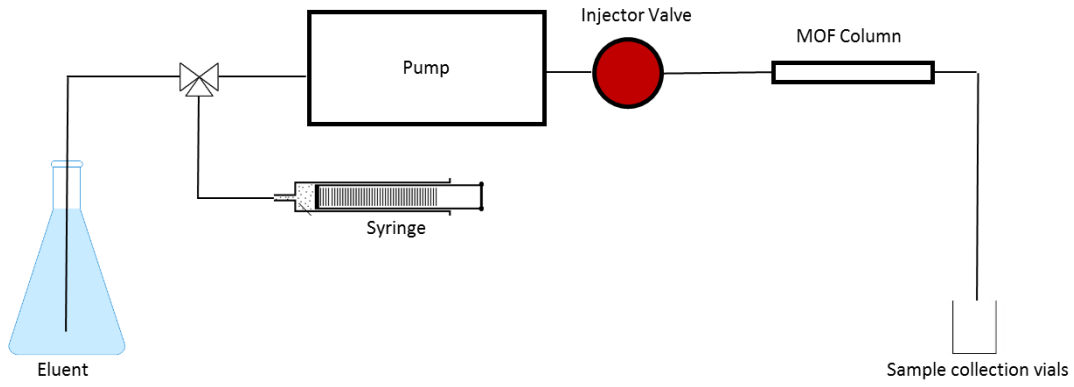


Figure 3.24 – Schematic of liquid phase separation rig

Figure 3.24 shows a schematic of the liquid phase separation rig used in these experiments. The syringe was used to prime the pump and to remove any air bubbles from the inlet tubing. A 6-way injector valve with 5 µl sample loop was used to inject the ethylbenzene/xylene mixture into to ensure a reproducible amount of analyte entered the system.

3.3.4.1 Separations with MFM-300(Al)

Based on the promising vapour phase results, the first MOF studied was MFM-300(Al). The initial conditions trialled were using a quaternary mixture of ethylbenzene, *m*-, *o*-, and *p*-xylene, with heptane as the eluent at a flow rate of 0.5 ml/min, with sample collection every minute. Results are shown in Figure 3.25.

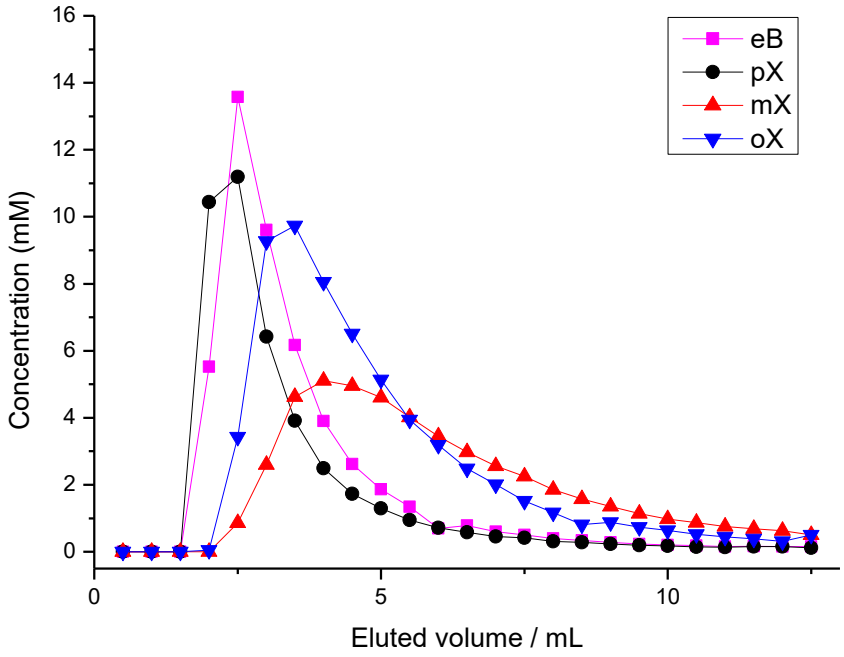


Figure 3.25 – Chromatogram of quaternary mixture of C_8 hydrocarbons in MFM-300(Al). Flow rate: 0.5 ml/min. Eluent: Heptane

A very minor degree of separation is observed, in the order *p*-xylene, ethylbenzene, *o*-xylene and then *m*-xylene, but there is a large amount of peak overlap and tailing present.

Using the same conditions, and after flushing the column with hexane for 60 minutes at 0.5 ml/min, hexane was then explored as an eluent. The results are shown in Figure 3.26.

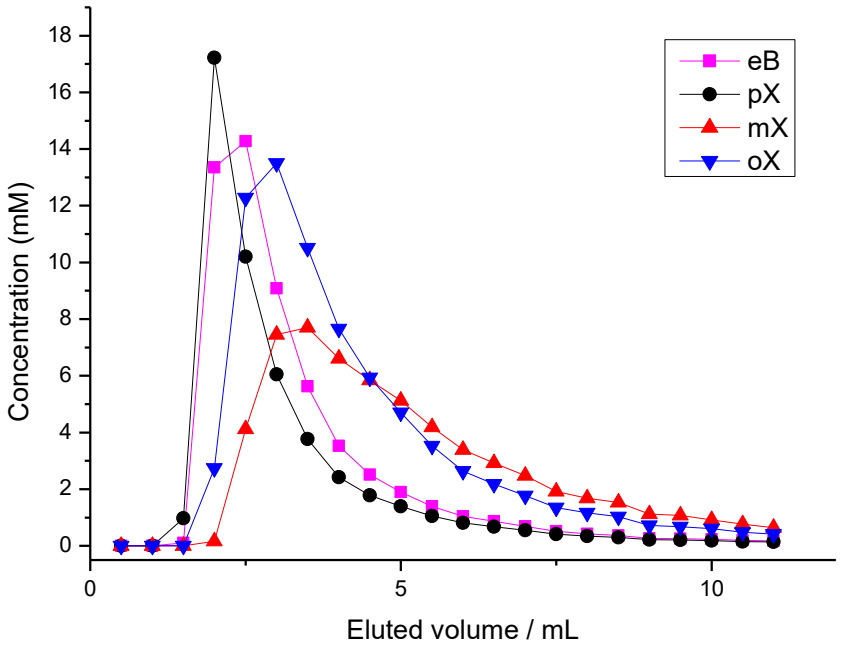


Figure 3.26 – Chromatogram of quaternary mixture of C_8 hydrocarbons in MFM-300(Al). Flow rate: 0.5 ml/min. Eluent: Hexane

These conditions, however, show no improvement over the separation with heptane.

The effect of conditioning of the column with DCM prior to performing the separation was then explored, as this has been shown to increase separation.[12] The column was conditioned for 80 minutes at a flow rate of 0.5 ml/min, followed by a separation experiment using a ternary mixture of *m*-, *o*-, and *p*-xylene and heptane as the eluent at a flow rate of 0.5 ml/min (Figure 3.27).

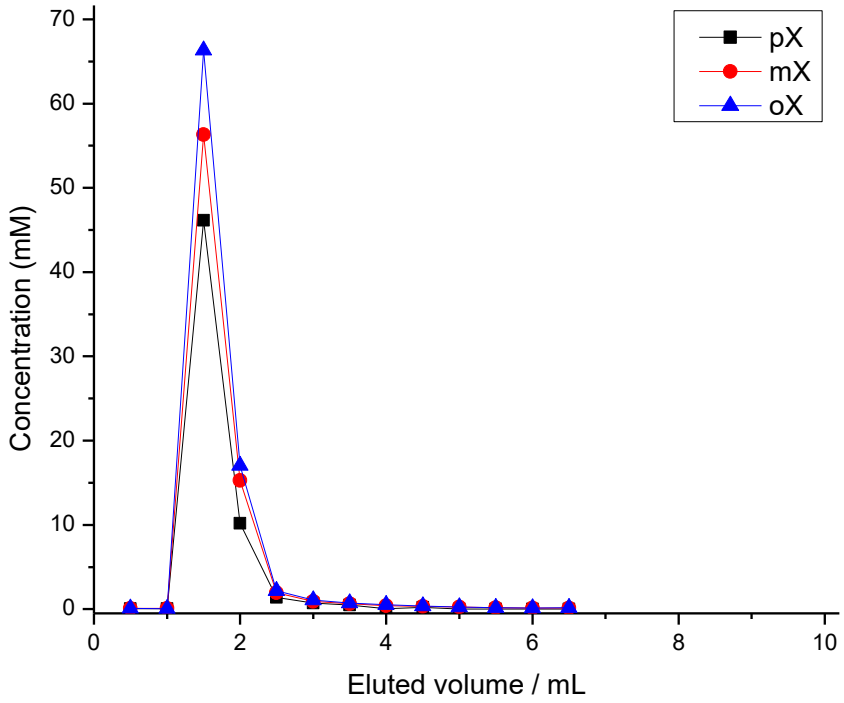


Figure 3.27 – Chromatogram of ternary mixture of C_8 hydrocarbons in MFM-300(Al) after DCM conditioning. Flow rate: 0.5 ml/min. Eluent: Heptane

In this case, however, conditioning had an adverse effect on the separation, with each of the 3 components eluting more quickly and at the same time. The peak shape, however, is much more symmetrical and narrower than in the heptane conditioned experiment.

Due to this improved peak shape with the presence of DCM, mixtures of heptane and DCM were considered as the eluent. Firstly a 95:5 (v/v) heptane:DCM mixture was used as the eluent, at a flow rate of 0.5 ml/min, using a ternary mixture of *m*-, *o*-, and *p*-xylene. The column was conditioned with heptane prior to the separation experiment. Results are shown in Figure 3.28.

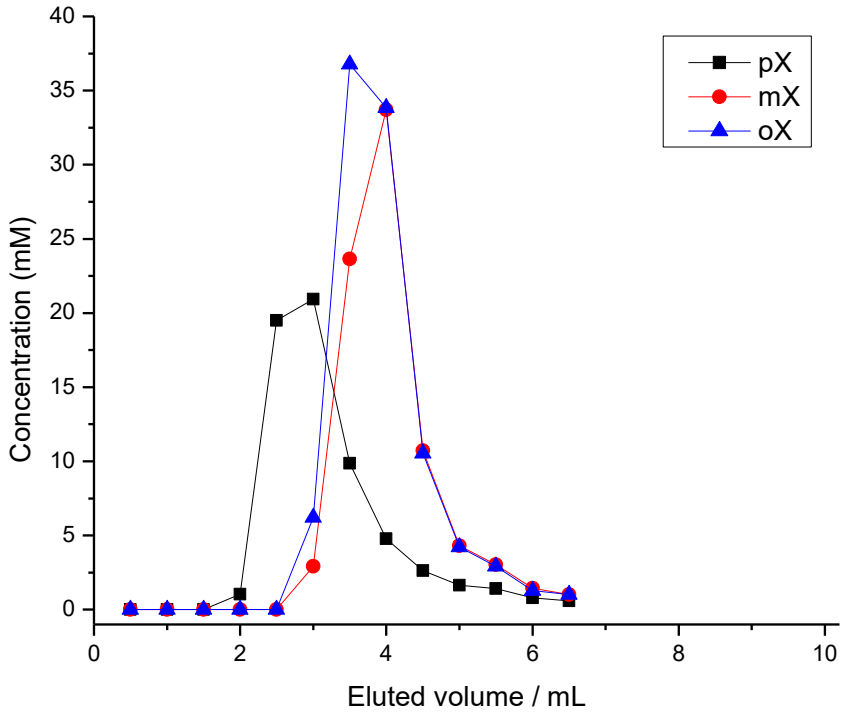


Figure 3.28 – Chromatogram of ternary mixture of C_8 hydrocarbons in MFM-300(Al). Flow rate: 0.5 ml/min. Eluent: 95:5 (v/v) heptane:DCM

There is a clear improvement on both the separation and the peak shape using these conditions compared to the pure heptane experiment, with *p*-xylene eluting slightly earlier than *m*- and *o*-xylene, which co-elute.

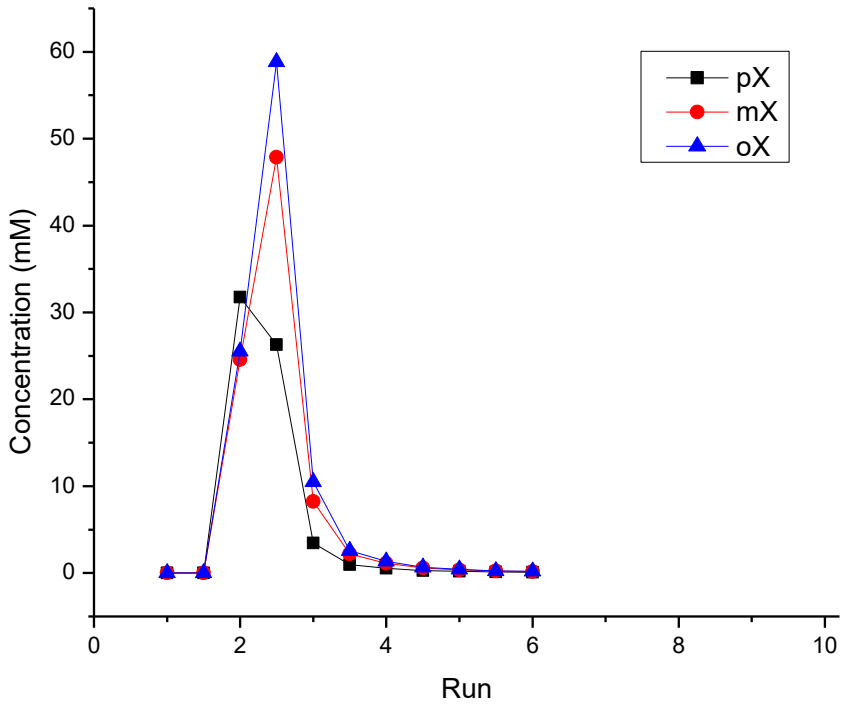


Figure 3.29 – Chromatogram of ternary mixture of C_8 hydrocarbons in MFM-300(Al) after conditioning with 95:5 (v/v) heptane:DCM. Flow rate: 0.5 ml/min. Eluent: 95:5 (v/v) heptane:DCM

The column was then conditioned for 60 minutes using the same 95:5 solvent mixture, and the separation experiment repeated using the same conditions (Figure 3.29). Again, the conditioning resulted in co-elution of all three xylenes.

Using a 9:1 (v/v) heptane:DCM mixture as the eluent, at a flow rate of 0.5 ml/min, on a heptane conditioned column worsens the separation of *p*-xylene from *m*- and *o*-xylene (Figure 3.30) when compared to the 95:5 solvent mixture, with separation only slightly better than the DCM conditioned experiment.

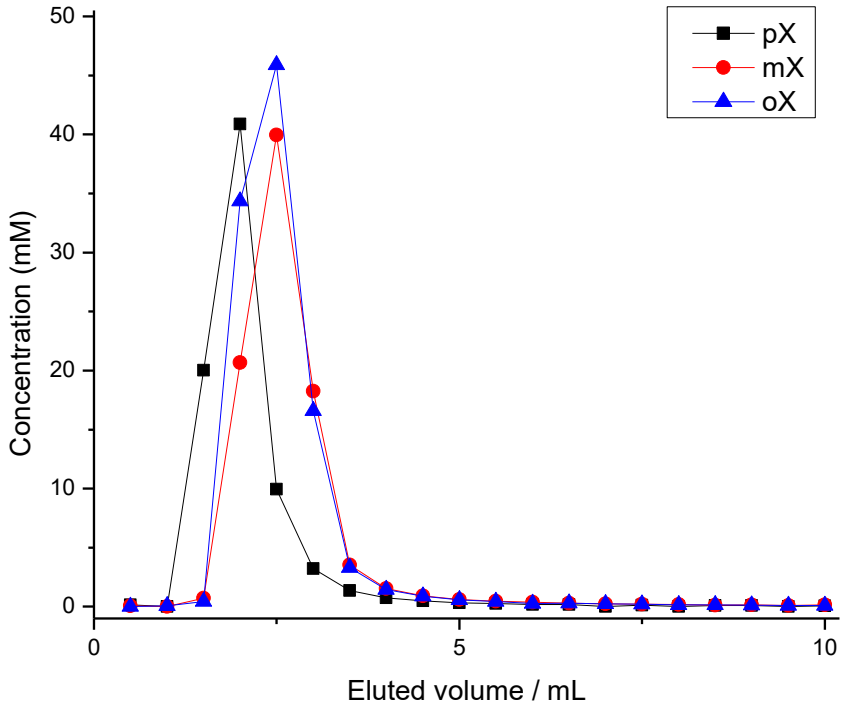


Figure 3.30 – Chromatogram of ternary mixture of C_8 hydrocarbons in MFM-300(Al). Flow rate: 0.5 ml/min. Eluent: 9:1 (v/v) heptane:DCM

The experiment was then repeated after conditioning the column with the 9:1 solvent mixture for 60 minutes. The resulting chromatogram is shown in Figure 3.31. Again, conditioning led to the co-elution of all three analytes.

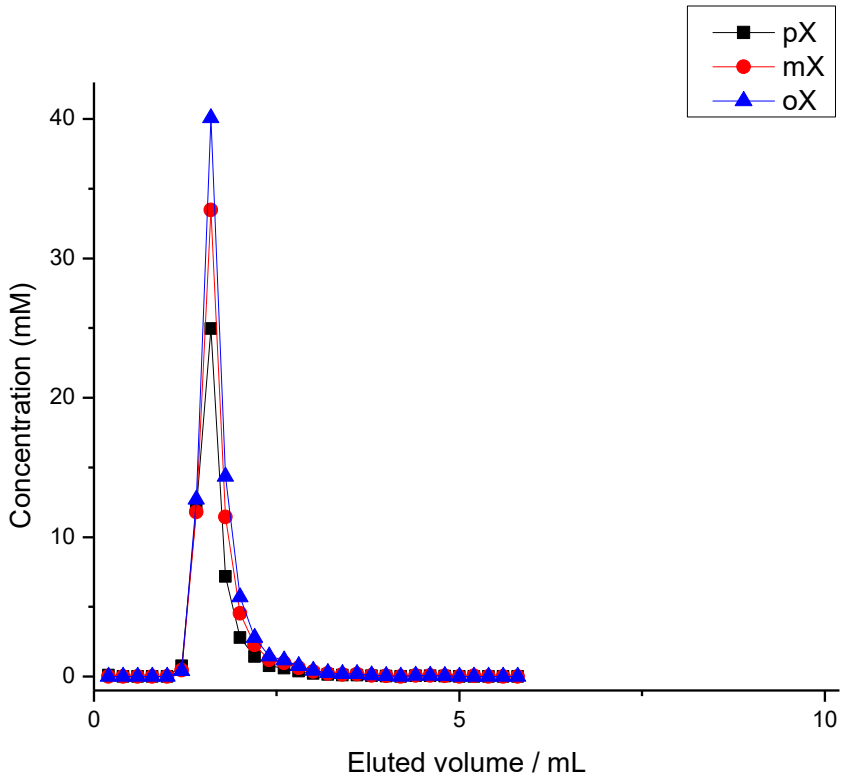


Figure 3.31– Chromatogram of ternary mixture of C_8 hydrocarbons in MFM-300(Al) after conditioning with 9:1 (v/v) heptane:DCM. Flow rate: 0.5 ml/min. Eluent: 9:1 (v/v) heptane:DCM

3.3.4.2 Separations with MFM-300(In)

After the separations in MFM-300(Al) proved unsuccessful, separations were attempted in MFM-300(In). Again, the initial conditions used heptane as the eluent at a flow rate of 0.5 ml/min, however in this case a quaternary mixture of ethylbenzene, *m*-, *o*- and *p*-xylene (1:1:1:1, v/v) was injected.

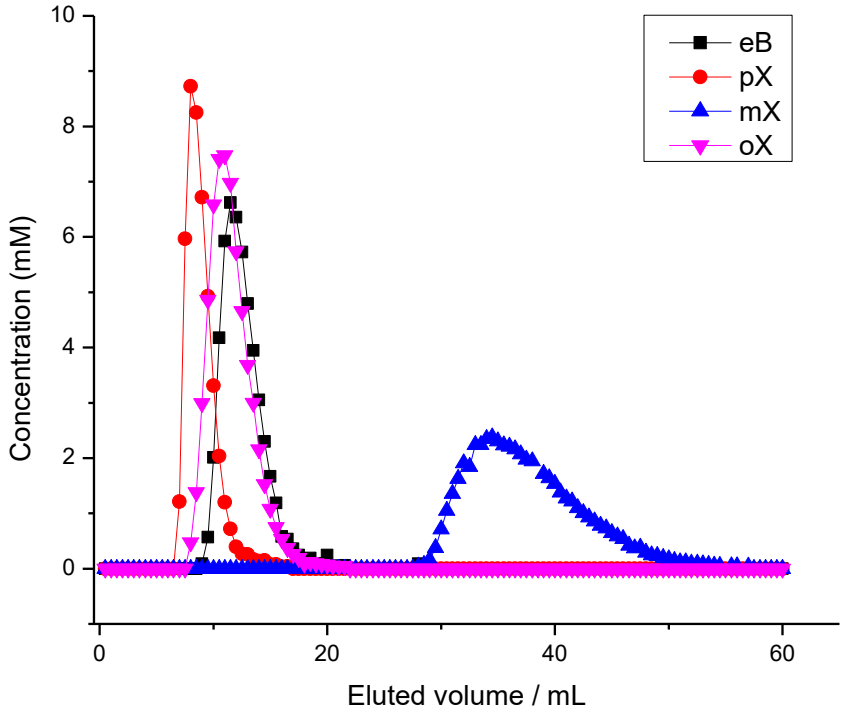


Figure 3.32– Chromatogram of quaternary mixture of C_8 hydrocarbons in MFM-300(In). Flow rate: 0.5 ml/min. Eluent: heptane.

Figure 3.32 confirms that separation does occur under these conditions. The first analyte to elute is *p*-xylene, followed by *o*-xylene, which elutes almost jointly with ethylbenzene, and finally *m*-xylene elutes last. Separation factors for this experiment (Table 3.4) confirm that the only significant separation occurs between *m*-xylene and the other compounds.

Table 3.4 – Separation factors calculated from MFM-300(In) chromatogram at 0.5 ml/min using heptane as the eluent.

	m-xylene	Ethylbenzene	*o*-xylene	*p*-xylene
m-xylene	-	3.0	3.1	4.2
ethylbenzene	-	-	1.1	1.4
o-xylene	-	-	-	1.3
p-xylene	-	-	-	-

There is a much greater degree of separation with these conditions in MFM-300(In) than there is in MFM-300(Al), which is the opposite of what was observed in the vapour phase experiments. This is likely due to the larger pore size of the In(III) MOF permitting diffusion of the hydrocarbon molecules, whereas in the case of the Al(III) analogue, there isn't sufficient time for the molecules to orientate into a suitable alignment to enter the pore.

To improve the separation, the experiment was repeated using hexane as the eluent. The resulting chromatogram is shown in Figure 3.33 and the corresponding separation factors shown in Table 3.5.

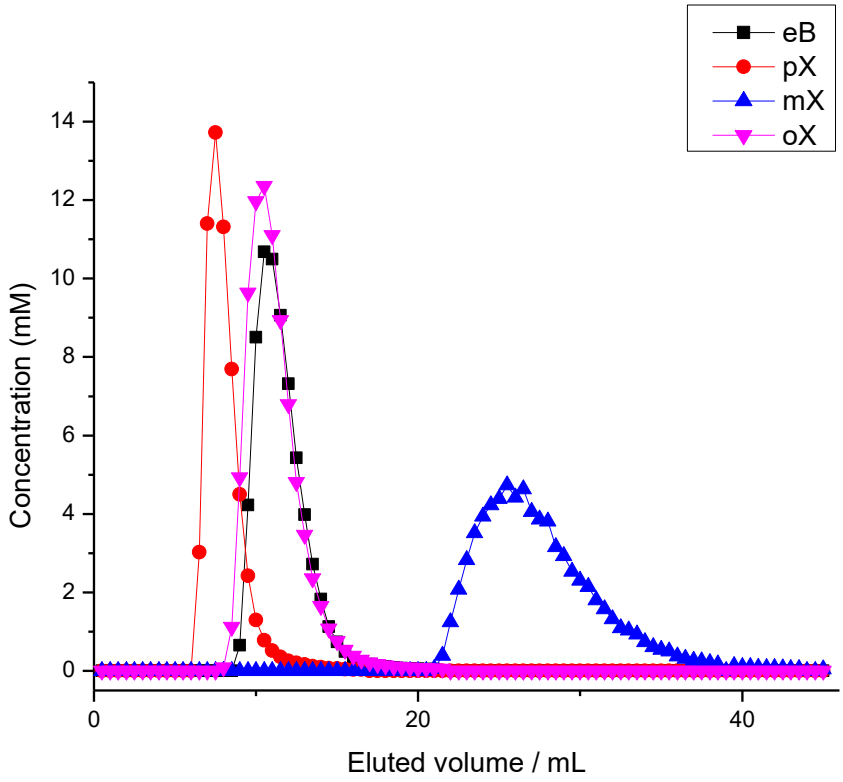


Figure 3.33– Chromatogram of quaternary mixture of C_8 hydrocarbons in MFM-300(In). Flow rate: 0.5 ml/min. Eluent: hexane.

Similarly to the results using heptane, the first compound to elute is *p*-xylene. This is followed by the co-elution of *o*-xylene and ethylbenzene, and then finally *m*-xylene elutes. As a result of the slightly longer retention time of *o*-xylene, the *o*-xylene/*p*-xylene separation factor is slightly larger than in the heptane experiment (1.4 compared to 1.3). Aside from this slight improvement, the separation is generally worse when using hexane as the eluent, however there is still baseline separation of *m*-xylene from ethylbenzene, *o*-xylene and *p*-xylene.

Table 3.5 – Separation factors calculated from MFM-300(In) chromatogram at 0.5 ml/min using hexane as the eluent.

	m-xylene	ethylbenzene	*o*-xylene	*p*-xylene
m-xylene	-	2.4	2.4	3.4
ethylbenzene	-	-	1.0	1.4
o-xylene	-	-	-	1.4
p-xylene	-	-	-	-

The experiment was then repeated using pentane as the eluent. The results are shown in Figure 3.34 and the corresponding separation factors shown in Table 3.6.

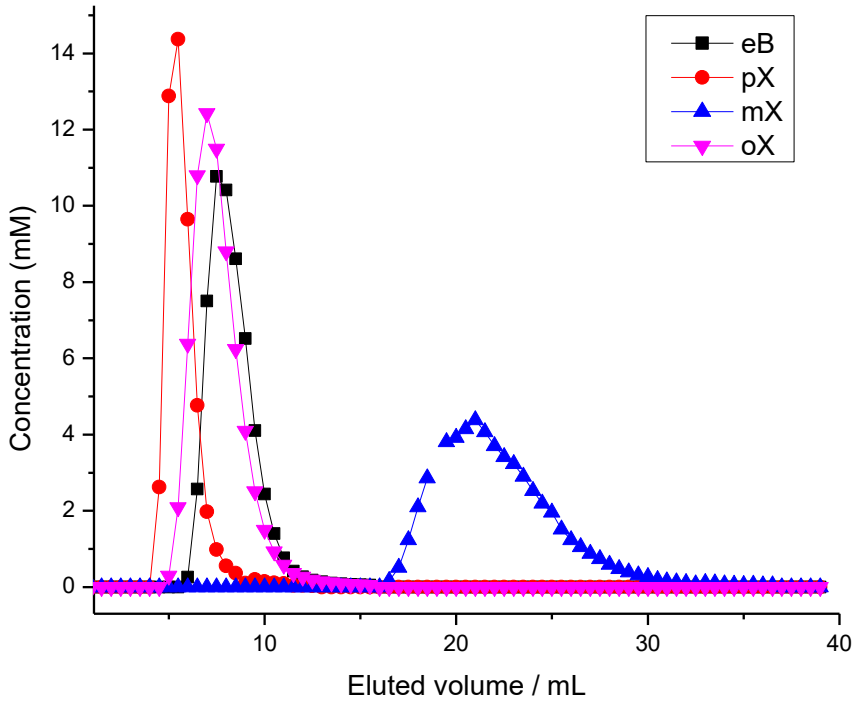


Figure 3.34– Chromatogram of quaternary mixture of C_8 hydrocarbons in MFM-300(In). Flow rate: 0.5 ml/min. Eluent: pentane.

Table 3.6 – Separation factors calculated from MFM-300(In) chromatogram at 0.5 ml/min using pentane as the eluent.

	m-xylene	ethylbenzene	*o*-xylene	*p*-xylene
m-xylene	-	2.7	3.0	4.0
ethylbenzene	-	-	1.1	1.5
o-xylene	-	-	-	1.3
p-xylene	-	-	-	-

Again, the order in which the compounds elute starts with *p*-xylene, followed by *o*-xylene, which is closely followed by ethylbenzene, and finally *m*-xylene elutes. The separation factors indicate that aside from *o*-xylene/*p*-xylene, the separation of each compound is better than with hexane, and only marginally worse than with heptane.

3.3.4.4 Separations with MFM-300(V)

Using similar conditions to those proven successful in MFM-300(In), separations with MFM-300(V) were then investigated. The first condition tried was using heptane as the eluent. Due to the higher back-pressures exhibited when using this column, however, the highest possible flow rate when using heptane was 0.32 ml/min. The results are shown in Figure 3.35 and separation factors shown in Table 3.7. It should be noted that due to a minimum sample volume requirement of the GC, the fractions were diluted with heptane to bring the overall volume of each fraction to 0.5 ml.

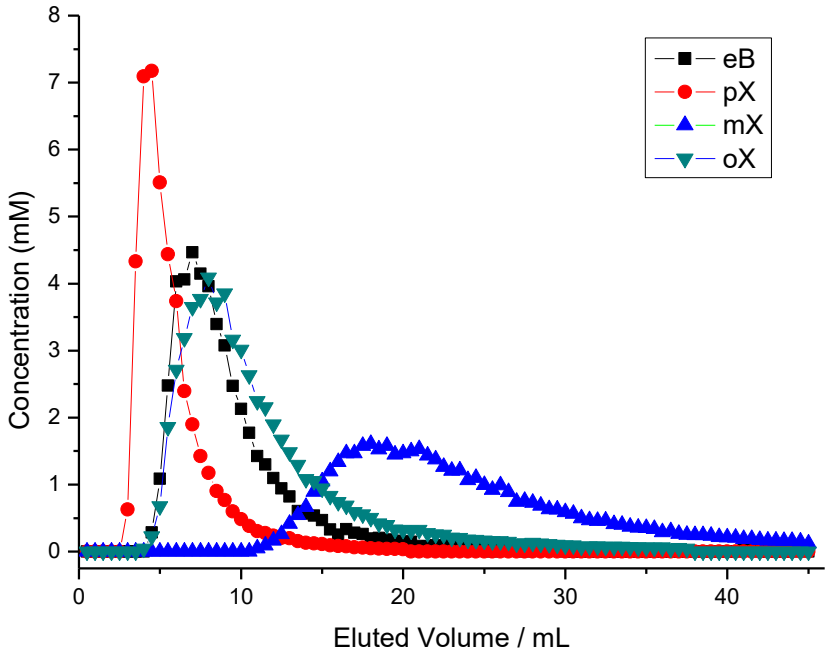


Figure 3.35– Chromatogram of quaternary mixture of C_8 hydrocarbons in MFM-300(V). Flow rate: 0.32 ml/min. Eluent: heptane.

Table 3.7 – Separation factors calculated from MFM-300(V) chromatogram at 0.32 ml/min using heptane as the eluent.

	m-xylene	*o*-xylene	ethylbenzene	*p*-xylene
m-xylene	-	2.2	2.5	3.9
o-xylene	-	-	1.2	1.8
ethylbenzene	-	-	-	1.6
p-xylene	-	-	-	-

Compared to the equivalent MFM-300(In) experiment, the order of elution of the four compounds appears to change. Firstly, *p*-xylene elutes, but this is followed by ethylbenzene which elutes closely with *o*-xylene, and finally *m*-xylene elutes. Based on the separation factors alone, the separation seems fairly good in comparison the MFM-300(In), however the broadness and tailing of the peaks means that the separation of *m*-xylene over the other three components is actually considerably worse.

Hexane was then used as the eluent, at a flow rate of 0.32 ml/min, after flushing the column with hexane for 2 hours. The results are shown in Figure 3.36. Again, the fractions were diluted to increase the volume to 0.5 ml for GC analysis.

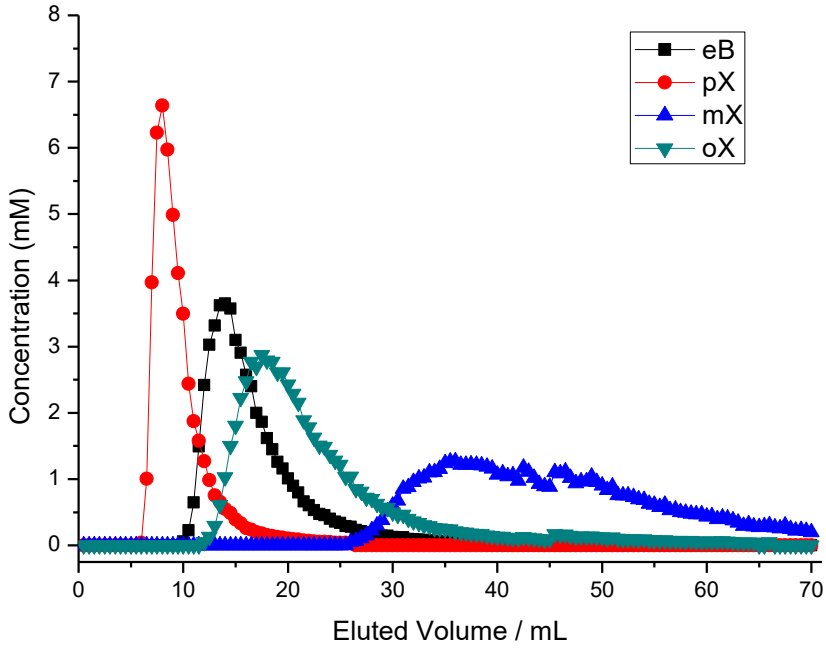


Figure 3.36– Chromatogram of quaternary mixture of C_8 hydrocarbons in MFM-300(V). Flow rate: 0.32 ml/min. Eluent: hexane.

The order of elution remains the same as with heptane, with *p*-xylene eluting first, followed by ethylbenzene, followed by *o*-xylene and then finally *m*-xylene. The separation factors (Table 3.8) show slight improvements over the heptane experiment for all but *m*-xylene/*o*-xylene, due to the comparatively longer retention time of *o*-xylene in this instance. Once again though, the peaks exhibit trailing which leads to a large amount of peak overlap. The only two compounds to show baseline separation are *m*-xylene/*p*-xylene.

Table 3.8 – Separation factors calculated from MFM-300(V) chromatogram at 0.32 ml/min using hexane as the eluent.

	m-xylene	*o*-xylene	ethylbenzene	*p*-xylene
m-xylene	-	2.0	2.6	4.5
o-xylene	-	-	1.3	2.1
ethylbenzene	-	-	-	1.7
p-xylene	-	-	-	-

Finally pentane was used as the eluent, at 0.32 ml/min, after flushing the column with pentane for 2 hours. Results are shown in Figure 3.37.

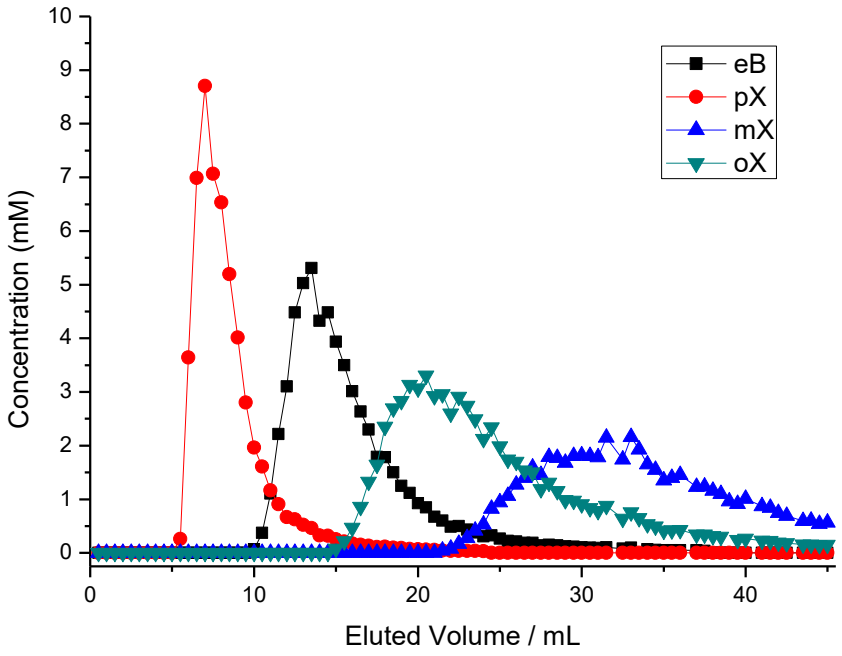


Figure 3.37– Chromatogram of quaternary mixture of C_8 hydrocarbons in MFM-300(V). Flow rate: 0.32 ml/min. Eluent: pentane.

Again the order of elution remains as *p*-xylene, ethylbenzene, *o*-xylene then *m*-xylene. The separation factors (Table 3.9) show equal separation of *m*-xylene/*o*-xylene and ethylbenzene/*o*-xylene (1.5), which also corresponds to the highest degree of ethylbenzene/*o*-xylene separation observed in these experiments. The separation of *p*-xylene from *o*-xylene and ethylbenzene is also the best observed in these experiments, although the tailing of the peaks results in a considerable amount of peak overlap.

Table 3.9 – Separation factors calculated from MFM-300(V) chromatogram at 0.32 ml/min using pentane as the eluent.

	m-xylene	*o*-xylene	ethylbenzene	*p*-xylene
m-xylene	-	1.5	2.2	4.3
o-xylene	-	-	1.5	2.9
ethylbenzene	-	-	-	1.9
p-xylene	-	-	-	-

3.3.4.5 Binary Breakthrough Experiments

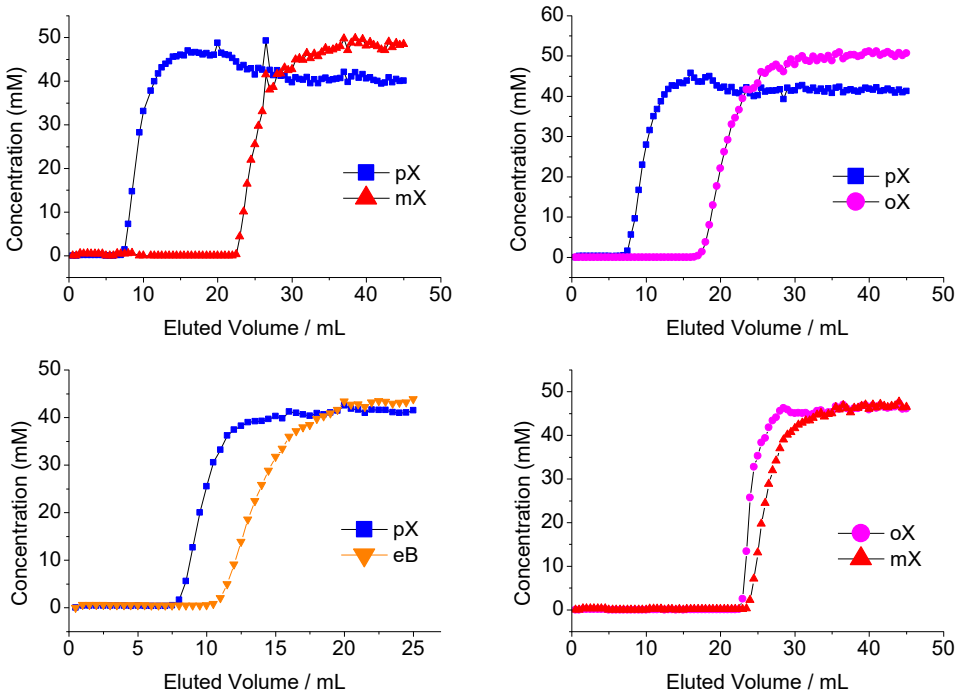


Figure 3.38 – binary breakthrough experiments using 40 mM binary mixtures.

After the promising results from the MFM-300(V) experiments with pentane, binary breakthrough experiments were performed with 40 mM 1:1 mixtures of *p*-xylene/*m*-xylene, *p*-xylene/*o*-xylene, *p*-xylene/ethylbenzene, and *m*-xylene/*o*-xylene in pentane (Figure 3.38). The separation of *m*-xylene from *p*-xylene is excellent, with 14 ml of elution *p*-xylene before the elution of *m*-xylene. Unsurprisingly, the separations follow the same trend as shown in the HPLC experiments, with *p*-xylene/*o*-xylene separation being slightly less than *p*-xylene/*m*-xylene, ethylbenzene/*p*-xylene slightly less than *p*-xylene/*o*-xylene, and *m*-xylene/*o*-xylene showing very little separation at all.

3.4 Conclusions

To summarise, investigations into the liquid phase separation of *m*-xylene, *o*-xylene, *p*-xylene and ethylbenzene in MFM-300(M) (M=Al, V, In) have been conducted. MFM-300(V) shows the most promise at separating all 4 compounds when using pentane as an eluent, however the broad peak shapes of the chromatogram affect the resolution. MFM-300(In) shows baseline separation of *m*-xylene from the other three compounds, however there is a large degree of coelution *o*-xylene and ethylbenzene. MFM-300(Al) shows virtually no separation of the four compounds, which is in contrast to the vapour phase adsorption experiments, where it showed a much higher uptake of *p*-xylene than *o*-xylene and *m*-xylene, and almost no uptake of ethylbenzene. High resolution PXRD was performed on C_8 hydrocarbon loaded MFM-300(M), confirming that the guest molecules interact with the phenyl ring of the framework. On *p*-xylene loading, MFM-300(In) undergoes a tetragonal $I4_122$ to orthorhombic $I2_12_12_1$ phase transition. This transition was further investigated using high pressure PXRD, where the same transition was observed at 0.584 GPa.

3.5 Experimental

3.5.1 High Resolution PXRD of Hydrocarbon-loaded MFM-300(M)

Samples of acetone-exchanged MFM-300(Al), MFM-300(V), and MFM-300(In) were activated at 120 °C under vacuum (10^{-3} bar) for 48 hours, each MOF divided into four portions, and 2 ml of either *m*-xylene, *o*-xylene, *p*-xylene or ethylbenzene added to each portion. The vials were then sealed for a period of 4 weeks. The samples were ground and loaded into 0.7 mm borosilicate capillaries. High resolution PXRD data were collected using monochromatic X-rays (λ = 0.825633,

0.825706, 0.825868 or 0.826162 Å) and MAC detectors, with the sample spinning to ensure better powder averaging. The backgrounds of the profiles were fitted using a Chebyshev polynomial with 13 coefficients, and the Stephens anisotropic peak function used to account for the slight anisotropic line broadening observed.

3.5.2 High Pressure PXRD Collection of MFM-300(In)

A sample of acetone-exchanged MFM-300(In) was activated for 5 days at 150 °C under vacuum (10^{-2} bar), ground, and then loaded in an inert atmosphere into a membrane-driven DAC, with quartz included to act as an internal pressure marker and Fluorinert™ FC-70 used as the PTM. *In situ* high pressure PXRD data were collected using monochromatic X-rays (λ = 0.4246 Å) and a MAR-345 image plate detector. The cell was pressurised from 0 – 3.23 GPa, followed by decompression to ambient pressure. The raw image data was processed using Fit-2D and Pawley refinements of the integrated data were performed in TOPAS Academic 5. The peak profile of the low pressure tetragonal phase was modelled using the Thompson-Cox-Hastings peak function, whereas the more asymmetric peaks present in the high pressure orthorhombic phase were modelled using a split pseudo-Voight function.

3.5.3 Vapour Adsorption Experiments

Isotherms were recorded at 318.15 K using a temperature controlled water bath on a Hiden IGA under ultrahigh vacuum. Both *m*-xylene (99%, Extra Dry, AcroSeal™) and *o*-xylene (99%, Extra Dry, AcroSeal™) were purchased from ACROS Organics. Ethylbenzene (anhydrous, 99.8%) and *p*-xylene (anhydrous, ≥99%) were purchased from Sigma Aldrich. The solvents were degassed in the vapour-loading chamber of the IGA. In each case around 80 mg of MFM-300(M) (M=Al, V, In) was loaded into the IGA and activated under ultrahigh vacuum at 423.15 K for 24 h. Between runs the samples were reactivated at 423.15 K for 24 h.

3.5.4 Liquid Phase Experiments

Liquid phase experiments were performed using a Gilson 307 HPLC pump equipped with a 10 ml pump head. The columns used were Supelco column blanks (ID × OD × L 4.6 mm × 1/4 in. × 15 cm), purchased from Sigma Aldrich. Parts were connected by Swagelok 1/16 in. stainless steel tubing. Quantitative analysis of fractions was performed on a Shimadzu GC-2014 gas chromatograph fitted with an Agilent J&W HP-INNOWax GC Column (ID x L x F 20 m x 0.18 mm x 0.18 µm).

3.5.4.1 Column Packing

Acetone-exchanged MFM-300(M) (M=Al, V, In) were each ground thoroughly and loaded as a slurry in heptane into a blank column which was then connected to the pump. The pressure limit on the pump was set to 220 bar and heptane flowed through the column a set flow rate of 4 ml/min for 15 minutes, maintaining a pressure of 220 bar throughout. More of the MOF slurry was then added to the column and the process repeated until the column was fully packed, at which point the column was flushed with heptane at 220 bar for 60 minutes.

3.5.4.2 HPLC Separations

A quaternary mixture of ethylbenzene and *m*-, *o*- and *p*-xylene (1:1:1:1, v/v) was injected into the injector port of a Rheodyne Model 7125 Injector fitted with a 5 µl sample loop. The eluent fed through the pump into the Rheodyne injector and then into the column. The analyte mixture was injected when the system was at a stable operating pressure.

3.5.4.3 Breakthrough Experiments

Breakthrough experiments were performed using equimolar binary mixtures of *m*-xylene/*o*-xylene, *m*-xylene/*p*-xylene, *o*-xylene/*p*-xylene, and *p*-xylene/ethylbenzene

in pentane at concentrations of 40 mM. The pump fed from this mixture at a set flow rate for the duration of the experiment.

3.6 References

1. V. Finsy, H. Verelst, L. Alaerts, D. De Vos, P. A. Jacobs, G. V. Baron and J. F. M. Denayer, *J. Am. Chem. Soc.*, 2008, **130**, 7110-7118.

2. M. P. M. Nicolau, P. S. Bárcia, J. M. Gallegos, J. A. C. Silva, A. r. E. Rodrigues and B. Chen, *J. Phys. Chem. C*, 2009, **113**, 13173-13179.

3. R. El Osta, A. Carlin-Sinclair, N. Guillou, R. I. Walton, F. Vermoortele, M. Maes, D. de Vos, and F. Millange, *Chem. Mater*., 2012, **24**, 2781–2791.

4. J. M. Holcroft, K. J. Hartlieb, P. Z. Moghadam, J. G. Bell, G. Barin, D. P. Ferris, E. D. Bloch, M. M. Algaradah, M. S. Nassar, Y. Y. Botros, K. M. Thomas, J. R. Long, R. Q. Snurr, and J. F. Stoddart, *J. Am. Chem. Soc*., 2015, **137**, 5706–5719.

5. S. Yang, J. Sun, A. J. Ramirez-Cuesta, S. K. Callear, W. I. F. David, D. P. Anderson, R. Newby, A. J. Blake, J. E. Parker, C. C. Tang and M. Schröder, *Nat. Chem*., 2012, **4**, 887-894.

6. M. Savage, I. da Silva, M. Johnson, J. H. Carter, R. Newby, M. Suyetin, E. Besley, P. Manuel, S. Rudić, A. N. Fitch, C. Murray, W. I. F. David, S. Yang and M. Schröder, *J. Am. Chem. Soc.*, 2016, **138**, 9119–9127.

7. K. Yang, Q. Sun, F. Xue, D. Lin, *J. Hazard Mater*., 2011, **195**, 124-131.

8. C. D. Baertsch, H. H. Funke, J.L. Falconer, and R. D. Noble, *J. Phys. Chem*., 1996, **100**, 7676–7679.

9. H. Kanai, V. Inouye, L. Yazawa , R. Goo, H. Wakatsuki, *J. Chromatogr. Sci.*, 2005, **43**, 57-62.

10. A. U. Ortiz, A. Boutin and F-X.Coudert, *Chem. Commun*., 2014, **50**, 5867-5870

11. O. Talu, C. Jie Guo, D. T. Hayhurst, *J. Phys. Chem*., 1989, **93**, 7294–7298.

12. A.Ahmed, M.Forster, R. Clowes, D. Bradshaw, P. Myers and H.Zhang, *J. Mater. Chem. A*, 2013, **1**, 3276-3286.

Chapter 4

A Stable Zirconium MOF for CO_2 Separation

4.1 Introduction

The general appeal of Zr(IV) MOFs is their excellent hydrothermal and thermal stability.[1,2] This opens up avenues of research not possible with other, less stable MOFs, such as copper and zinc, for example water adsorption.

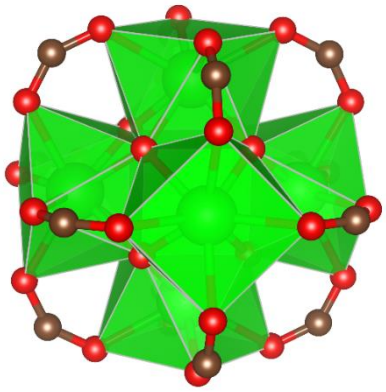


Figure 4.1 – $Zr_6O_4(OH)_4L_{12}$ cluster present in UiO-66. Figure taken from reference 2.

The first zirconium MOFs were demonstrated in 2008 by Lillerud *et al.*[2] with the publication of the series UiO-66 – UiO-68. The series comprises a $Zr_6O_4(OH)_4L_{12}$ cluster (Figure 4.1), with linear dicarboxylate linkers 1,4-benzene-dicarboxylate, 4,4'-biphenyl-dicarboxylate and 4,4''-terphenyl-dicarboxylate and exhibits excellent hydrothermal, mechanical stability, and gas adsorption properties. Responsible for this observed high stability is the highly connected octahedral Zr_6 cluster, in which alternate triangular faces are capped with μ_3-O and μ_3-OH. The stability of this series has led to considerable research into this series, particularly into ligand functionalisation[3,4] and post-synthetic modification.[5]

Work by Yaghi *et al.*[6] exploited the water stability of the Zr_6 cluster to investigate the water adsorption properties of several Zr(IV) MOFs. The frameworks each

showed a retention of crystallinity after water adsorption, and almost no loss of uptake was observed over five cycles.

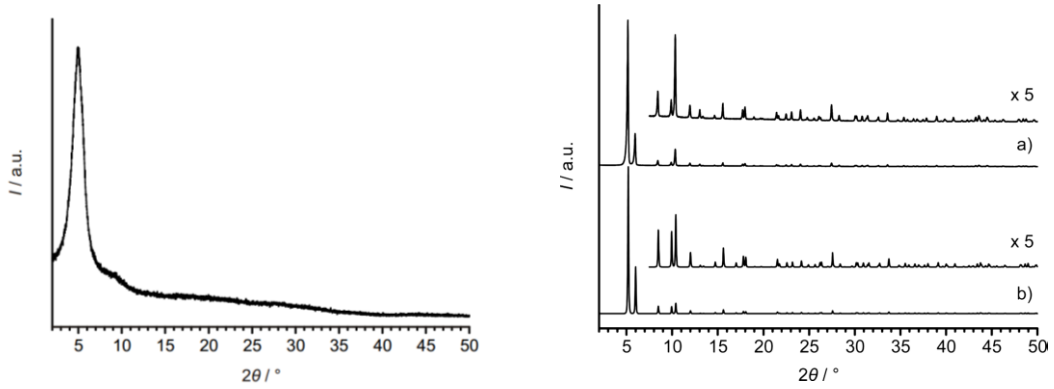


Figure 4.2 – (left) resulting powder diffractogram from synthesis without modulator; (right) resulting powder diffractogram from synthesis using modulator. Figure taken from reference 7.

A common approach in Zr-MOF chemistry is the use of a monocarboxylic acid modulator during the MOF synthesis. The modulator is often used in large excess, and acts as a competitive binder to the zirconium cluster, greatly reducing the rate of nucleation of the MOF, thereby significantly increasing the crystallinity of the final product. Behrens *et al.*[7] investigated this effect and successfully showed how the use of benzoic acid greatly increased the product's crystallinity. Their results are shown in Figure 4.2

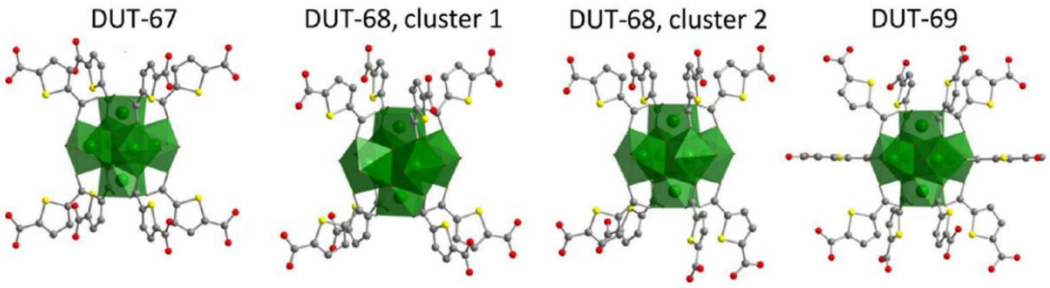


Figure 4.3 – Zr(IV) clusters present in DUT-67, DUT-68 and DUT-69. Figure taken from reference 8.

In 2013, Kaskel *et al.*[8] demonstrated a series of Zr-MOFs using 2,5-thiophenedicarboxylic acid as a linker. They found that due to the bent linker, a series of polymorphic MOFs could be made (DUT-67, DUT-68 and DUT-69) by varying solvents and the amount of acetic acid used as modulator, suggesting that modulators may have another role in the formation of zirconium MOFs, in addition to merely increasing crystallinity. The different zirconium clusters from this polymorphic series can be seen in Figure 4.3. They are very similar to the $Zr_6O_4(OH)_4L_{12}$ clusters present in the UiO-66 series, differing only by the number of linkers coordinated.

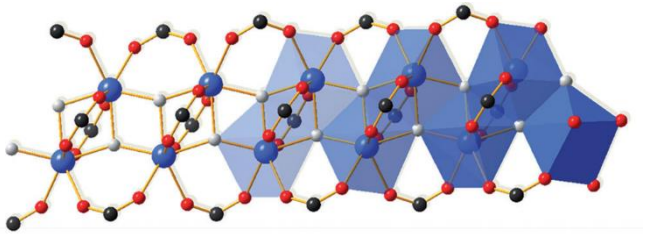


Figure 4.4 – Zirconium oxide chains found in the MIL-140 series. Figure taken from reference 9.

Work by Serre *et al.*[9] has shown a completely different type of zirconium cluster to those in the previously discussed cases. The MIL-140 series consists of zirconium oxide chains, shown in Figure 4.4, bridged by dicarboxylic acids. The group compared the stability of this series to their respective polymorphs in the UiO-66 – UiO-68 series and found that, especially when comparing the polymorphs of the longer linkers, the MIL-140 series was much more stable.

4.2 Aims of this Work

The aims of this chapter were to synthesises a highly stable Zr(IV) MOF for use in CCS, and to use synchrotron PXRD to gain an understanding of the MOFs behaviour in response to CO_2.

4.3 Results and Discussion

4.3.1 Synthesis

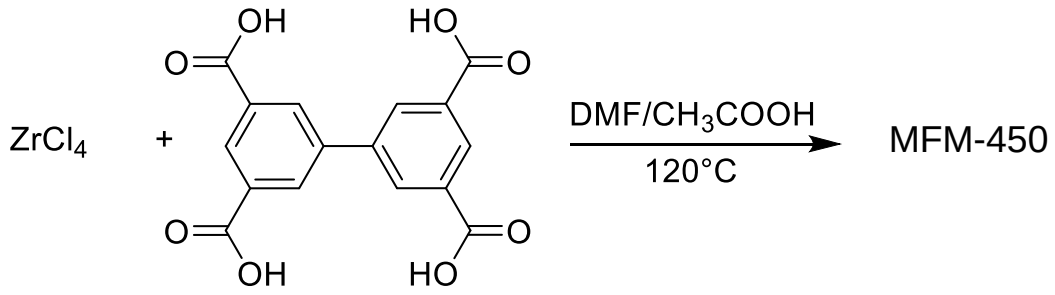


Figure 4.5 – MFM-450 reaction scheme

MFM-450 was synthesised via solvothermal methods using a roughly 2:1 ratio of ZrCl4:BPTC in a 1:1 mixture of DMF and acetic acid at 120°C, yielding a phase pure white microcrystalline powder (Figure 4.5). PXRD (Figure 4.6) reveals that the material crystallises in the cubic space group *Im*-3 with unit cell dimensions of *a* = 24.403(2) Å.

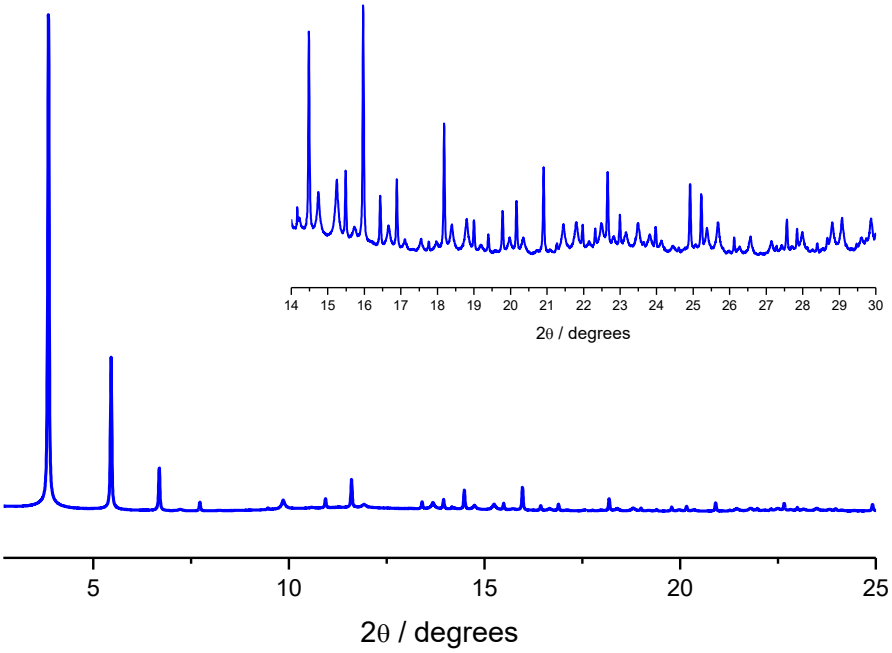


Figure 4.6 – synchrotron powder diffractogram of MFM-450; (inset) high angle region showing excellent crystallinity

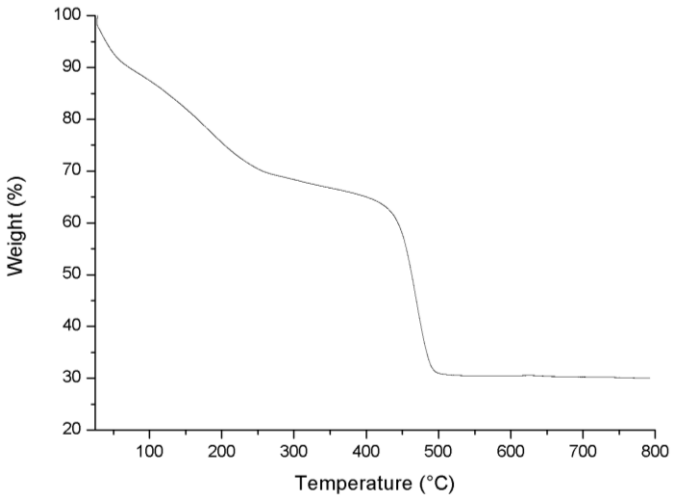


Figure 4.7 – TGA of MFM-450

TGA of the as-synthesised sample of MFM-450 in air (Figure 4.7) shows solvent loss below 200°C, with the material then stable up to 420°C, at which point the framework decomposes.

4.3.2 Structure of MFM-450

The structure was solved by Prof. Junliang Sun using Materials Studio. This structure solution was then used as a model for the subsequent refinements presented here.

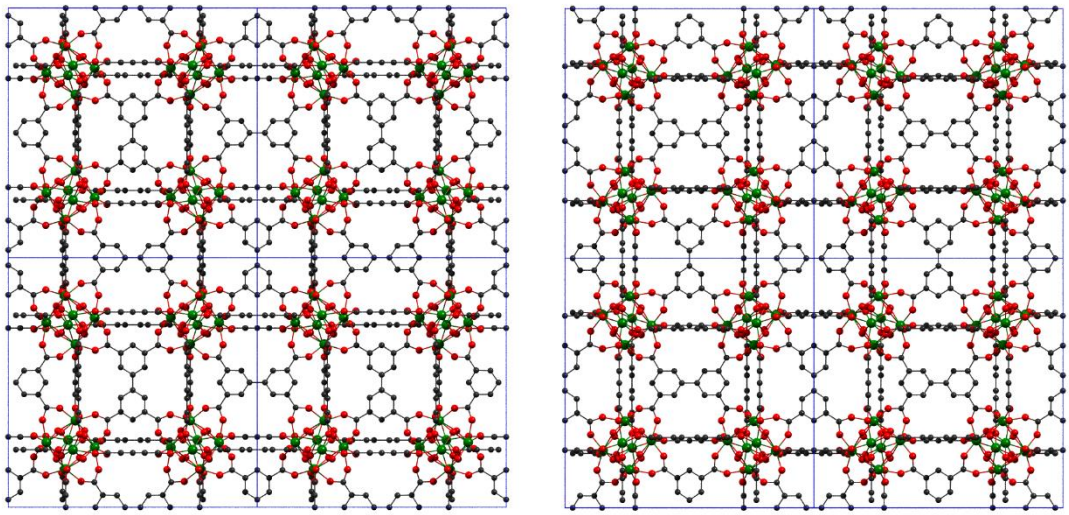


Figure 4.8 – (left) view down *a* axis of 2x2 supercell of MFM-450 showing extended framework; (right) view down *c* axis of 2x2 supercell of MFM-450 showing extended framework.

MFM-450 crystallises in the cubic space group *Im*-3, comprising an extended framework (Figure 4.8) formed of two distinct cages with $ZrO_4(OH)_4$ clusters at the vertices and BPTC linkers lying flat on each face (Figure 4.9). The positions of the H atoms on the cluster cannot be determined by PXRD, however evidence from the *in situ* CO_2 experiment discussed later in this chapter suggests that the O atoms pointing into cage B are protonated. The arrangement of linkers on the faces of each

cage dictates the size and shape of the cage, with cage A being cubic, and cage B cuboidal.

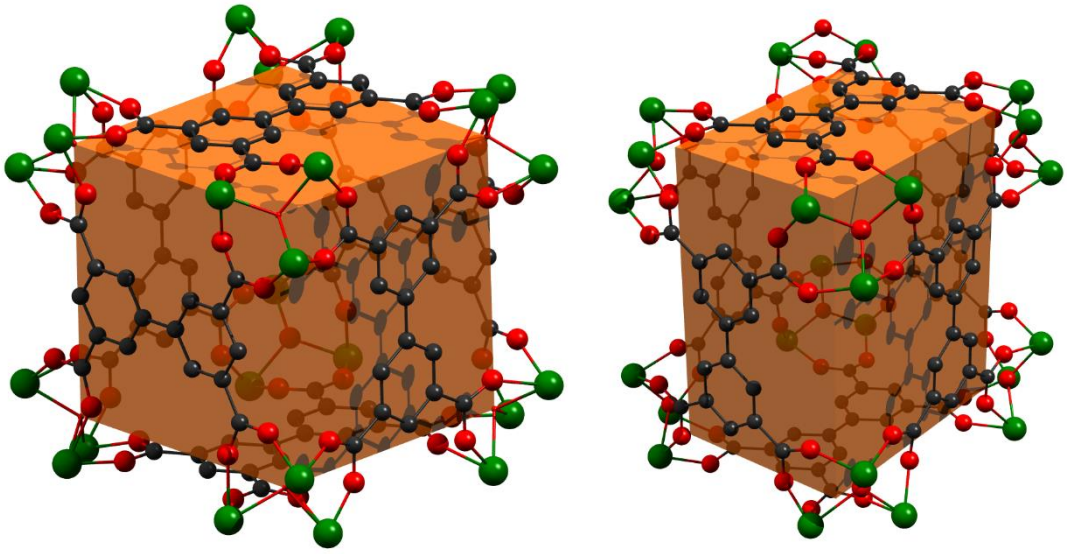


Figure 4.9 – (left) cubic cage A, with alternate arrangement of linkers on adjacent faces; (right) cuboidal cage B with two of four adjacent faces sharing similar linker orientation.

In cage A, due to adjacent faces of the cube each having alternate linker orientations, there is only one type of narrow window along the edge of the cage. In cage B, however, when considering one face, two of the four adjacent faces have the linker orientated in the same direction as this face, resulting in three types of window: a larger window in the case of side-on – side-on linkers, a smaller window of similar size to that found on cage A, resulting from side-on – end-on orientations, and finally the smallest window which is a result of end-on – end-on orientations.

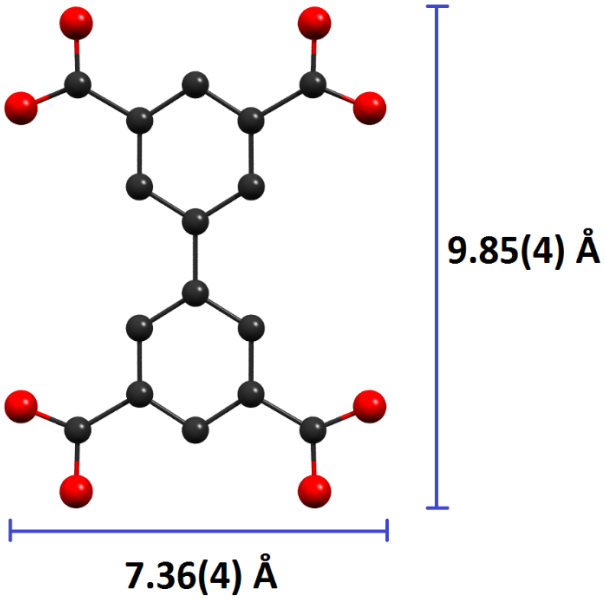


Figure 4.10 – dimensions of BPTC as measured from MFM-450 structure.

As the linker occupies a square face of a cube, but dimensions of the linker are not square in shape (Figure 4.10), the $ZrO_4(OH)_4$ octahedra distort heavily to accommodate them. When comparing the cluster to that of the $ZrO_4(OH)_4$ cluster found in UiO-66,[1] another MOF with a $ZrO_4(OH)_4L_{12}$ cluster (Figure 4.11), this distortion is apparent.

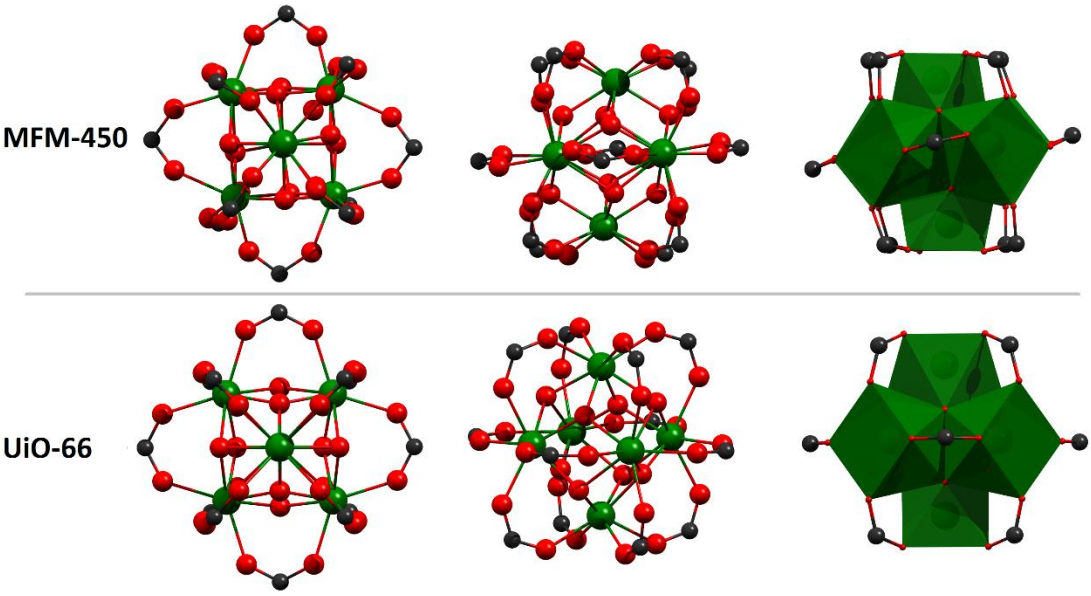


Figure 4.11 – (top) different views of Zr(IV) cluster in MFM-450; (bottom) different views of Zr(IV) cluster in UiO-66.

On inspection of the powder diffractogram of MFM-450 (Figure 4.12), it is clear that two distinct peak shapes are present. These broad peaks lie on reflections which have an odd number as an *h*, *k*, or *l* value, which are also coincident with the planes which intersect the Zr(IV) atoms. Due to the distortion of the $ZrO_4(OH)_4$ cluster, however, some clusters are positioned slightly out of the *hkl* plane (Figure 4.13), which possibly contributes to the peak broadening.

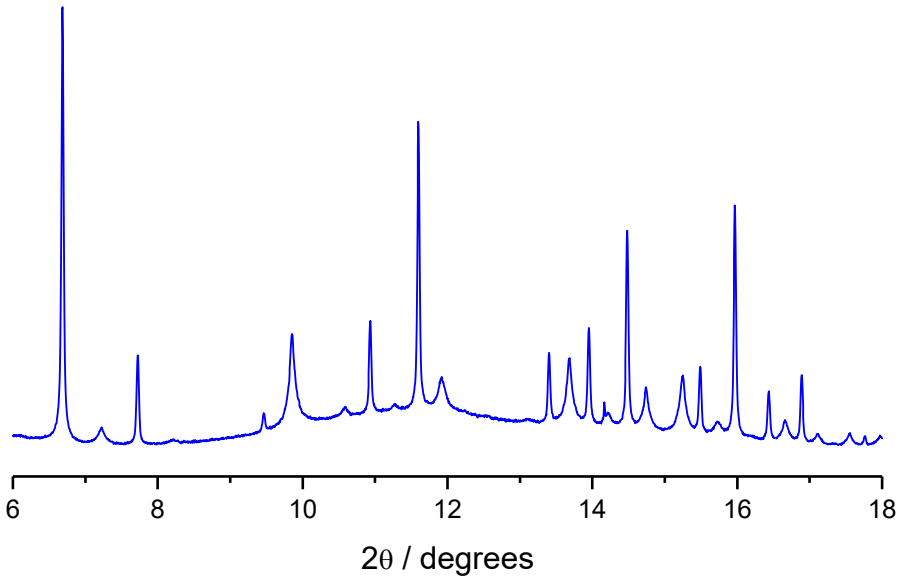


Figure 4.12 – zoomed in region of powder diffractogram of MFM-450, showing two distinct peak shapes.

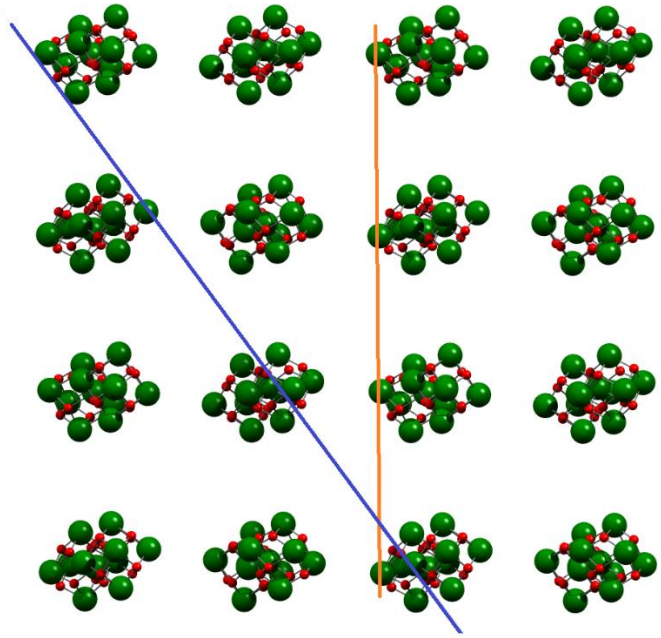


Figure 4.13 – arrangement of the Zr clusters in MFM-450 with respect to the (431) plane (blue line) and the (501) plane (orange line).

4.3.3 Gas Adsorption Studies

The N_2 isotherm of MFM-450 at 77 K is shown in Figure 4.14. From this a BET surface area of 587 m^2/g was calculated, using the built in BET calculator of the TriStar, confirming the porosity of the MOF.

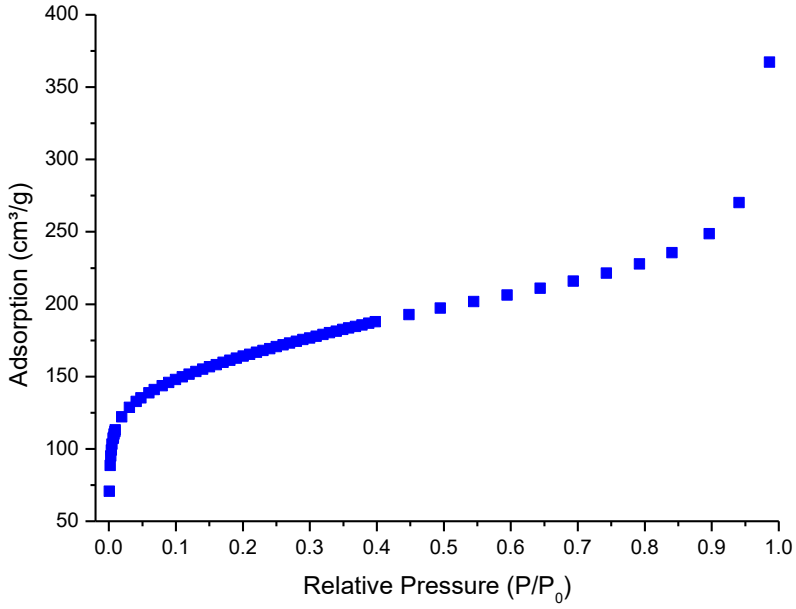


Figure 4.14 – N_2 isotherm of MFM-450 at 77 K.

In order to compare the selectivity of the framework for N_2 against CO_2, the N_2 uptake at 273, 283, and 298 K was investigated. The resulting isotherms are shown in Figure 4.15. As expected, the uptake is inversely proportional to temperature, with the isotherm at 273 K exhibiting the highest uptake of the three at 0.155 mmol/g, an uptake of 0.091 mmol/g at 283 K, and an uptake of 0.052 mmol/g at 298 K. These low values, coupled with the almost linear profile of the isotherms, suggest a low level of interaction with between N_2 and MFM-450.

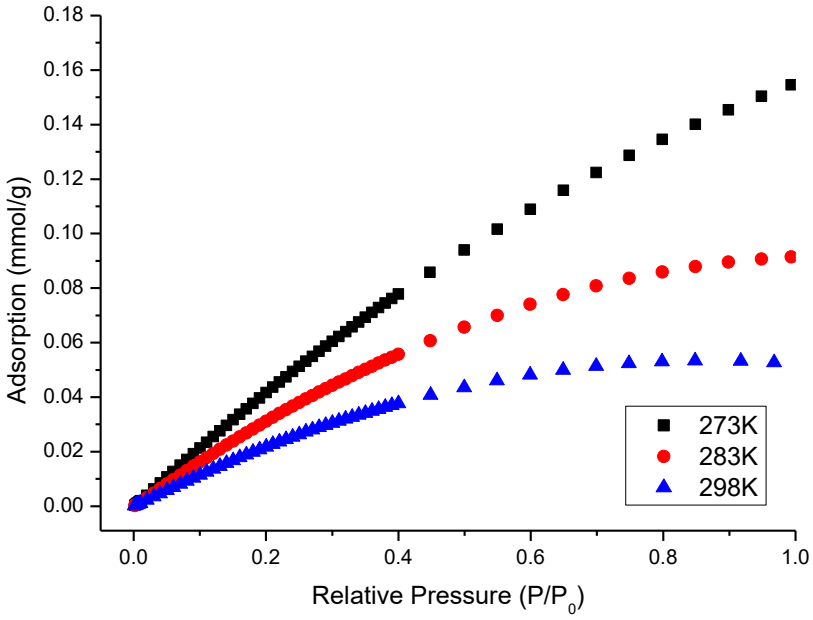


Figure 4.15 – N_2 isotherms of MFM-450 at 273 K, 283 K and 298 K.

The uptakes of CO_2 at 273, 283, and 298 K were then investigated. The resulting isotherms are shown in Figure 4.16. Again, the uptake is inversely proportional to temperature, with MFM-450 exhibiting its highest uptake, of 2.32 mmol/g, at 273 K, followed by 1.97 mmol/g, at 283 K, and 1.48 mmol/g, at 298 K. When compared to other MOFs in the literature, these values are relatively low, however, adsorption capacity is only one of the criteria to be considered for assessing the suitability of a MOF for carbon capture.

A plot of the heat of adsorption (Q_{st}) of CO_2 in MFM-450 is shown in Figure 4.17. The Q_{st} at zero coverage is 31.38 kJ/mol, confirming that the adsorption of CO_2 in this MOF is a relatively weak physisorption process.

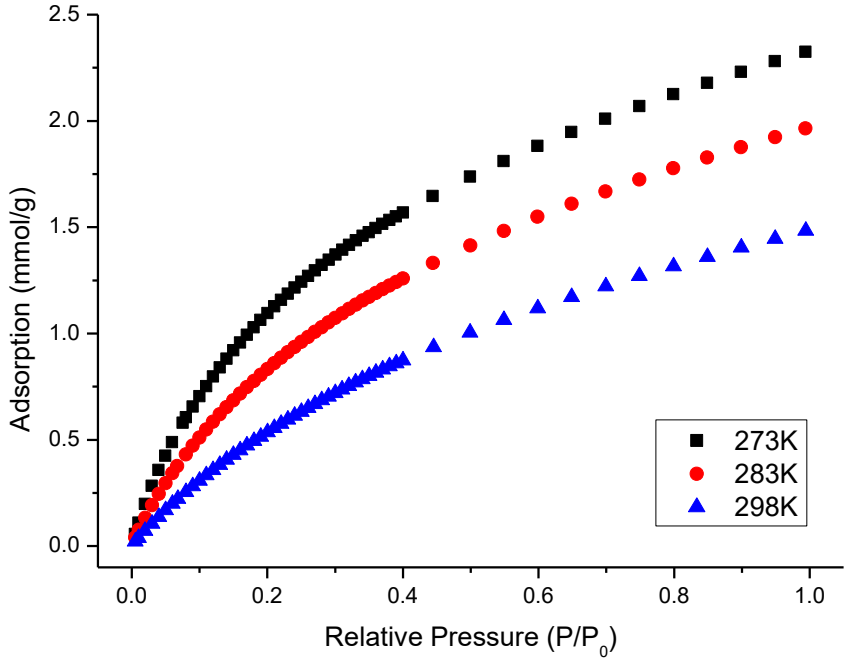


Figure 4.16 – CO_2 isotherms of MFM-450 at 273 K, 283 K and 298 K.

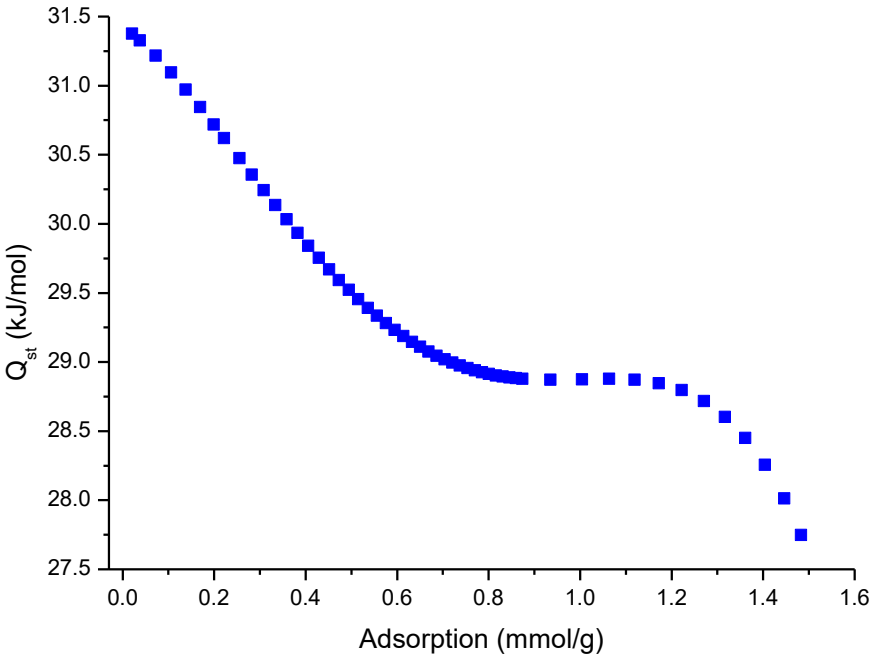


Figure 4.17 – CO_2 heat of adsorption plot for MFM-450.

4.3.4 Gas Selectivity Studies

The selective adsorption of CO_2 over N_2 is an important property to consider when assessing the suitability of a material for carbon capture. A CO_2:N_2 ratio of 15:85 is generally used with dual component selectivity calculations as this is a good estimate of the proportions of each gas in the flue gas stream. The selectivities at 273, 283 and 298 K were calculated by IAST and are shown in Figure 4.18.

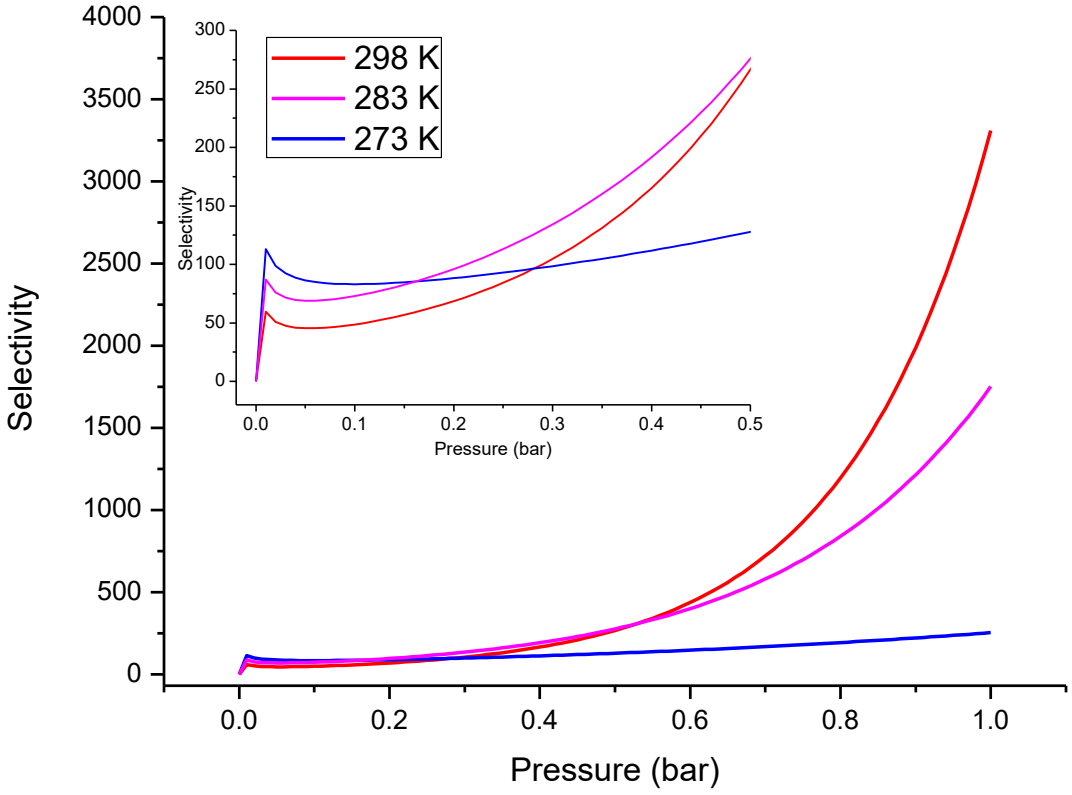


Figure 4.18 – Plots of CO_2/N_2 selectivities at 298 K, 283 K, and 273 K for MFM-450.

The selectivities follow similar shapes at each temperature. An initial decrease is observed with increasing pressure followed by a sharp increase to incredibly high

selectivities at 1 bar, of 253 at 273 K, 1750 at 283 K, and 3309 at 298 K. While these selectivities are high, they are perhaps suggestive of a problem with the IAST model in this instance, likely due to a comparatively weak interaction between the framework and N_2 and a much stronger interaction in the case of CO_2. The low pressure region shows selectivities of 113 at 273 K, 87 at 283 K, and 60 at 298 K, which seem more comparable with literature values, and also inversely correlate with temperature, which would be expected.

4.3.5 *In Situ* PXRD Studies

To probe the interaction between MFM-450 and CO_2, *in situ* high resolution PXRD was performed on the PXRD beamline I11 at DLS. The experiment was performed at 150 K to increase the amount of CO_2 in the MOF and also to reduce molecular vibration, which both increase the likelihood of accurately locating the guest molecule.

In cage A, one CO_2 site which is positionally disordered across twenty-four positions was found, each at an occupancy of 0.247. As the occupancy does not exceed 0.25, a model in which three quarters of these positions have been removed was proposed (Figure 4.19). This CO_2 molecule interacts with the phenyl ring at a distance of 3.17(8) Å from the centroid of the phenyl ring to the C atom of the CO_2. The CO_2 molecules bound to adjacent linkers are positioned in such a way to also form T-shape interaction with the other phenyl ring-bound CO_2 molecules within the cage (Figure 4.19c), at a distance of 2.8(1) Å. This creates a cyclical network within the cage, as shown in Figure 4.19b.

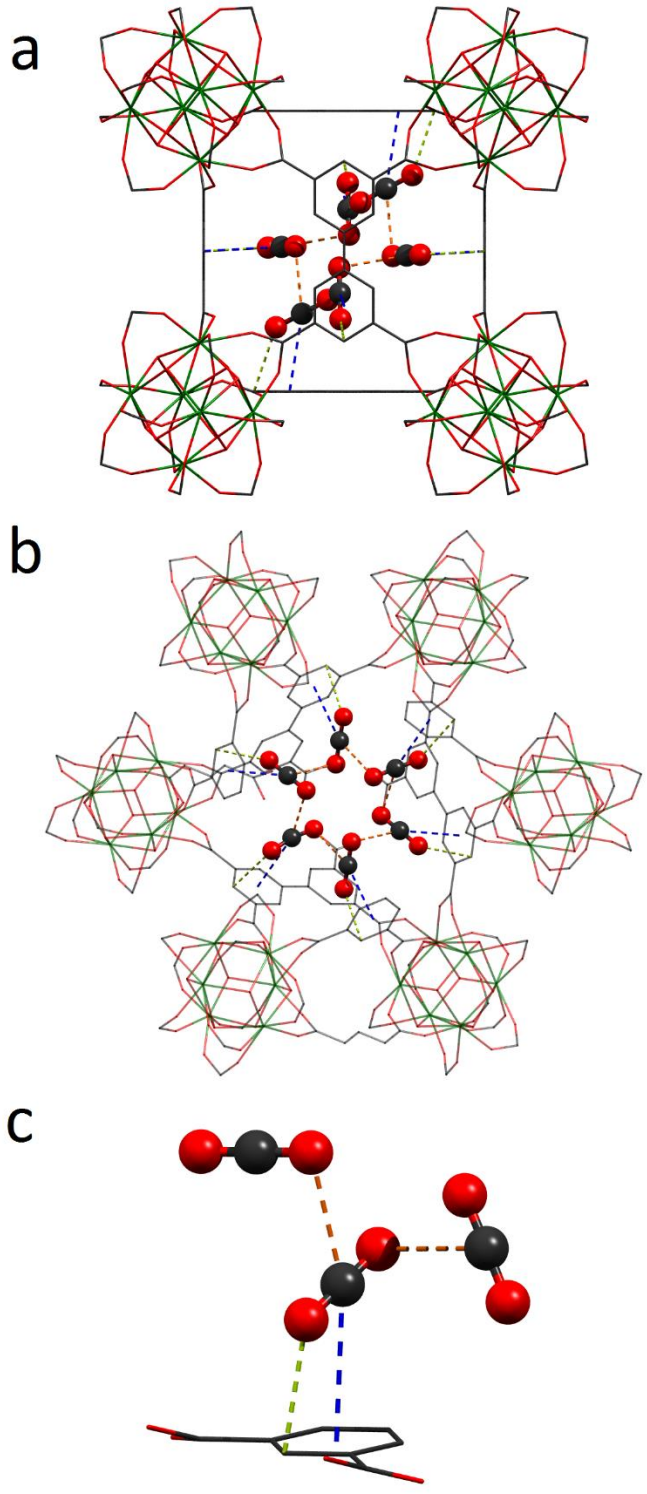


Figure 4.19 – The location of CO_2 within cage A; a) side on view of cage; b) view from a truncated corner of the cage; c) close-up view of CO_2 interaction with phenyl ring. Blue dotted line = 3.17(8) Å, orange dotted line = 2.77(13) Å.

Cage B, however, has 8 CO_2 molecules at an occupancy of 0.802, which are located in the corners of the cage (Figure 4.20). An oxygen atom of each CO_2 molecule sits pointing towards two carbons of the carboxylate functional groups of the linker at a distance of 3.57(6) Å – a type of interaction not possible in cage A, due to the alternate orientations of linkers on adjacent faces. The proximity of this CO_2 molecule to the μ_3-O atom of the framework, at a distance of 3.39(6) Å also suggests that there may be a H atom present on the μ_3-O, thus confirming the location of the μ_3-OH on the cluster.

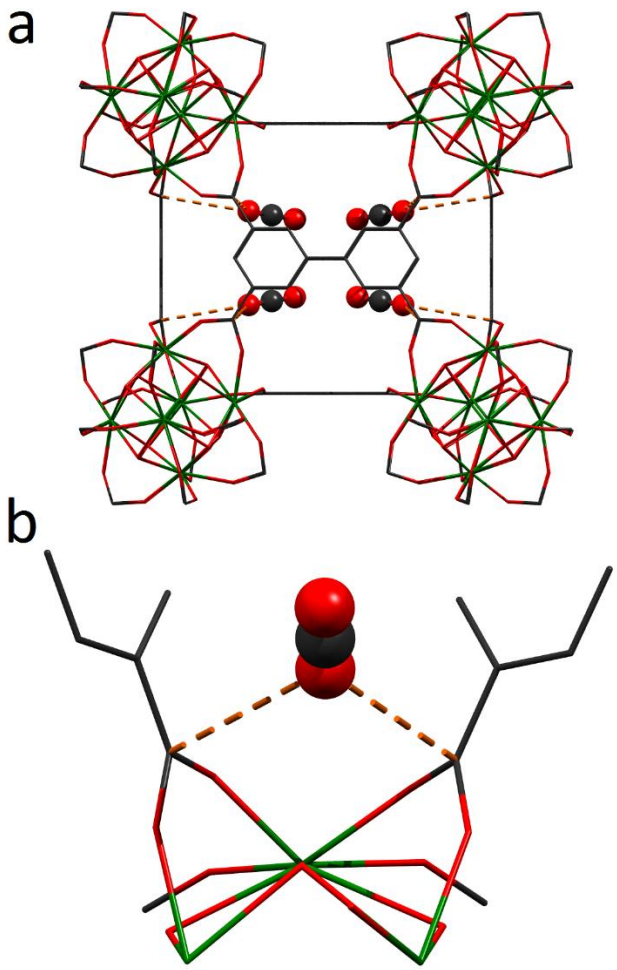


Figure 4.19 – The location of CO_2 within cage B; a) side on view of cage; b) close up of CO2 interaction with carboxylate. Orange dotted line = 3.57(6) Å

4.4 Conclusions

In summary, a Zr(IV)-BPTC MOF, MFM-450, has been synthesised and its CO_2 and N_2 uptakes measured at 273, 283, and 298 K. At each temperature, a much higher CO_2 uptake was observed over N_2, with values at 1 bar of 2.32 mmol/g CO_2 at 273 K, 1.97 mmol/g CO_2 at 283 K, and 1.48 mmol/g CO_2 at 298 K, and 0.155 mmol/g N_2 at 273 K, an uptake of 0.091 mmol/g N_2 at 283 K, and an of 0.052 mmol/g N_2 at 298 K. To probe the interaction between the framework and CO_2, an *in situ* PXRD study was conducted. Two binding sites were found in the MOF – one in cage A which interacted with the phenyl ring of the linker *via* a π-π interaction, and one in cage B which interacted with the carboxylate of the linker *via* a dipole-dipole interaction.

4.5 Experimental

All chemicals were purchased from Sigma Aldrich and were used without further purification. Elemental analysis was performed on a CE-440 elemental analyser at the University of Nottingham. TGA experiments were performed on a Pyris 1 Thermogravimetric Analyser under a flow of air. Gas isotherms were performed on a Micromeritics Tristar.

4.5.1 Synthesis of $Zr_6O_4(OH)_4(BPTC)_3$ (MFM-450)

Zirconium (IV) chloride (20 mg, 86 μmol) was combined with biphenyl-3,3',5,5'-tetracarboxylic acid (15 mg, 45 μmol) in a pressure vessel, DMF/CH_3COOH (5 ml, 1:1, v/v) added, and the suspension heated to 120°C for 48 hours. A white precipitate was then separated by centrifugation (10 min, 4000 rpm), washed with hot DMF and centrifuged (2 min, 4000 rpm) then washed with acetone and centrifuged (2 min, 4000 rpm), the acetone decanted, and the solid left to dry in air overnight. Elemental

microanalysis (%) found (calculated for $Zr_6O_{56}H_{83}C_{58}N$) C 31.12 (31.13); H 3.75 (3.74) N 0.61 (0.64).

4.5.2 High Resolution PXRD

High resolution synchrotron PXRD experiments were performed on beamline I11 at DLS (λ = 0.825690 Å). A sample of acetone-exchanged MFM-450 was loaded into a 0.7 mm borosilicate capillary which was secured into the sample cell. The cell was pressurised to 1.5 bar with N_2, the DVPC switched to 'hold' mode and the pressure monitored. The pressure remained at 2 bar indicating that the cell was sealed. The system was then evacuated of N_2 and dosed with CO_2 to 2 bar.

The sample was then activated at 403 K under vacuum (1 x 10^{-6} bar) for 1 hour, cooled to 150 K and data was collected for 40 minutes with beamline I11's high resolution MAC detectors. The sample was then dosed with 1 bar of CO_2 at 150 K, and after 30 minutes of equilibration, data collected for 40 minutes using MAC detectors.

4.5.3 Structural Refinement Details

The activated structure and 1 bar CO_2 loaded structure were refined with the Rietveld method using TOPAS Academic 5, with input files created in jEdit. The backgrounds of the profiles were fit using a Chebyshev polynomial with 12 coefficients. A *hkl* dependent peak function was used to account for the broadening of peaks with odd values of *h*, *k* or *l*. CO_2 molecules were modelled as rigid bodies and their positions and orientations found initially via simulated annealing, followed by refinement. The framework was soft-restrained, and refined after CO_2 refinement, resulting in excellent fits.

4.6 References

1. T. Loiseau, C. Serre, C. Huguenard, G. Fink, F. Taulelle, M. Henry, T. Bataille and G. Ferey, *Chemistry*, 2004, **10**, 1373-1382.

2. J. H. Cavka, S. Jakobsen, U. Olsbye, N. Guillou, C. Lamberti, S. Bordiga and K. P. Lillerud, *J. Am. Chem. Soc*., 2008, **130**, 13850-13851.

3. G. E. Cmarik, M. Kim, S. M. Cohen and K. S. Walton, *Langmuir*, 2012, 28, 15606-15613.

4. Q. Yang, A. D. Wiersum, P. L. Llewellyn, V. Guillerm, C. Serre and G. Maurin, *Chem. Commun.*, 2011, **47**, 9603-9605.

5. P. Roy, A. Schaate, P. Behrens and A. Godt, *Chemistry*, 2012, **18**, 6979-6985.

6. H. Furukawa, F. Gándara, Y-B. Zhang, J. Jiang, W. L. Queen, M. R. Hudson, and O. M. Yaghi, *J. Am. Chem. Soc.*, 2014, **136**, 4369–4381.

7. A. Schaate, P. Roy, A. Godt, J. Lippke, F. Waltz, M. Wiebcke and P. Behrens, *Chemistry*, 2011, **17**, 6643-6651.

8. V. Bon, I. Senkovska, I. A. Baburin and S. Kaskel, *Cryst. Growth Des.*, 2013, **13**, 1231-1237.

9. V. Guillerm, F. Ragon, M. Dan-Hardi, T. Devic, M. Vishnuvarthan, B. Campo, A. Vimont, G. Clet, Q. Yang, G. Maurin, G. Ferey, A. Vittadini, S. Gross and C. Serre, *Angew. Chem. Int. Ed. Engl.*, 2012, **51**, 9267-9271.

Conclusions

The work in this thesis has successfully achieved the goal of gaining an understanding of guest-MOF interactions via PXRD.

In Chapter 2, a new remote control gas dosing system for use on powder diffraction beamline I11 at DLS was presented. This system offers much greater precision and control over the previous manual system. Using this system, the response of MFM-300(V) to both pure CO_2 and an equimolar mixture of CO_2 and N_2 was investigated. Two CO_2 sites were found in all cases, with CO_2-A forming a dipole-dipole interaction with the framework's hydroxyl group, and CO_2-B interacting with CO_2-A *via* further dipole-dipole interaction. The presence of N_2 in the mixture was found to affect the position of the CO2 molecules, particularly at low loadings. Further to this, for the first time, the long term SO_2 adsorption stability of a MOF, MFM-300(Al), was studied by powder diffraction. The SO_2-loaded MOF was found to remain stable over a period of 37 weeks.

In Chapter 3, the successful separation of *m*-xylene from ethylbenzene and *o*-, and *p*-xylene using MFM-300(In) was demonstrated. Contrary to promising results from vapour adsorption experiments, MFM-300(Al) showed no significant separation of the 4 compounds in the liquid phase. MFM-300(V), however was slightly more promising, and shows the best separation of ethylbenzene and *o*-xylene out of all 3 MOFs, however suffers from very broad peaks which lower the resolution of the chromatogram. PXRD studies of C_8 hydrocarbon-loaded MFM-300(M) revealed π-π stacking interactions between the C_8 hydrocarbons and the phenyl ring of the framework, and in the case of MFM-300(In)(*p*-xylene), tetragonal $I4_122 \rightarrow$ orthorhombic $I2_12_12_1$ phase change was observed. High pressure PXRD results confirm that this phase change can also be induced by pressure of 0.584 GPa.

In Chapter 4, a new Zr(IV)-BPTC MOF, MFM-450, was synthesised and its CO2 and N2 adsorption properties investigated. As it showed some promise for CO_2/N_2 selectivity, an *in situ* PXRD experiment was performed. The results confirmed a π-π stacking interaction between CO_2 and the phenyl ring in cage A of the MOF, whereas in cage B, the orientation of the linkers allowed for a dipole-dipole interaction with the carboxylate moiety of the linker.

Appendices

Appendix 1.1 - Fits of Rietveld refinements from single component CO_2 adsorption experiment with MFM-300(V)

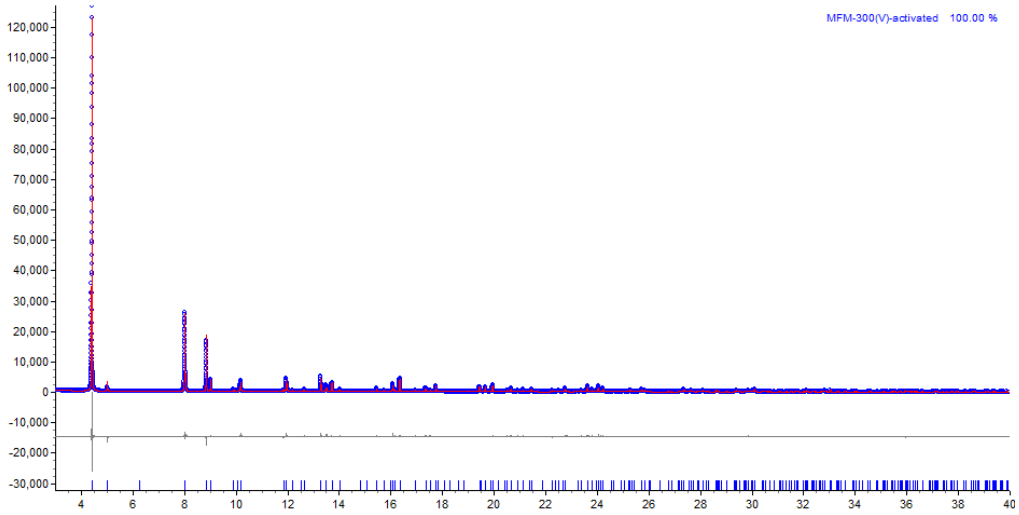


Figure A1 – Rietveld refinement plot of MFM-300(V^{III}). Blue open circle = observed; red line = calculated; grey line = difference.

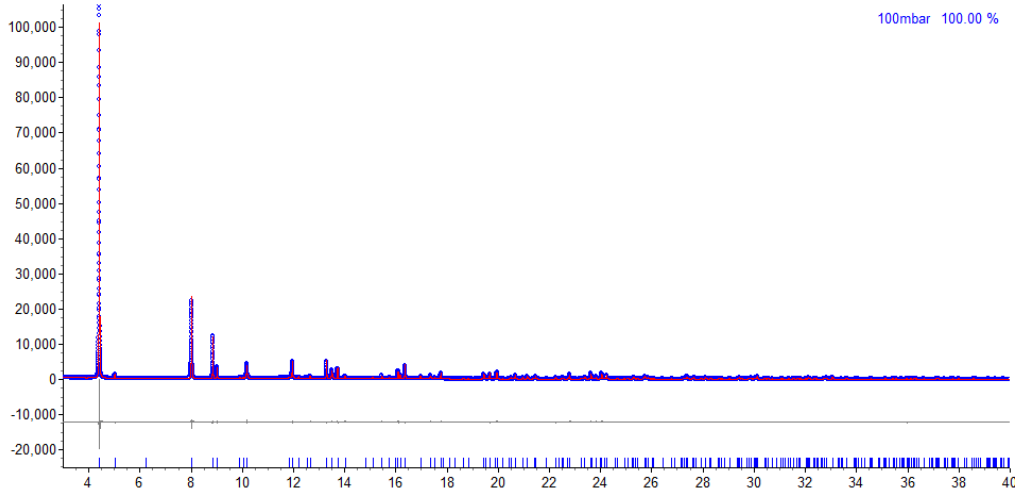


Figure A2 – Rietveld refinement plot of MFM-300(V^{III})-I. Blue open circle = observed; red line = calculated; grey line = difference.

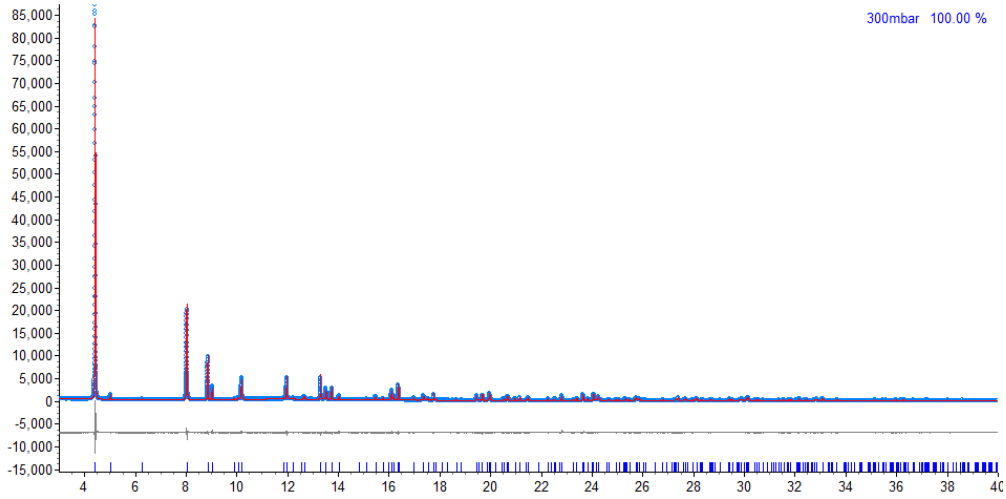


Figure A3 – Rietveld refinement plot of MFM-300(V^{III})-II. Blue open circle = observed; red line = calculated; grey line = difference.

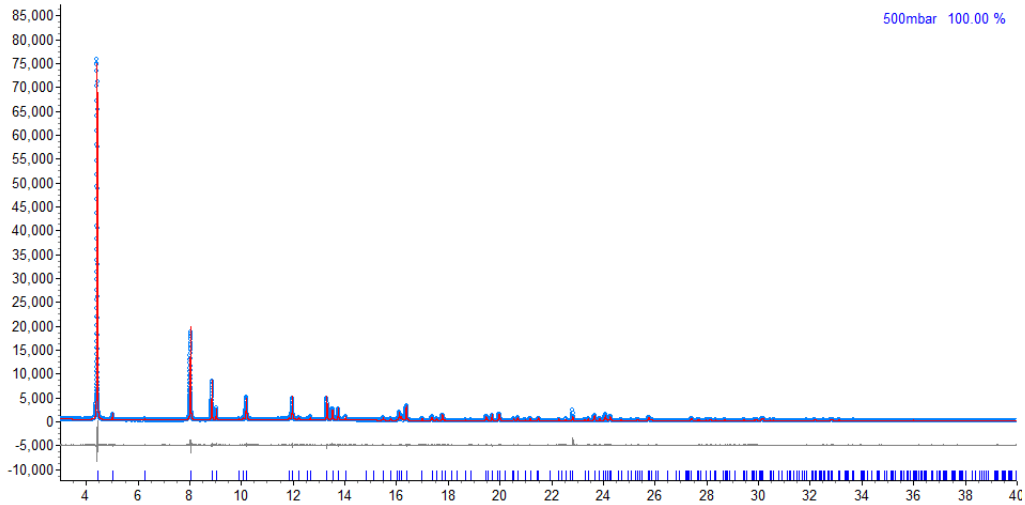


Figure A4 – Rietveld refinement plot of MFM-300(V^{III})-III. Blue open circle = observed; red line = calculated; grey line = difference.

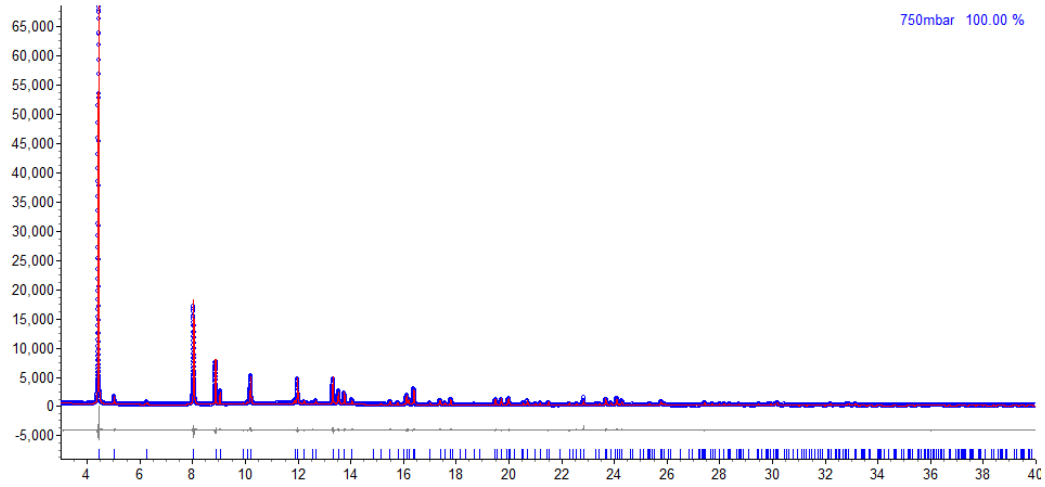


Figure A5 – Rietveld refinement plot of MFM-300(V^{III})-IV. Blue open circle = observed; red line = calculated; grey line = difference.

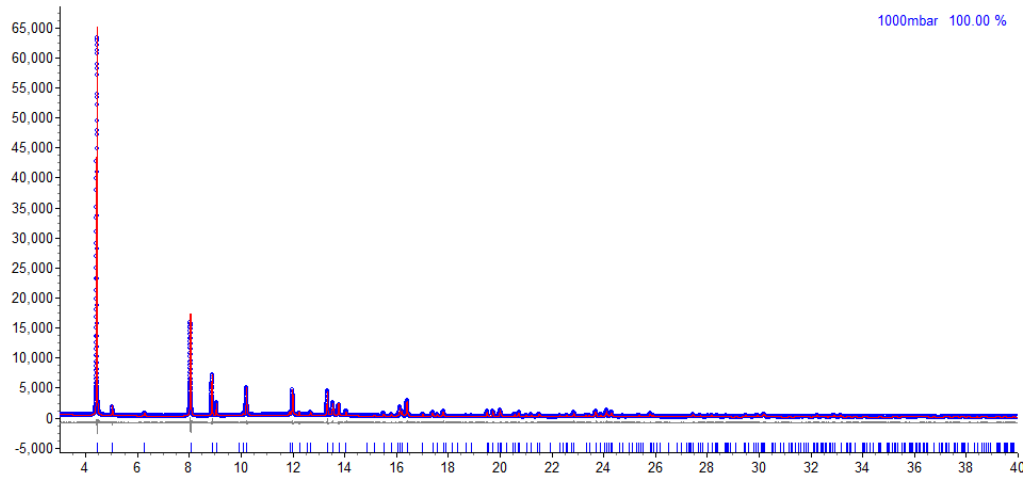


Figure A6 – Rietveld refinement plot of MFM-300(V^{III})-V. Blue open circle = observed; red line = calculated; grey line = difference.

Appendix 1.2 – Fits of Rietveld refinements from dual component N_2/CO_2 adsorption experiment

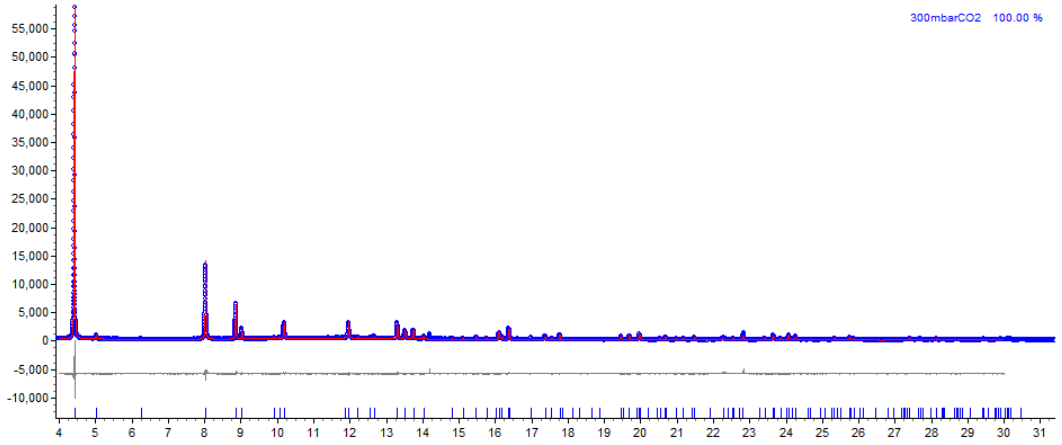


Figure A7 – Rietveld refinement plot of MFM-300(V^{III})-VI. Blue open circle = observed; red line = calculated; grey line = difference.

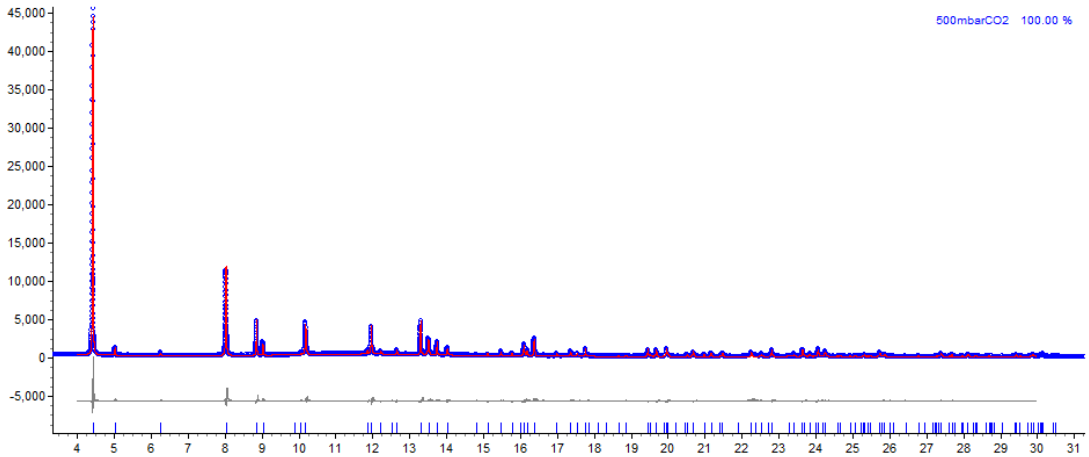


Figure A8– Rietveld refinement plot of MFM-300(V^{III})-VII. Blue open circle = observed; red line = calculated; grey line = difference.

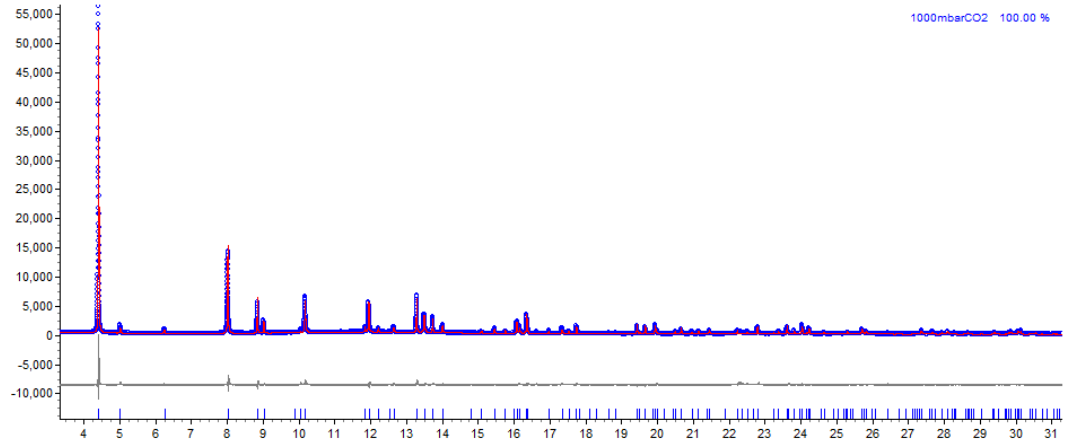


Figure A9 – Rietveld refinement plot of MFM-300(V^{III})-VII. Blue open circle = observed; red line = calculated; grey line = difference.

Appendix 1.3 – Fit of SO_2 LDE PXRD

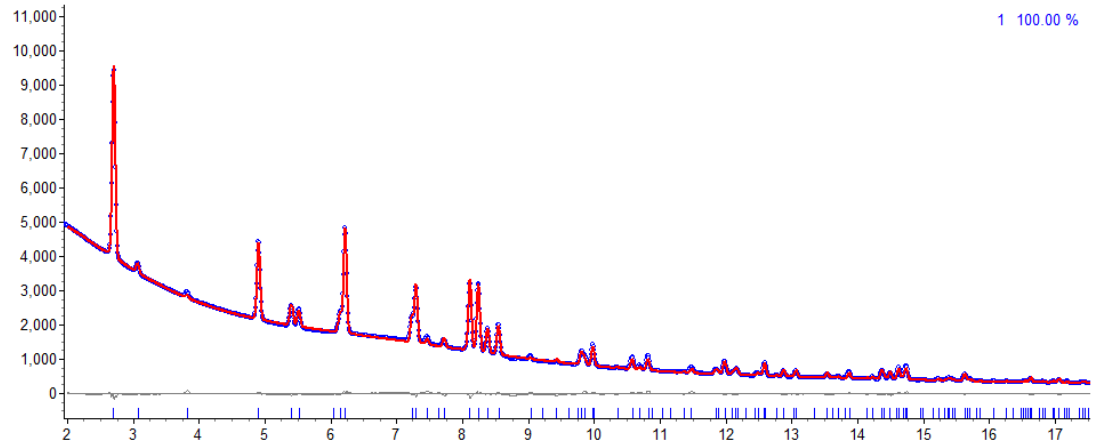


Figure A10 – Rietveld refinement plot of MFM-300(Al)•4SO_2 from LDE experiment. Blue open circle = observed; red line = calculated; grey line = difference.

Appendix 1.4 – C_8 Hydrocarbon loaded MFM-300(M) PXRD

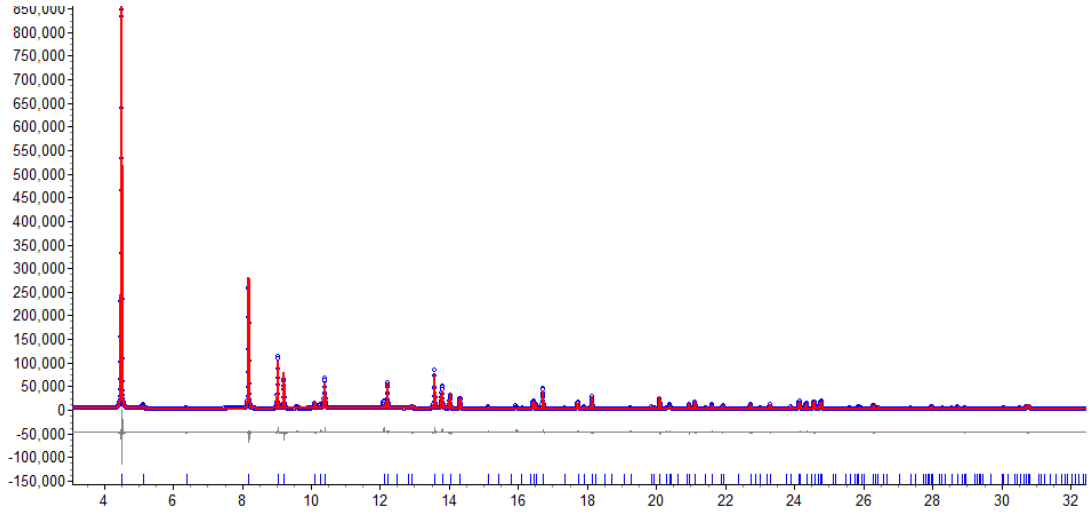


Figure A11 – Rietveld refinement plot of o-xylene loaded MFM-300(Al). Blue open circle = observed; red line = calculated; grey line = difference.

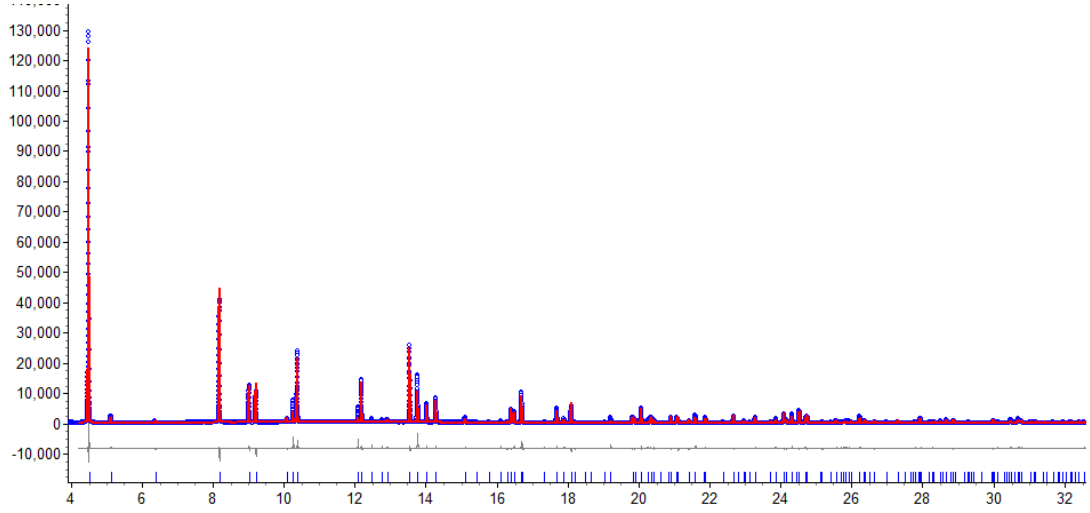


Figure A12 – Rietveld refinement plot of ethylbenzene loaded MFM-300(Al). Blue open circle = observed; red line = calculated; grey line = difference.

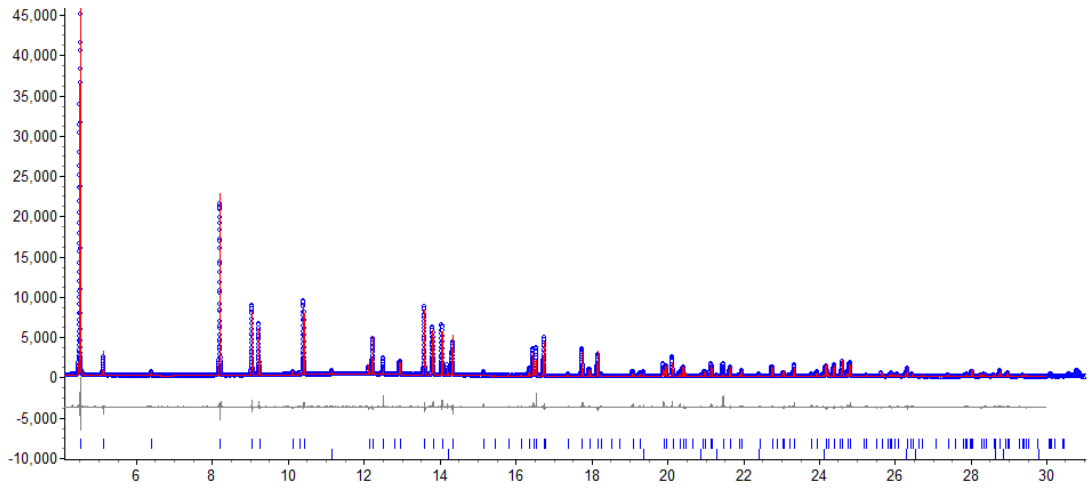


Figure A13 – Rietveld refinement plot of m-xylene loaded MFM-300(Al). Blue open circle = observed; red line = calculated; grey line = difference.

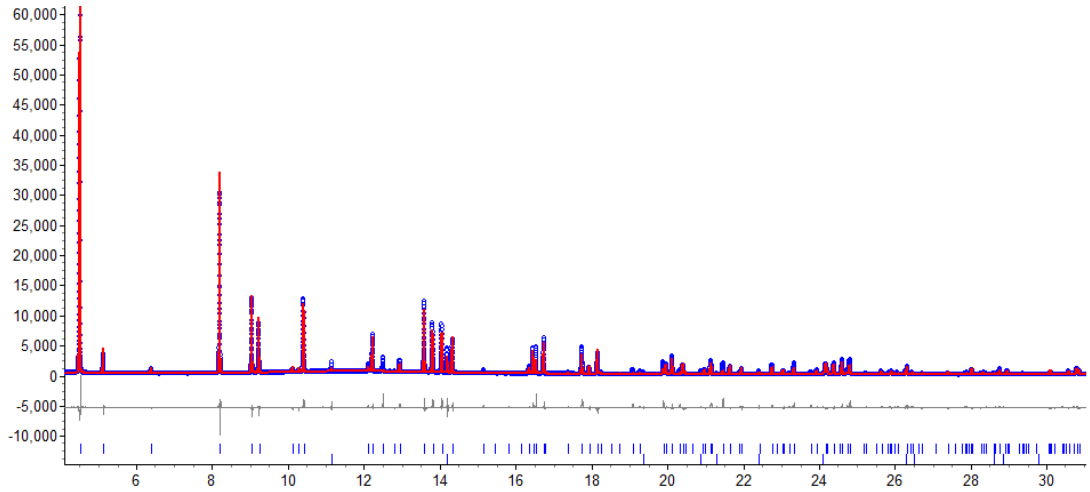


Figure A14 – Rietveld refinement plot of p-xylene loaded MFM-300(Al). Blue open circle = observed; red line = calculated; grey line = difference.

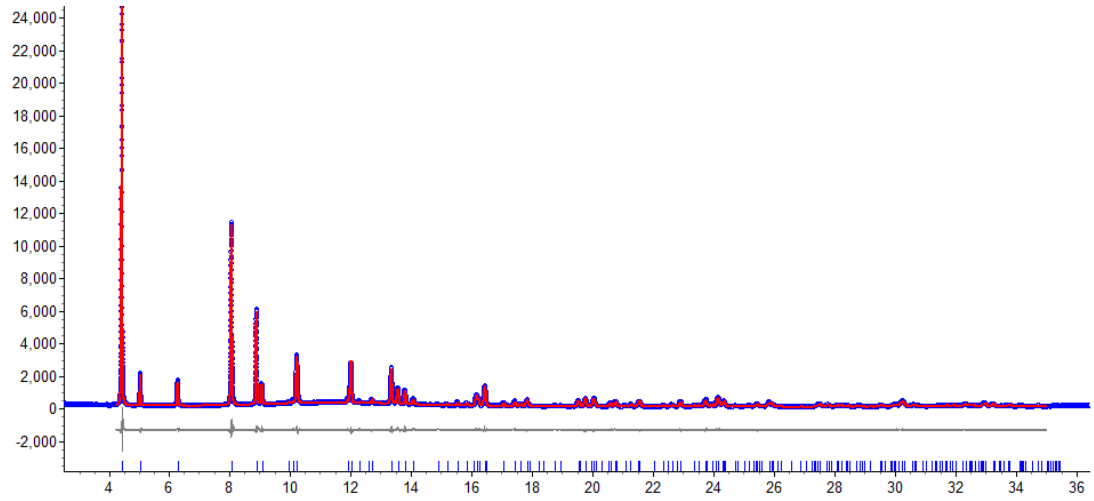


Figure A15 – Rietveld refinement plot of ethylbenzene loaded MFM-300(V). Blue open circle = observed; red line = calculated; grey line = difference.

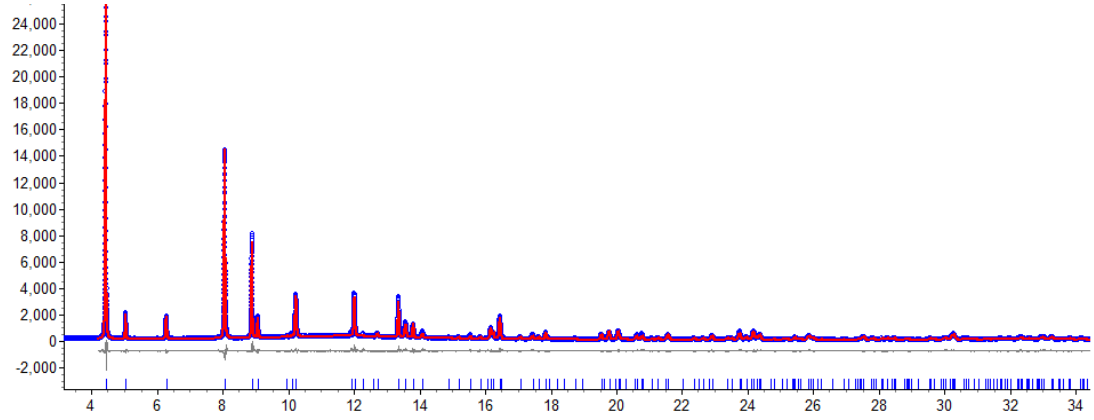


Figure A16 – Rietveld refinement plot of m-xylene loaded MFM-300(V). Blue open circle = observed; red line = calculated; grey line = difference.

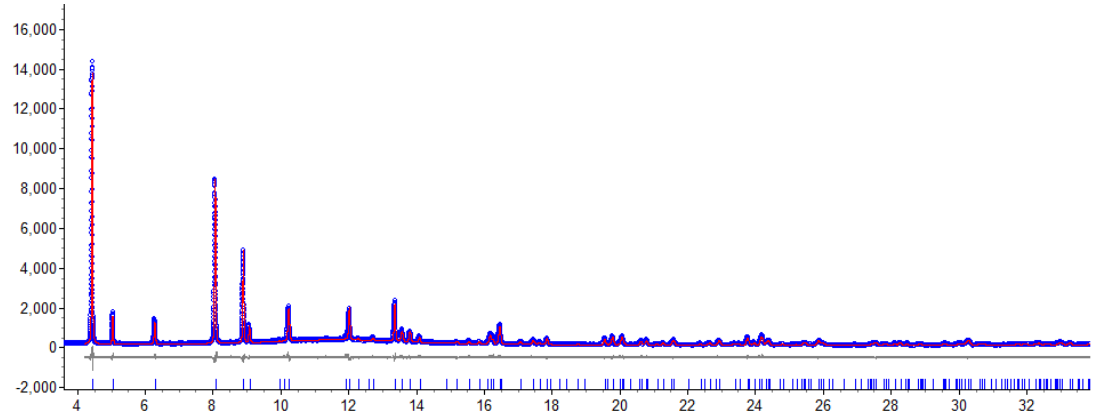


Figure A17 – Rietveld refinement plot of o-xylene loaded MFM-300(V). Blue open circle = observed; red line = calculated; grey line = difference.

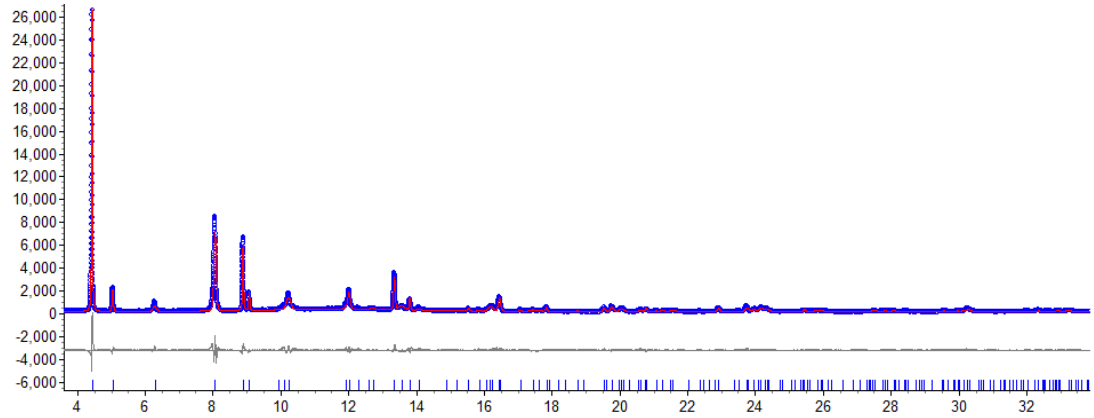


Figure A18 – Rietveld refinement plot of p-xylene loaded MFM-300(V). Blue open circle = observed; red line = calculated; grey line = difference.

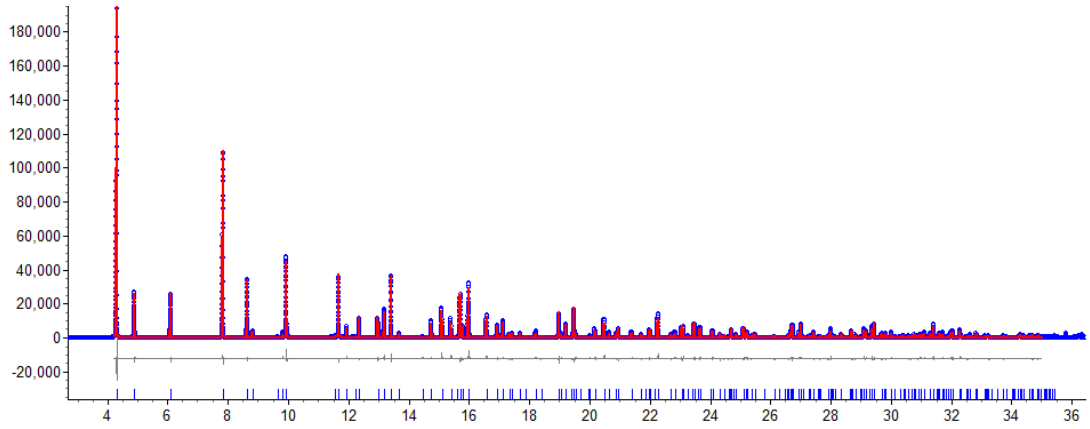


Figure A19 – Rietveld refinement plot of ethylbenzene loaded MFM-300(In). Blue open circle = observed; red line = calculated; grey line = difference.

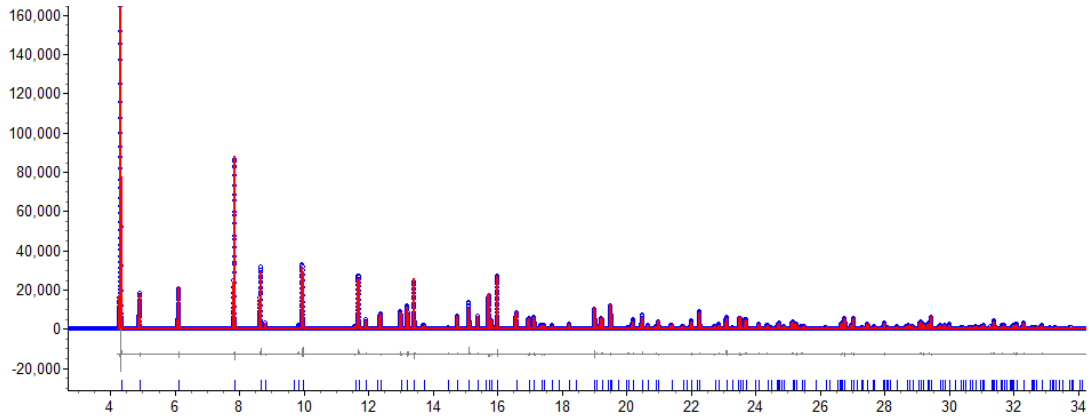


Figure A20 – Rietveld refinement plot of ethylbenzene loaded MFM-300(In). Blue open circle = observed; red line = calculated; grey line = difference.

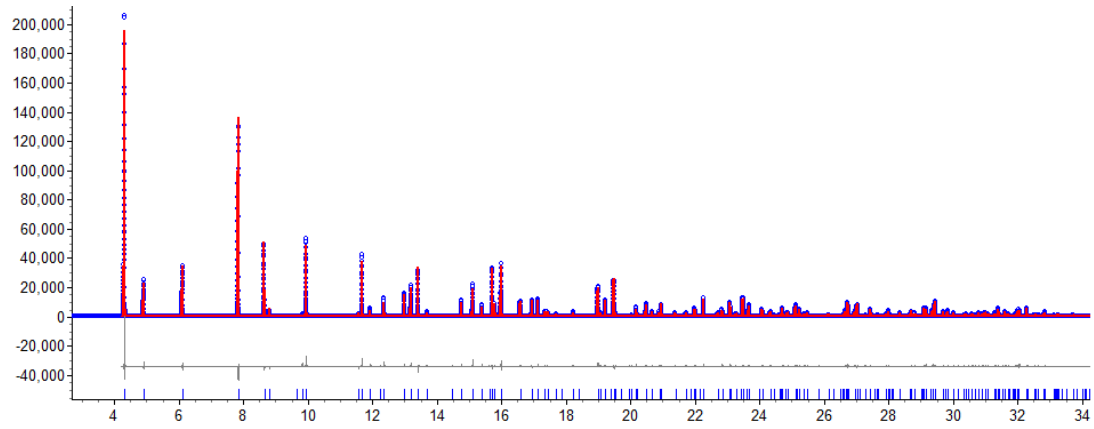


Figure A21 – Rietveld refinement plot of o-xylene loaded MFM-300(In). Blue open circle = observed; red line = calculated; grey line = difference.

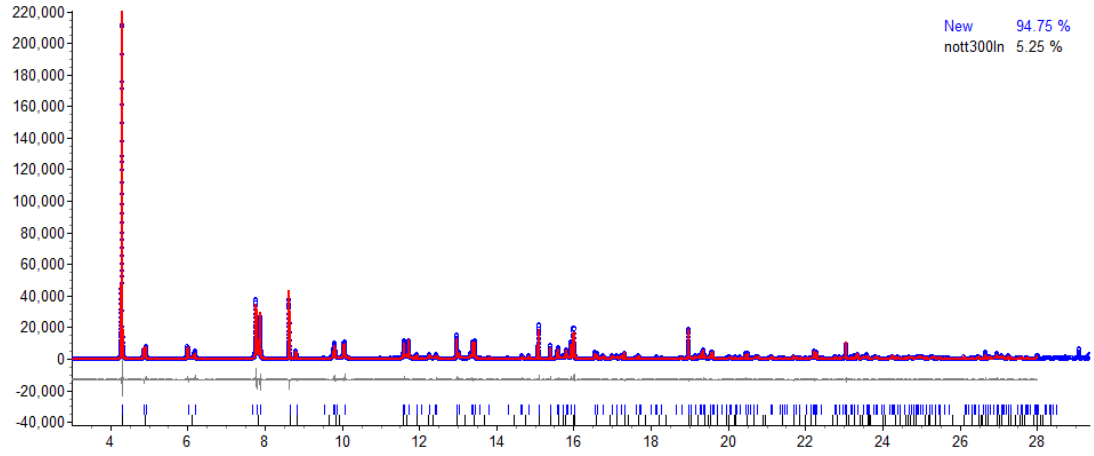


Figure A22 – Rietveld refinement plot of p-xylene loaded MFM-300(In). Blue open circle = observed; red line = calculated; grey line = difference.

Appendix 1.5 – MFM-450 PXRD

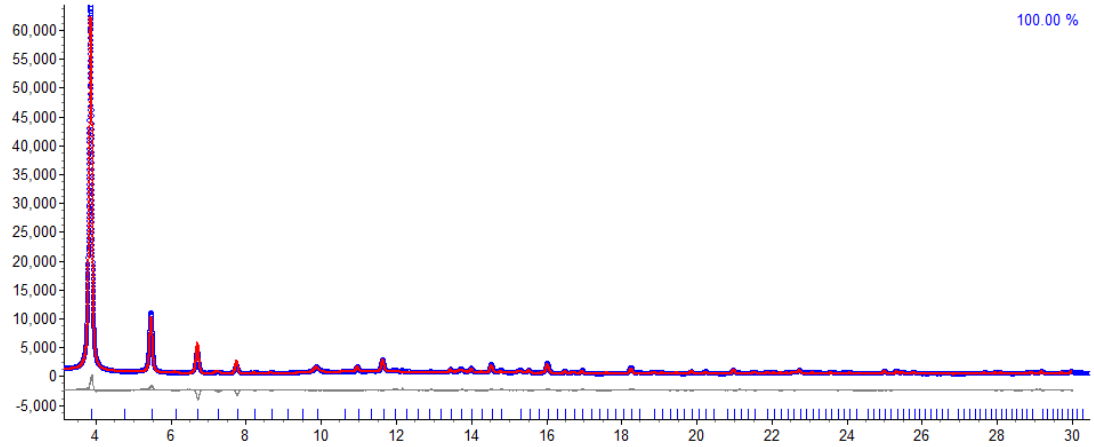


Figure A23 – Rietveld refinement plot of activated MFM-450. Blue open circle = observed; red line = calculated; grey line = difference.

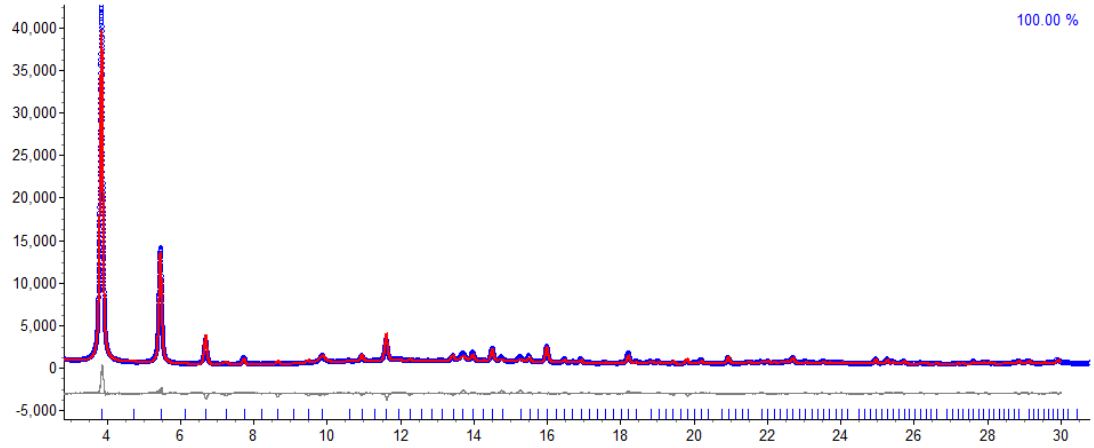


Figure A24 – Rietveld refinement plot of 1 bar CO_2-loaded MFM-450. Blue open circle = observed; red line = calculated; grey line = difference.